

ANISOTROPY OF MAGNETIC SUSCEPTIBILITY  
OF PHREATOMAGMATIC SURGE DEPOSITS,  
HOPI BUTTES, NAVAJO NATION, ARIZONA, USA

By Trenton T. Newkirk

A Thesis  
Submitted in Partial Fulfillment  
of the Requirements for the Degree of  
Master of Science  
in Geology

Northern Arizona University  
May 2009

Approved:

---

Michael H. Ort, Ph.D., Chair

---

Nancy R. Riggs, Ph.D.

---

Wendell A. Duffield, Ph.D.

## **ABSTRACT**

### **ANISOTROPY OF MAGNETIC SUSCEPTIBILITY OF PHREATOMAGMATIC SURGE DEPOSITS, HOPI BUTTES, NAVAJO NATION, ARIZONA, USA**

**TRENTON T. NEWKIRK**

The Mio-Pliocene Hopi Buttes volcanic field records phreatomagmatic eruptions as a result of alkaline mafic magma through water-saturated sediments in a playa-type setting. The resulting phreatomagmatic features include maar volcanoes and their associated outflow and surge deposits. Phreatomagmatic surge deposits are formed during single depositional episodes. These deposits can be traced laterally in cliff exposures up to 1400 meters from the eruptive vent. Anisotropy of magnetic susceptibility (AMS) was applied to rocks on these deposits to offer insight into the emplacement processes of phreatomagmatic surges.

In each of the main study areas, the general AMS results show a characteristic proximal, medial, and distal signature. AMS trends exhibit an increasing organization with respect to magnetic axes with lateral distance from the eruptive vent through the medial sections of the dataset; this trend generally becomes less lineated, but still well foliated in the distal reaches.

The AMS results from this study can be categorized into three distinct AMS signatures that correlate with spatial trends in deposit characteristics in the field. These physical regions are defined by the lateral facies changes observed within the individual flow units. These distinct AMS categories – essentially AMS ‘fabrics’ – can be discussed within the spatial context of 1) disorganized facies (proximal), 2) lineated facies (medial), and 3) girdled facies (distal). The results from AMS analyses at Triplets maar, Haskie maar and Deshgish butte exhibit a general pattern towards increasing organization from proximal to medial locations with respect to distance from eruptive source, finally transitioning to an AMS signature that is well foliated, but less lineated at distal depositional reaches.

## ACKNOWLEDGEMENTS

I would like to thank my advisor, Dr. Michael Ort for his tenacity over the years, and my committee, Drs. Nancy Riggs, and Wendell Duffield, for their support throughout the final process. I would also like to acknowledge my lone funding source USGS-DOI EDMAP grant. Many thanks to UNMPL (University of New Mexico Paleomagnetic Lab) and NAUPL (Northern Arizona Paleomagnetic Lab) for granting me the opportunity to run my AMS and ChRM samples, and to the individuals who granted me permission and provided the necessary training: Dr. Mike Petronis, and Dr. John Geismann. For technical support and sample processing, I'd like to thank Ben Peterson, and James Wallace for the aerial imagery. I thank the families around the field area for their hospitality and friendliness, especially the Bichitty's and Haskie's. The Navajo Nation Minerals Department was kind enough to allow me to conduct research on Tsézhin bií. Any person wishing to conduct geologic investigation on the Navajo Nation must first apply for and receive a permit from the Navajo Nation Minerals Department, PO Box 9000, Window Rock, AZ 86515.

Finally, I'd like to thank Erin Young, and Karen Vanaman for their support and letting me crash at their homes for sometimes weeks-on-end. I am forever indebted to my parents for giving me, through their own example, the belief that hard work and perseverance achieves all goals. Lastly and most importantly the conclusion of this whole endeavor would never have come to fruition without the love and support of my wife and best friend, Sara Jenkins.

## TABLE OF CONTENTS

---

<b>ABSTRACT .....</b>	<b>II</b>
<b>ACKNOWLEDGEMENTS .....</b>	<b>III</b>
<b>TABLE OF CONTENTS.....</b>	<b>IV</b>
<b>LIST OF TABLES .....</b>	<b>VII</b>
<b>LIST OF FIGURES .....</b>	<b>VIII</b>
<b>LIST OF PLATES .....</b>	<b>VIII</b>
<b>CHAPTER 1: INTRODUCTION AND BACKGROUND.....</b>	<b>1</b>
INTRODUCTION .....	1
TEXTURAL SIGNIFICANCE OF AMS .....	1
REGIONAL GEOLOGY (COLORADO PLATEAU).....	2
PHREATOMAGMATISM .....	8
SURGE EMPLACEMENT MODELS.....	9
SURGE EMPLACEMENT PROCESSES.....	10
DEPOSITIONAL PROCESSES AND FACIES .....	15
PROJECT SIGNIFICANCE.....	16
<b>CHAPTER 2: PROJECT METHODS .....</b>	<b>18</b>
FIELD METHODS .....	18
MAGNETIC METHODS.....	18
Magnetic Remanence .....	18
Anisotropy of Magnetic Susceptibility (AMS).....	19
ANALYTICAL METHODS .....	21
<b>CHAPTER 3: VOLCANIC FACIES, VOLCANO DESCRIPTIONS AND FIELD INTERPRETATIONS .....</b>	<b>24</b>
STANDARD FACIES FOR VOLCANIC SEQUENCES.....	24
Facies LT1: Disorganized and Poorly Stratified Lapilli-Tuff.....	24
Facies LT2: Moderately stratified lapilli-tuff .....	26
Facies LT3: Stratified undulatory lapilli-tuff.....	26
Facies T4: Moderately stratified tuffs .....	28
Facies LT5: Stratified undulatory tuff .....	28
Facies T6: Stratified undulatory juvenile-rich tuff.....	29
Facies T7: Erosional Sandwave-Bedded Tuff .....	29

Facies T8: Sandwave-bedded ash tuff .....	31
Facies T9: Planar-stratified tuff .....	31
Facies T10: Planar-laminated tuff .....	32
<b>VOLCANO DESCRIPTIONS .....</b>	<b>32</b>
Triplets Maar .....	32
Haskie Maar .....	35
Deshgish Butte .....	37
<b>CHAPTER 4: RESULTS OF MAGNATIC REMANENCE ANALYSES.....</b>	<b>40</b>
<b>CHRM RESULTS.....</b>	<b>40</b>
Triplets ChRM Results .....	40
Haskie Maar ChRM Results .....	42
<b>AMS RESULTS .....</b>	<b>42</b>
Triplets AMS Results .....	42
Haskie AMS Results .....	50
Deshgish AMS Results .....	54
<b>CHAPTER 5: AMS FABRIC INTERPRETATION .....</b>	<b>57</b>
<b>PROCESSES (AMS).....</b>	<b>57</b>
Disorganized AMS Facies Deposits.....	57
Lineated AMS Facies Deposits.....	59
Girdled AMS Facies Deposits .....	60
<b>CHAPTER 6: CONCLUSIONS .....</b>	<b>62</b>
<b>REFERENCES CITED .....</b>	<b>64</b>
<b>APPENDICES.....</b>	<b>75</b>
APPENDIX 1: ChRM Data for Study Sites.....	75
APPENDIX 2: AMS Data for Study Sites.....	82

## LIST OF TABLES

---

<b>Table 1:</b> Anisotropy of Magnetic Susceptibility (AMS) Data from Hopi Buttes Phreatomagmatic Deposits.....	45
<b>Table 2:</b> Triplets Maar AMS Textural Discrimination Table.....	46
<b>Table 3:</b> Haskie Maar AMS Textural Discrimination Table.....	52
<b>Table 4:</b> Deshghish AMS Textural Discrimination Table.....	56

## LIST OF FIGURES

---

<b>Figure 1:</b> Distribution of Middle to Late Cenozoic Volcanic Centers in the Southwestern United States.....	3
<b>Figure 2:</b> Map of the Hopi Buttes Volcanic Field.....	7
<b>Figure 3:</b> Stages of Surge Development.....	12
<b>Figure 4:</b> Facies photos of LT1 and LT2.....	25
<b>Figure 5:</b> Facies photos of LT3 and LT5.....	27
<b>Figure 6:</b> Facies photos of LT5 and T6.....	30
<b>Figure 7:</b> Stratigraphic Section of Triplets Maar Phreatomagmatic Deposits.....	34
<b>Figure 8:</b> Stratigraphic Section of Haskie Maar Phreatomagmatic Deposits.....	36
<b>Figure 9:</b> Stratigraphic Section of Desgish Butte Phreatomagmatic Deposits.....	38
<b>Figure 10:</b> Triplets Maar and Associated Volcanic Deposits, with ChRM Results.....	41
<b>Figure 11:</b> Haskie Maar and Associated Volcanic Deposits, with ChRM Results.....	41
<b>Figure 12:</b> Triplets Maar, Associated Volcanic Deposits and AMS Results.....	44
<b>Figure 13:</b> Ratio of $\alpha_{95}$ error of declination/ $\alpha_{95}$ error.....	48
<b>Figure 14:</b> Haskie Maar, Associated Volcanic Deposits and AMS Results.....	50
<b>Figure 15:</b> Deshgish Butte, Associated Volcanic Deposits and AMS Results.....	55
<b>Figure 16:</b> Stages of Surge Development with Associated AMS Signatures.....	58

## LIST OF PLATES

---

**Plate 1:** Geologic Map of Deshgish Butte and Vicinity, Indian Wells and White Cone 7.5' Quadrangles, Hopi Buttes, Navajo Nation, (Tsézhin bií), Arizona, USA (back cover pocket).



## **CHAPTER 1: INTRODUCTION AND BACKGROUND**

---

### ***INTRODUCTION***

The Hopi Buttes volcanic field is a unique location for the study of phreatomagmatic volcanism in that it affords the opportunity to view a spectrum of volcanic processes, from the subvolcanic magma-water interaction zones to soft-sediment deformation of lacustrine units. One of the characteristics of the Hopi Buttes volcanic field is that, in many cases, individual emplacement (rock) units have a continuous exposure that can be traced back to their eruptive vent. This characteristic allows us to make observations on the deposits at variable distances from a vent, producing snapshots of a single moment in transport processes during which material was deposited.

Phreatomagmatic depositional processes have long been studied in detail, but the modern analytical techniques employed during analysis of magnetic data have evolved within the past twenty years. The use of paleomagnetic techniques, such as anisotropy of magnetic susceptibility (AMS), offers a researcher the ability to observe a change in microscopic textures in any spatial or temporal relation. The current research at the Hopi Buttes volcanic field aims to further enhance understanding of the rapid and dynamic processes involved in phreatomagmatic eruptions through analysis of magnetic fabric properties along the length of the depositional flow path. The project seeks a robust correlation between unique AMS signatures, microscopic transport processes, and distance from eruptive vent as flow processes change with decreasing lateral momentum.

### ***TEXTURAL SIGNIFICANCE OF AMS***

Magnetic textural analysis (i.e. AMS) and granulometric studies (i.e. grain size and clast morphology analysis) have been used with great success to aid in the interpretation of transport processes of density currents. AMS analysis offers a non-destructive method of observing microscopic textures, and gives insight into the rock's microscopic magnetic fabric, which in turn yields quantitative particle directional data.

Granulometric studies have afforded scientists the ability to statistically observe clast size and particle morphology evolution, which can then be spatially referenced. These studies offer us a better understanding of depositional properties in recent eruptive

events and modern systems, which we then can use to interpret ancient deposits. However, these studies destroy the orientations of emplacement and do not give insight into the detailed depositional fabrics preserved within the matrix and orientation of the particles and clasts. Clast counts and sieving offer information on component analysis, but do not provide objective directional measurements. AMS and granulometric analysis both offer valuable insights into emplacement processes. It is unfortunate that, if the deposit can be drilled for AMS analysis, it is likely too indurated to be sieved for granulometric analyses, so the two types of analyses can rarely be made on the same deposits.

AMS has been used to evaluate flow directions in pyroclastic flow deposits, to determine vent location (Ellwood, 1982; Incoronato et al., 1983; Knight et al., 1986, Wolff et al., 1989; MacDonald and Palmer, 1990; Hillhouse and Wells, 1991; Palmer et al., 1991; Seaman et al., 1991; Ort, 1993; Cagnoli and Tarling, 1997; MacDonald et al., 1998; Ort et al., 1999) or to provide information about depositional processes of ignimbrites (Fisher et al., 1993; Baer et al., 1997; Le Pennec et al., 1998; Palmer and MacDonald, 1999; Burgisser and Bergantz, 2002; Ort et al., 2003; Burgisser and Gardner, 2006). These latter studies suggest that the depositional systems in pyroclastic flows are controlled by complex relations between the transport systems and topography at different distances from the vent. These studies have been dedicated to investigate large-volume ignimbrites emplaced up to tens of kilometers from the vent, in order to define a comprehensive model of pyroclastic flow transport and depositional dynamics. Only a few AMS studies have been carried out on small-volume phreatomagmatic deposits (e.g. Incoronato et al, 1983; Zanella et al., 1999; Porecca, 2003).

### ***REGIONAL GEOLOGY (COLORADO PLATEAU)***

The Colorado Plateau (Fig. 1) is a tectonic block of continental crust characterized by a 3-5-km-thick section of flat-lying Phanerozoic sedimentary rocks (Tingey et al., 1991). The suite of sedimentary rocks overlies igneous and metamorphic rocks whose crystallization ages span 1.69-1.79 Ga, with Sm-Nd  $T_{dm}$  model ages ranging from 1.8-2.0 Ga (Condie, 1986; Bennett and DePaolo, 1987; Wendlandt et al., 1993).

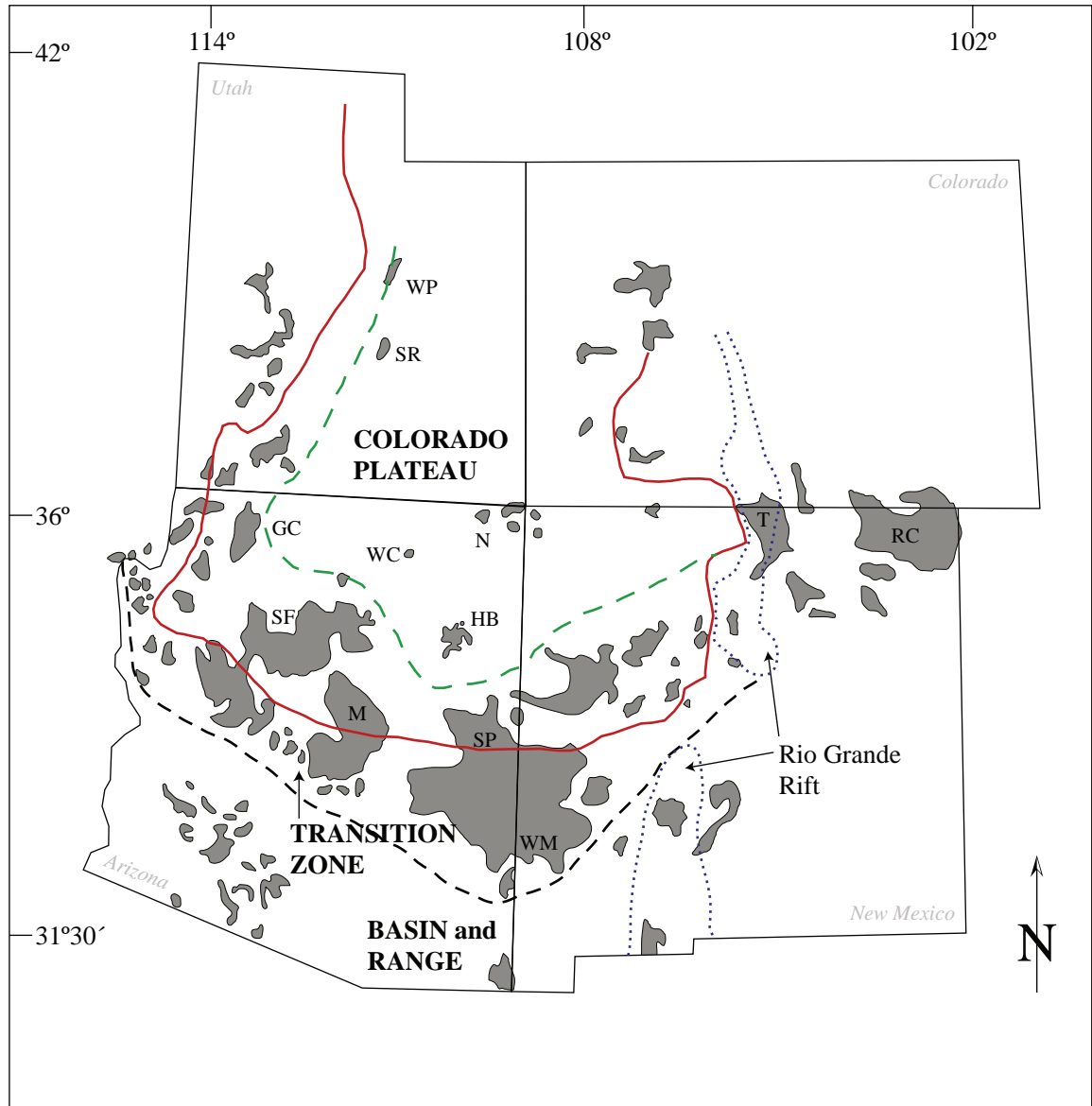


Figure 1: Distribution of middle to late Cenozoic volcanic centers in the southwestern United States. Solid red line represents the physiographic boundary of the Colorado Plateau. Dashed green and blue lines represent the geophysical boundaries of the Colorado Plateau and Basin and Range, respectively. Dotted blue line denotes the Rio Grande Rift. Volcanic fields are denoted by letters: GC, Grand Canyon; HB, Hopi Buttes; M, Mormon; N, Navajo; RC, Raton-Clayton; T, Taos; SP, Springerville; SF, San Francisco; SR, San Rafael Swell; WC, Wildcat Peak; WM, White Mountains; WP, Wasatch Plateau. Adapted and modified from Akers et al. (1971), Kempton et al. (1991), Tingey et al. (1991), and Delaney and Gartner (1997).

The Colorado Plateau has remained mostly unscathed throughout most of Phanerozoic time, experiencing only minor contractional deformation during the Laramide Orogeny (75-40 Ma) and extensional deformation during Paleogene time along its western and southern perimeters (Alibert et al., 1986). In contrast, many of the tectonic regions surrounding the Colorado Plateau, including the Basin and Range, Rio Grande Rift, and central Rocky Mountains, have experienced significant orogenic and magmatic activity throughout much of Cenozoic time.

Physiographic boundaries between the Colorado Plateau and neighboring provinces are varied. Physiographic transitions into the Basin and Range along the western margin of the Plateau are abrupt, accommodated through large normal faults such as the Hurricane and Grand Wash-Hunlock Fault systems. Spatial patterns and ages of volcanic centers across this edge of the Plateau suggest that magmatism has migrated eastward, following a generally eastward progression in active faulting (Maldonado and Nealey, 1995).

During late Neogene time (~10 Ma to present), tectonic activity migrated into the Transition zone and margins of the Colorado Plateau (Maldonado and Nealey, 1995). Increased seismicity and volcanism along the western boundary of the Colorado Plateau suggest that recent faulting in this region is in part responsible for elevating the Plateau to its present elevation ~ 2 km above mean sea level (Parsons and McCarthy, 1995).

In contrast, the interior of the Colorado Plateau remained quiescent and relatively unaffected by the widespread volcanism occurring along its margins. The few magmatic products on the Plateau that are contemporaneous with this phase of tectono-magmatic activity include Oligocene-Miocene syenite-diorite laccolithic complexes of the La Sal, Henry, and Abajo Mountains (Fig. 1; Nelson and Davidson, 1998), and isolated minette eruptive centers of the Navajo volcanic field (Laughlin et al., 1986; Severstone et al., 1999). Also, an isolated occurrence of a mid-Tertiary (20 Ma) nepheline monchiquite diatreme located at Wildcat Peak represents the only other temporally associated magmatism on the Colorado Plateau (Fitton et al., 1991).

During middle-late Neogene time (~17-5 Ma), the Colorado Plateau experienced a second phase of low-volume alkaline magmatic activity. Widespread calc-alkaline volcanism occurred during intervals of this time period along the physiographic margin

of the Colorado Plateau at the San Francisco, Mormon Mountain, White Mountain, Springerville, Mount Taylor and Jemez volcanic fields (Fig. 1; Kempton et al., 1991). The volcanic system that produced the nephelinites, monchiquites, and basanites of the Hopi Buttes volcanic field (Fig. 2) were active between 7.8 to 6.8 Ma and represent the most volumetrically significant volcanic activity on the geophysical Colorado Plateau during late Neogene time (Shafiqullah and Damon, 1985; Ort et al., 1998; Vazquez, 1998; Hooten, 1999a).

The Hopi Buttes volcanic field is a Mio-Pliocene intraplate volcanic field, whose eruptive centers are scattered within an 800 km<sup>2</sup> area of north-central Arizona (Fig. 2). The volcanic field lies within the south-central portion of the Colorado Plateau, an area that comprises nearly flat-lying sedimentary rocks of Paleozoic, Mesozoic, and Cenozoic age (Shoemaker et al., 1962; Sutton, 1974). Within the study area, the Mio-Pliocene volcanic rocks of the Hopi Buttes lie unconformably on the Triassic Moenave (TM) Formation (Billingsley, 2004). The lower member of the Bidahochi Formation (Tlb) is a sequence of siltstone and fine sandstone of lacustrine or playa origin, the middle member is composed of pyroclastic-surge deposits and silica-undersaturated mafic lava flows, and the upper member is sandstone and siltstone of eolian or fluvial origin (Regan, 1924; Repenning and Irwin, 1954; Vazquez, 1998).

Approximately 300 individual eruptive centers have been identified within the Hopi Buttes volcanic field (Fig. 2; White, 1991; Vazquez, 1999; Hooten, 1999b; Shafiqullah and Damon, 1986; Nealey and Sheridan, 1989; Damon et al., 1991; Ort et al., 1998). Mafic extrusive rocks range in composition from alkaline lamprophyre (monchiquite) to sodic nephelinite and basanite (Wenrich and Mascarenas, 1982; Ort et al., 1998).

The eruptive vents located along the eastern portion of the Hopi Buttes tend to have surficial features preserved (i.e. vent margins, debris aprons, and outflow deposits), whereas the western vents are typically eroded down to the sub-volcanic 'plumbing' (Ulrich et al., 1984, 1989). Early studies of this area (Williams, 1936; Sutton, 1974) argued for eruption into late Miocene-Pliocene (6-4 million years old) Lake Bidahochi (also called Lake Hopi), but White (1991) showed that, at least in some vents, there was no surface water present at the time of eruption and the phreatomagmatic activity resulted

from the interaction of melt with mud, rather than with water. White (1990) described the surface through which eruption occurred at the Hopi Buttes as a playa, with surface water only during seasonal wet periods. The interbedding of subaerial volcanic deposits with playa deposits at the Hopi Buttes reflects this year-to-year seasonal variation. However, the large number of hydrovolcanic events suggests a constant supply of water in saturated subsurface muds (White, 1990).

Dallegge et al. (2003) utilized  $^{40}\text{Ar}/^{39}\text{Ar}$  geochronology and geochemical correlation between extra-basinal tuffs to demonstrate that deposition of the lower Bidahochi Formation occurred between about 16 Ma and about 8 Ma, far earlier and over a longer period of time than previously thought.  $^{40}\text{Ar}/^{39}\text{Ar}$  dates within the middle member are about 7 Ma +/- 0.2 (Ort, unpublished data). Previous K-Ar dates on groundmass plagioclase separates place volcanism between 6.0 Ma and 8.5 Ma with no clear pattern of migration of magmatism with time (Damon & Spencer, 2000). Hoskietso maar, which gave a 4.2 Ma date, was later re-dated using  $^{40}\text{Ar}/^{39}\text{Ar}$  methods on phlogopite separates (Ort and Hooten, unpublished data). Their recent Ar/Ar data show these vents are between 6.9 Ma and 7.5 Ma.

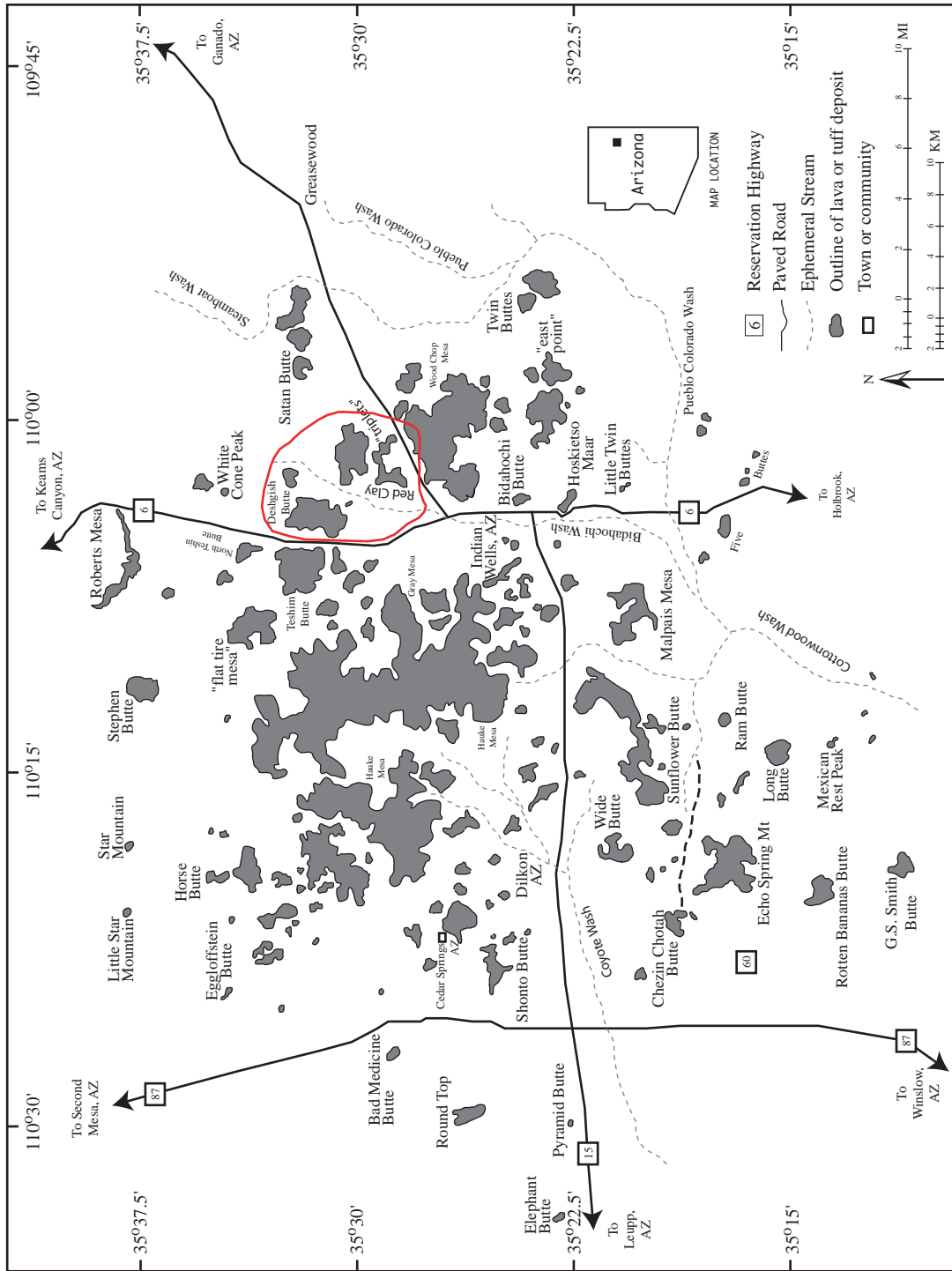


Figure 2: Map of the Hopi Buttes volcanic field. Red line denotes the present study area. Modified from Wenrich (1989).

## ***PHREATOMAGMATISM***

Phreatomagmatism, in the strict sense, includes a spectrum of volcanic processes resulting from the interaction between groundwater and magma (Sheridan and Wohletz, 1983; Wohletz and Heiken, 1991; White, 1996). When magma comes into contact with ground or surface water during its rise to the surface, thermal energy will be transferred through the magma-water interface. If the ambient pressures are below the critical value for water, the thermal transfer is reduced under stable vapor film boiling conditions (Fiedler et al., 1980). It is in this phase where molten liquids and water have the capacity to react violently (Zimanowski et al., 1997).

This reaction occurs during the interaction between molten material (fuel) and external (non-magmatic) water (coolant) in a process known as Molten Fuel-Coolant Interactions, or MFCIs (Wohletz and Heiken, 1992). Zimanowski et al. (1997) describes this process with four phases: 1) hydrodynamic premixing of water and melt under stable film boiling conditions; 2) quasi-coherent quantitative vapor film collapse in the premix leading to direct contact between melt and water; 3) fine fragmentation of melt and rapid increase of heat transfer in a positive feedback mechanism; and 4) system expansion and generation of superheated steam. Physical analysis of explosive magma-water interactions suggests that MFCIs largely control the style of fragmentation and explosivity in phreatomagmatic eruptions (Buchanan, 1974; Wohletz, 1986; White, 1996).

The dynamics of the interface between magma and wet sediments involves heat transfer at various rates, from passive quenching to explosive fragmentation (Wohletz, 2002). Prior to the onset of interaction, a vapor film develops at the MFCI interface, acting as a thermal barrier promoting the buildup of potential energy. Vapor film collapse at the fuel (melt) surface produces fragmentation in the melt and propagation of acoustic stress waves that promote further fragmentation (Wohletz, 1991; White, 1996). Combined with melt fragmentation, the rapid superheating of the water, now in direct contact with the magma, results in a far more energetic reaction than normal boiling, producing extremely explosive vapor expansion and vapor-rich eruptions (Wohletz and McQueen, 1984a).



Recent studies (e.g. Grunewald et al., 2007) have shown that water chemistry plays a vital role in the degree of explosivity. Laboratory studies show that melts interacting with saline brines produce reduced explosivity as compared to those that interact with pure waters. It is plausible that a spectrum of MFCI processes exists in the saline near-surface waters of playa or sabkha environments, and meteoric water and saturated sediments (Regan, 1924; Reppenning and Irwin, 1954). Variability of both solute content and MFCI process may produce a multitude of explosive responses.

### ***SURGE EMPLACEMENT MODELS***

Surges within the Hopi Buttes originated from phreatomagmatic and phreatic eruptions (White, 1996). During phreatomagmatic eruptions, Koyaguchi and Woods (1996) model a dilution of the collapse column caused by the initial entrainment of ambient air, which they find may suppress steam vaporization within a surge and facilitate a rise and segregation of finer-grained material, enhancing density stratification. Dilute density currents – pyroclastic surges – are multiphase transport systems composed of particles of various sizes and densities and dispersed gas, promoted by a complex interplay of phase change from steam to liquid water droplets.

The Vazquez and Ort (2006) model for Haskie Maar (also applied here to the Triplets and Deshghish Maars) for phreatomagmatic surge emplacement contrasts with the emplacement model of Wohletz and Sheridan (1979), but is supported by models developed after the Wohletz and Sheridan (1979) model (e.g. Sohn and Chough, 1989; Chough and Sohn, 1990). Wohletz and Sheridan proposed that pyroclastic surges are emplaced by a progressively deflating surge that produces a characteristic facies progression. Their model suggests that a surge cloud is most inflated and turbulent in the proximal areas, and produces sandwave structures as a result of traction sedimentation. As the surge continues to spread radially, the surge cloud progressively deflates and produces massive and planar facies due to increasing inertial forces. Thus, an overall downcurrent facies progression of sandwave to massive to planar is produced according to the model of Wohletz and Sheridan.

Wohletz and Sheridan based their model on statistical analysis of surge sequences from multiple volcanoes. This approach is useful for large-scale refinement, however it

may over-generalize sequences representing variable eruptive phases and styles (Vazquez, 1998). Fisher and Schmincke (1984) suggested that the Wohletz and Sheridan (1979) model provides a good general summary of dominant flow processes through time at a given locality, but should not be directly interpreted in terms of active processes within a single surge.

Studies of phreatomagmatic deposits from Korea (Sohn and Chough, 1989; and Chough and Sohn, 1990), and Italy (Colella and Hiscott, 1997) have employed detailed stratigraphic approaches, but have not traced surge progression within single, laterally-continuous units. Emplacement models derived from the vertical and lateral facies successions suggest that deposition occurs through an initially dense surge that becomes very turbulent and density-stratified at medial distances due to sedimentation, and finally deflates in distal areas due to deceleration and dilution.

Sohn and Chough (1989) and later, Vazquez and Ort (2006), explained sequential base-surge processes that progress through three general stages of transport and sedimentation and are controlled by the listed variables through time. Progressively, the stages are: (1) initial over-capacitated stage, (2) inflated and stratified stage, and (3) final deflating stage (Fig. 3). The proximal to distal facies produced by these surges progress from massive to sandwave to planar, contrasting with the Wohletz and Sheridan (1979) model. The facies succession of phreatomagmatic units at Haskie, Triplets, and Deshghish Maars appear to support the more recent models.

### ***SURGE EMPLACEMENT PROCESSES***

Stage 1, the initial over-capacitated stage, is produced at the inception of a phreatomagmatic eruption. Base surges (Fig. 3A) may result from a lateral blast or the collapse of low buoyancy eruption columns, due to high steam and tephra contents in the column. The term ‘base surge’ was originally applied to the radial outward motion of basal clouds observed and photographed in nuclear explosions, which Moore (1967) linked to similar features observed during the Taal 1965 eruptions. At its onset, the base surge is highly turbulent and uniformly mixed due to the initial explosive blast and high

thermal energy, leading to turbulent convective circulation of the cloud (Cas and Wright, 1987). The surge is a high-concentration suspension (Fig 3A). As the surge spreads radially away from the vent, it will rapidly lose its sediment load due to deposition from dense suspension (Sohn and Chough, 1989). Generally nonstratified and poorly-sorted lapilli-tuff deposits will be produced proximal to the vent; these early tuffs may construct tephra rings and cones (Fig. 3A; Wohletz and Sheridan, 1983; Sohn and Chough, 1989). As the surge propagates into a laterally-moving flow, poor stratification develops; depositional features suggest a stratified “bipartite” eruption unit that is dominated by a massive, structureless bed and capped by a thin, finer-grained layer (Vazquez and Ort, 2006).

Stage 2 is an inflated and stratified flow. As the surge advances down-current, segregation produces a basal traction-carpet and the surge becomes unsteady, density stratified, and highly turbulent (Fig 3B; Vazquez and Ort, 2006). The lower concentration flow overlying the traction carpet is characterized by suspension and saltation transport; separation of the traction carpet and the turbulent flow occurs as a result of sediment loss and dilution due to mixing with ambient air (Sohn and Chough, 1989; Vazquez and Ort, 2006).

Numerical and theoretical studies suggest that pulses are likely to develop in turbulent surges, as well as internal waves and vortices that permeate the surge current as local manifestations and continuous hydraulic structures (Valentine, 1987; Sohn and Chough, 1989). As a base surge continues downcurrent, it will become progressively more diluted as a result of debulking of the flow and the incorporation and expansion of ambient air (Laval et al., 1988). Decreased particle concentration facilitates turbulent

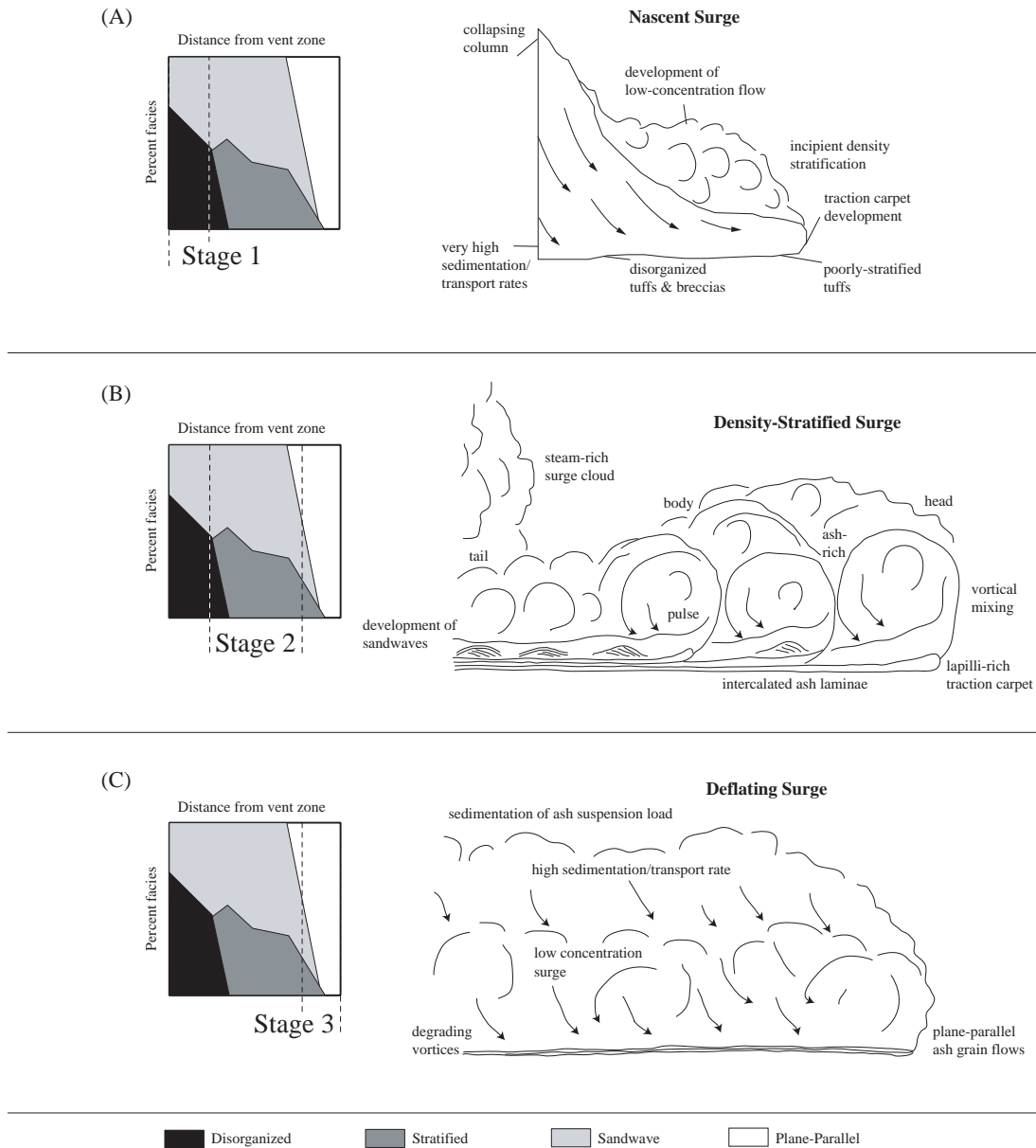


Figure 3: (A) In stage 1 of surge emplacement, collapse of low buoyancy column produces an overcapacitated surge current that overcomes the initial steam base surge. Near vent sedimentation occurs through a combination of fall back and poorly-developed lateral transport processes. (B) During stage 2 of surge development, the surge has undergone flow transformation into an underlying dilute flow that progressively grades downward into a traction carpet. Organization of internal vortices and waves causes the surge to develop pulses, and produce variable traction carpet stratification. (C) In the final stage of surge development – stage 3 – the surge is dilute and has lost much of its sediment load. Deceleration and condensation cause rapid fallout of cohesive ash that aggrades as grain flows. Lateral movement is sustained by degrading vortices and waves. This stage represents the waning character of each surge at the most distal locations.

activity (Fisher, 1979). The highly concentrated and uniformly mixed nascent surge of Stage 1 may transform into several large turbulent eddies or pyroclastic surges, *sensu stricto*, that are time-transient and unsteady, and occur as a series of pulses (Fig 3B). Individual pulses will produce distinct beds, and/or laminae, depending on flow power, particle concentration and pyroclast size. Interbedded ash laminae and basal lapilli-tuff beds form as individual pulses aggrade and override fine-grained tephra material deposited behind the head of the preceding pulse (Vazquez, 1998; Vazquez and Ort, 2006).

The overlying dilute flow is characterized by turbulent grain-support and saltation processes. Turbulence is quantified by the Reynolds number,  $Re = \frac{VD}{\nu}$  or  $Re = \frac{\textit{inertial}}{\textit{viscous}}$  where V is the mean fluid velocity (m/s), D is the diameter (m), and  $\nu$  is the kinematic viscosity ( $m^2/s$ ). Gravitational forces, thermal energy from juvenile pyroclasts, the latent heat of gaseous water condensation, and a continual decrease in particle concentration due to density segregation and dilution of the inflated overlying flow provide the pulsating change of energy for the laterally propagating flow (Fisher, 1979; Cas and Wright, 1987; Sohn and Chough, 1989). As the surge migrates, the eruptive pulse loses kinetic and potential energy due to continued dilution and condensation-induced cohesion (Fisher, 1979; Cas and Wright, 1987; Sigurdsson et al., 1987). The lower particle concentration in the overlying flow creates a viscosity contrast with the underlying traction carpet, which in turn causes a disparity in velocity and enhancement of density stratification (Sohn, 1997).

Although the resultant surge has become inflated and highly turbulent at this point, due to sediment loss and dilution, the surge is also decelerating due to decreased density and momentum (Vazquez, 1998). Cas and Wright (1987) purport that, at this stage, the surge becomes laterally partitioned into recognizable head, body, and tail sections. The partitioned body represents the bulk of the flow, with the highest mass, velocity and momentum. At the head, the body is circulated upward and diluted by Kelvin-Helmholtz instability waves along the margins of the surge top (Allen, 1982). The tail is generally the slowest portion of the surge, and has a lower sediment-carrying capacity than the body, resulting in a continuous fine-grained bed that caps the eruption

unit (Cas and Wright, 1987). Vazquez (1998) suggests that a change from supercritical to subcritical deposition in ash-rich sandwaves in surge deposits represents the transition from the body to tail sedimentation.

Stage 3 is distinguished by the waning flow and ultimate deflation of the transient surge (Fig. 3C). Progressive sediment loss and deflation in prior stages cause the surge to decelerate and decrease in particle concentration. Particles, which were entrained within the flow at earlier stages, begin to rain down as moist clumps. High moisture content in this stage is evident by the appearance of impact sags beneath lapilli- to ash-sized pyroclasts and widespread occurrence of diffuse bed contacts (Vazquez, 1998).

Continuous lateral motion and pulsating and periodic vortices cause the sediment grains to be deposited as distinctive grain layers that show evidence of shearing and development of low-angle bedforms (Cas and Wright, 1987). Individual grain layers shear along and locally scour underlying beds, producing low-angle truncations of strata. Due to a continuous loss of coarse grains in previous stages, the traction carpet now has a similar grain size to the overlying dilute flow, and bipartite phases can coalesce into a single transport and depositional unit at this distance from the vent. Vazquez (1998) describes deposits produced by this as plane-parallel beds with alternating beds and laminae of a generally structureless nature, but with evidence of shearing.

Vazquez (1998) determined that the facies concentrated in the distal section of the Haskie Maar eruption sequences are deposited in this stage. Beyond the Haskie Maar outcrops, the surge would have lost the bulk of its sediment load and momentum, caused by continual lateral motion, dilution and particle sedimentation. This ultimate 'surge death' is typically represented by plane parallel, very thinly bedded to finely laminated ash-tuffs. These deposit characteristics are not recognized in the preserved Haskie Maar sequence; it is likely that these deposits occurred beyond the spatial limit of preserved exposures.

Distal deposits are observed elsewhere throughout the Hopi Buttes volcanic field. These deposits are generally comprised of finely laminated ash and are easily reworked, eroded, covered up, or completely destroyed by subsequent deposition. This makes tracing individual distal surge deposits to their origin difficult because of the high spatial

and temporal concentration of volcanic activity during the life of the Hopi Buttes volcanic field.

### ***DEPOSITIONAL PROCESSES AND FACIES***

Phreatomagmatic surge deposition is a consequence of energy change and proximity to the eruptive vent. The observed lateral and vertical facies variations are representative of these changes in energy within the flow. Facies analysis reveals that pyroclastic sequences of Hopi Buttes surge deposits can be represented by four generalized groups. The groups are generally comparable to those used by other workers (e.g., Wohletz and Sheridan, 1979; Sohn and Chough, 1989; Chough and Sohn, 1990; Lajoie et al., 1992; Colella and Hiscott, 1997) for their facies analyses of base-surge deposits from small basaltic and rhyolitic volcanoes. The facies are designated as: (1) a proximal disorganized to diffusely stratified zone, (2) a proximal-medial stratified zone, (3) a medial sandwave-bearing zone, and (4) a distal plane-parallel zone (Vazquez, 1998; Vazquez and Ort, 2006).

Across the Hopi Buttes, individual eruptive units exhibit similar facies successions with increasing distance from their eruptive vents. Despite variation between eruptive units resulting from the eruption type and the unique dynamics of eruption size, the ratio of the water to water-saturated sediments present, and the overall explosivity of the eruption (Vazquez and Ort, 2006), several similar facies groups have been observed within the study area. The Triplets maar has mapable units extending ~1000m from its inferred eruptive vent; the Kohl maar produced deposits extending well beyond ~1800m from the inferred eruptive vent (Plate 1).

Proximal facies eruptive units (within 400 m of the vent) are dominated by the disorganized to diffusely stratified group 1 (Fig 3A). Medial facies, ash tuffs from sandwave-bearing facies group 3 (distances 400-1000 m from the vent), develop above facies group 1, as secondary eruptive pulses deposit material with the continual collapse of the eruption column (Fig 3B). Between 400 and 600 m from the vent, the disorganized to diffusely stratified facies at the base of each eruption unit transforms into the stratified facies group 2. This vertical succession (stratified facies group overlain by sandwave facies group) is characteristic of eruption units at medial locations (Fig 3B). At distances

≥ 900 m, the upper portions of the eruption units transform into the sandwave or plane-parallel facies. At distal locations (> 1000 m from the vent), the stratified facies group from the lower portions of each eruption unit increasingly transform into plane-parallel facies (Fig 3C). At the most distal outcrops (> 1200 m), eruption units are composed entirely of the plane-parallel facies group.

Laterally contiguous facies successions have varied distances and intertonguing relations that may differ from the gross facies occurrence for the entire sequence, reflecting the slightly different runout distances, eruption foci and bed thickness of individual eruption units. Lateral and vertical facies transitions within single eruption units suggest that, as single surge currents traveled away from the vent, they transformed through three general stages of transport and sedimentation: (1) an early overlaid and diffusely stratified stage, (2) an inflated and density stratified stage, and (3) a final deflating stage when pyroclasts rapidly decouple from the surge current (Fig 3A, B, C; Vazquez and Ort, 2006).

### ***PROJECT SIGNIFICANCE***

The study area for this project is approximately 64 km<sup>2</sup> in the eastern part of the Hopi Buttes volcanic field (Fig. 2). Part of this area was mapped at scale of 1:12,000 for United States Geological Survey (USGS) EDMAP Grant 03HQAG0048, and part at a 1:6,000 scale, to illustrate small features. All mapable units were identified and recorded within this area, with additional volcanoes outside of the map boundary examined for specific indicators of surge emplacement processes. The eastern portion of the Hopi Buttes volcanic field, including the present study area, is unique in its variety of outcrop exposure. Accelerated erosion in this portion of the field reveals a spectrum of phreatomagmatic deposits, from surficial maar and tuff ring edifices, to the root zone and associated tuffaceous pyroclastic facies. The maar-diatreme exposures within the Hopi Buttes area are some of the best in the world and provide an excellent location for the study of surge facies.

The greater study area is included in Indian Wells, White Cone, Greasewood Spring, and Satan Butte USGS 7.5 minute topographic quadrangles. Vazquez (1998) mapped the Haskie Maar, located in the southeastern corner of the study area, at a similar



scale with emphasis on identification and description of various pyroclastic facies. This previous work provided valuable field-based data for the interpretation of anisotropy of magnetic susceptibility (AMS) fabrics. The present study refines previous depositional models by providing textural control and further insight into internal depositional processes through the incorporation of quantitative AMS analysis.

Specific objectives of this project were to: 1) construct a detailed geologic map and describe lateral facies transitions of pyroclastic deposits away from the eruptive source; 2) provide textural analysis of groundmass fabrics and anisotropy of magnetic susceptibility (AMS) within individual laterally continuous deposits; and 3) propose a detailed microscopic to mesoscopic model for the depositional and emplacement dynamics of surge processes.

## CHAPTER 2: PROJECT METHODS

---

### ***FIELD METHODS***

Field mapping at 1:6000 scale within the sample areas at the Hopi Buttes was conducted in order to locate individual pyroclastic surge deposits (Plate 1). Several mapped locations afforded pristine lateral sections in which specific sites were designated for further analysis. These sites were described in detail with respect to their vertical and lateral facies and sampled for paleomagnetic analyses. Results from paleomagnetic analyses were then employed for interpretation of magnetic fabrics, which presumably correspond to the depositional rock fabrics.

### ***MAGNETIC METHODS***

The paleomagnetic properties used to interpret the Hopi Buttes phreatomagmatic surge deposits are Anisotropy of Magnetic Susceptibility (AMS) and Characteristic Remanent Magnetism (ChRM). AMS was analyzed to determine the magnetic fabrics within the individual cores; as a non-destructive process, this is the first step in paleomagnetic analysis. As a second step, the ChRM for many samples was obtained in order to determine the baseline orientation of the samples and recognize any potential structural rotations of the deposits. The ChRM resets the magnetic memory, thus rendering the core useless for most other paleomagnetic analyses.

#### *Magnetic Remanence*

Characteristic remanent magnetism (ChRM) is the in-situ magnetic field of geological materials, and is typically composed of more than one component. The primary component is the direction of the magnetic field acquired during formation. Primary NRM may be a product of three main processes in rocks that have not experienced hydrothermal alteration: 1) *thermoremanent magnetization (TRM)*, acquired during cooling from high temperature; 2) *chemical remanent magnetization (CRM)*, formed by growth or change of ferromagnetic grains below the Curie temperature; and 3) *detrital remanent magnetization (DRM)*, acquired during accumulation of sedimentary rocks containing detrital ferromagnetic minerals. Thermoremanent magnetization is

typically the most pervasive magnetization process in volcanic rocks. During crystallization, the local geomagnetic field,  $H$ , imprints the local magnetic field on the rocks according to the equation  $J_r = \chi H$ . Bulk susceptibility,  $\chi$ , is the net susceptibility resulting from contributions of all minerals, but is typically dominated by ferromagnetic minerals.

Secondary NRM components may be acquired subsequently and can alter or obscure primary NRM. These secondary components of NRM may add vectorially to the primary NRM to produce a hybrid or total NRM (NRM = *primary* NRM + *secondary* NRM). Acquisition of induced magnetization is also a reversible process without any memory of past magnetic fields. Such reversals may be induced by chemical alteration processes, rapid electromagnetic flux (lightning strike) and long-term exposure to a geomagnetic field subsequent to rock formation. As a paleomagnetic analysis tool, RM reveals the strength and direction of the primary local magnetic field induced in the ferromagnetic fabric of a rock during crystallization. In the laboratory, RM values are measured using an artificially applied magnetic field. The constructive interference measured in this environment is a vector whose value is the sum of two components:  $J = J_i + J_r$ , where  $J_i$  is the known experimentally induced magnetic field and  $J_r$  is the natural remanent magnetism. Stepwise alternating field demagnetization takes out parts of the magnetic remanence, with the late-formed remanence typically coming out at lower levels of demagnetization. Typically, the characteristic remanent magnetization is found during analysis of the sample after higher steps in the demagnetization process.

### ***Anisotropy of Magnetic Susceptibility (AMS)***

The measurement of the low-field anisotropy of magnetic susceptibility (AMS) of rocks is a rapid and non-destructive method to obtain information about the fabric of rocks. The AMS depends on the anisotropy of each mineral and the spatial arrangement of grains within the rock.

The magnetic susceptibility,  $k$ , is the dimensionless scaling factor between the two fields ( $\vec{M} = K\vec{H}$ ), where  $M$  is the induced magnetization of the sample from an external field  $H$ . When  $k$  varies with the direction of  $H$ , the material is anisotropic for magnetic susceptibility. In this case,  $k$  is a second-order tensor that can be expressed in

terms of a triaxial ellipsoid, in which the greatest intensity is induced along the long axis ( $K_1$ ) and the weakest intensity induced along the short axis ( $K_3$ ) (Nye, 1985). The bulk susceptibility of a single sample is defined as  $K = (K_1+K_2+K_3)/3$ , where  $K_1>K_2>K_3$  are the principal susceptibilities measured in SI units (Tarling and Hrouda, 1993).

The overall AMS fabric of a material depends on the anisotropy of the magnetic mineral carrier it contains, and the spatial relation/interaction between proximal particles. Typically, AMS analysis shows a 0.5 to 5% detection of overall anisotropy of individual specimens. This relatively low detection level can be a function of two rock features: 1) a product of several detectible aspects within the rocks, 2) a function of considerable anisotropy within a few single particles. The values measured could be only a function of minor amount of anisotropy of the shape of the magnetic particles, or a case of only a few being elongate and oriented, or of only a few being in contact to make a distribution anisotropy. Shape anisotropy is affected by the shape of an individual mineral grain. A magnetized body will produce magnetic charges or poles at the surface. This surface charge distribution, acting in isolation, is itself another source of a magnetic field. Magnetic interactions among neighboring magnetic carriers may be anisotropic if the grains are not uniformly distributed throughout a matrix; such spatial distributions are referred to as 'location fabrics' and the resulting AMS has been termed 'distribution anisotropy' (Hargraves et al., 1991). The shape-preferred orientation of magnetic grains is the main source of the AMS in magmatic rocks and lavas (Cañón-Tapia, 2002). The shape distribution orientation of magnetic mineral carriers is another source of AMS and is generally used in the interpretation of pyroclastic rocks where distribution may be more important.

The origin of AMS fabric in pyroclastic surge deposits and ignimbrites is still under debate. Hrouda (1982) and Tarling and Hrouda (1993) interpreted AMS fabrics in ignimbrites as resulting from a preferred orientation of elongate ferromagnetic grains that moved within the flow. Wolff et al. (1989) and Hargraves et al. (1991) suggested that magnetite grains can form around or aggregate along the edges of elongate glass shards and, if two or more grains are in direct contact, such interaction can create the anisotropic fabric detected in ignimbrites. Le Pennec et al. (1998) present several possible ways to

form the AMS fabric and argued that the nature of the AMS fabric in one sample may not necessarily be the same as in another sample from the same unit.

A wide range of parameters has also been used to describe AMS shapes, equations relating the lengths of the individual K axes to familiar petrologic terminology. These include lineation ( $L=K_1/K_2$ ), foliation ( $F=K_2/K_3$ ), and degree ( $P=K_1/K_3$ ). The shape factor values ( $T = \left[ \frac{2\ln(K_2/K_3)}{\ln(K_1/K_3)} \right] - 1$ ) describe the susceptibility ellipsoid, where values  $0 < T < 1$  represent oblate (disc) shaped, and  $-1 \leq T < 0$  indicate prolate (rod) shaped particles.

Of all the textural parameters, the AMS axis  $K_1$  offers the greatest insight into the depositional processes, followed by the orientation of the  $K_3$ . The orientation of the  $K_1$  axis offers a visual key to the overall alignment of particles within the rock, and a conceptual framework for their transport history and depositional processes;  $K_1$  axis signatures can be used to decipher a locally turbulent vs. laminar flow history. In a turbulent flow, prolate particles would be transported by rolling ( $K_1$  axis perpendicular to flow direction), and oblate particles would likely move through tumbling and/or saltation ( $K_1$  axis parallel to flow). By contrast, a  $K_1$  axis parallel to flow in a laminar flow system would signify particle alignment and transport by the dominant shear vector. Consequently, the directional orientation of the  $K_1$  axis in relation to particle shape can constitute a robust proxy for flow type. The  $K_3$  axis may offer additional insight into depositional processes, indicating the degree of imbrication, particularly within oblate fabrics.

## ***ANALYTICAL METHODS***

Rock-magnetic samples from 30 sites in the Hopi Buttes were analyzed for ChRM (11 sites) and AMS (30 sites). The term “site” refers to a part of a single outcrop (10-30 cm *tall* by 20-50cm *wide*) within a cliff face. The site locations were distributed based upon distance from the inferred eruptive vent; sites were selected from various visible facies units defined by Vazquez and Ort (2006). Sample sites were located in the basal portion of the individual eruptive surge beds. At each site, the sense of flow was inferred from the macro- and mesoscale flow markers and facies based on the Vasquez and Ort

(2006) depositional model. At each site, 1-2 large block samples (~30-60 cm (l) x ~10-20 cm (w) x ~10-30 cm (h)) were collected by hand and oriented with a magnetic and solar compass. These large blocks were extracted from the cliff face by pre-drilling a rough block outline. In order to re-orient field samples in the laboratory, an aluminum ring was secured parallel to the cliff face by an epoxy bond and measurements of strike and dip were recorded for precise alignment. After the pattern was drilled out and orientation was documented, the final extraction was completed with a hammer and hardened steel chisel.

The large bulk samples were brought to the laboratory, placed in aluminum baking trays, and set in plaster of Paris to retain their original orientation. From the block(s) collected at each site, a drill press with a coring bit extracted 6-16 individual cores, located several centimeters apart from one another along the determined sample layer. Subsamples for paleomagnetic analysis (10-15) were extracted as short core segments (standard cylindrical specimens 25.4 mm diameter x 22 mm length).

AMS measurements were conducted at the University of New Mexico Paleomagnetism Laboratory (UNMPL) in Albuquerque, New Mexico, using a Kappabridge KLY-4. The Kappabridge KLY-4 (MFK1-FA) has a sensitivity of  $3 \times 10^{-8}$  SI (bulk susceptibility) and  $2 \times 10^{-8}$  SI (anisotropy) with an operating frequency at 960-15616 Hz, field homogeneity of 0.2%, a measuring range of up to 0.5 (SI), and an accuracy within one range of +/-3%. For the AMS determination, the specimen susceptibility is measured in 15 different positions following the KLY-4 standard operating procedure of rotatable design (i.e. core axis oriented perpendicular, parallel, and vertical to the core holder). The positions are changed manually and the susceptibility tensors are calculated, including statistical errors. The AMS values for all specimens were evaluated using the Anisoft AMS data analysis software written by Martin Chadima and Vit Jelinek for Agico Inc. (available online at [www.agico.com](http://www.agico.com)) and Jelinek statistics (Jelinek, 1977).

Magnetic remanence analysis was conducted in the paleomagnetism laboratory at Northern Arizona University, Flagstaff, Arizona, using a Molspin Ltd "Minispin" rock magnetometer and shielded alternating-field demagnetizer. Alternating-field demagnetization (AFDemag) is used to erase remanence components of low coercivity

and low reliability in order to backstep and examine the orientation history of the surge deposits. Specifications for the Molspin Ltd “Minispin” are as follows; *specimen size* can be up to 1" x 1" (2.54 cm) cylindrical in shape. The process has an *integration time* of either 6 seconds (24 spins), or 24 seconds (120 spins), and a detection *sensitivity/noise level*:  $2.5 \times 10^{-8}$  EMU.CM-3 ( $2.5 \times 10^{-5}$  A/m) for 4 spins at the 24 second s time constant.

## CHAPTER 3: VOLCANIC FACIES, VOLCANO DESCRIPTIONS and FIELD INTERPRETATIONS

---

### *STANDARD FACIES FOR VOLCANIC SEQUENCES*

Detailed measurements and observations were made on exposed sections (12 sections at Haskie Maar, 12 Sections at Triplets, and 11 at Deshghish Butte) along the cliff faces of the Hopi Buttes (Plate 1). Phreatomagmatic surge sequences are represented by 10 sedimentary facies based on grain size and sedimentary structures. The classification scheme is based on Vazquez and Ort (2006) and modified from Sohn & Chough (1989).

#### *Facies LT1: Disorganized and Poorly Stratified Lapilli-Tuff*

Facies LT1 comprises single beds of green, fine- to medium-grained, poorly-sorted ash-poor lapilli tuff with no or poor stratification (Fig. 4). Upper contacts are flat, whereas lower contacts undulate and scour underlying beds. Bed thickness averages 25 cm and is greatest in lows in the substrate. In source-proximal locations, this facies is structureless, whereas farther downcurrent, reverse grading occurs in basal portions (approximately 5 cm) or throughout the bed. Poor internal stratification is defined by grain-supported lapilli trains. Small blocks and coarse-grained lapilli are abundant throughout the matrix-supported lapilli tuff on this facies. Pyroclasts are dominated by matrix-supported, juvenile lapilli with scattered, coarse-grained lapilli and small blocks. Crude alignment of elongated pyroclasts exists parallel to bedding planes in poorly-stratified examples.

Ballistic blocks and bombs are common in this facies, in many cases accompanied by impact sags. Impact sags are typically associated with blocks located at the base of beds, with infilling by overlying lapilli tuff. Blocks within the body of the bed typically have their maximum and intermediate axes parallel to bedding, and are not associated with significant sags. Coarse-grained lapilli are concentrated in the lows produced by impact sags.



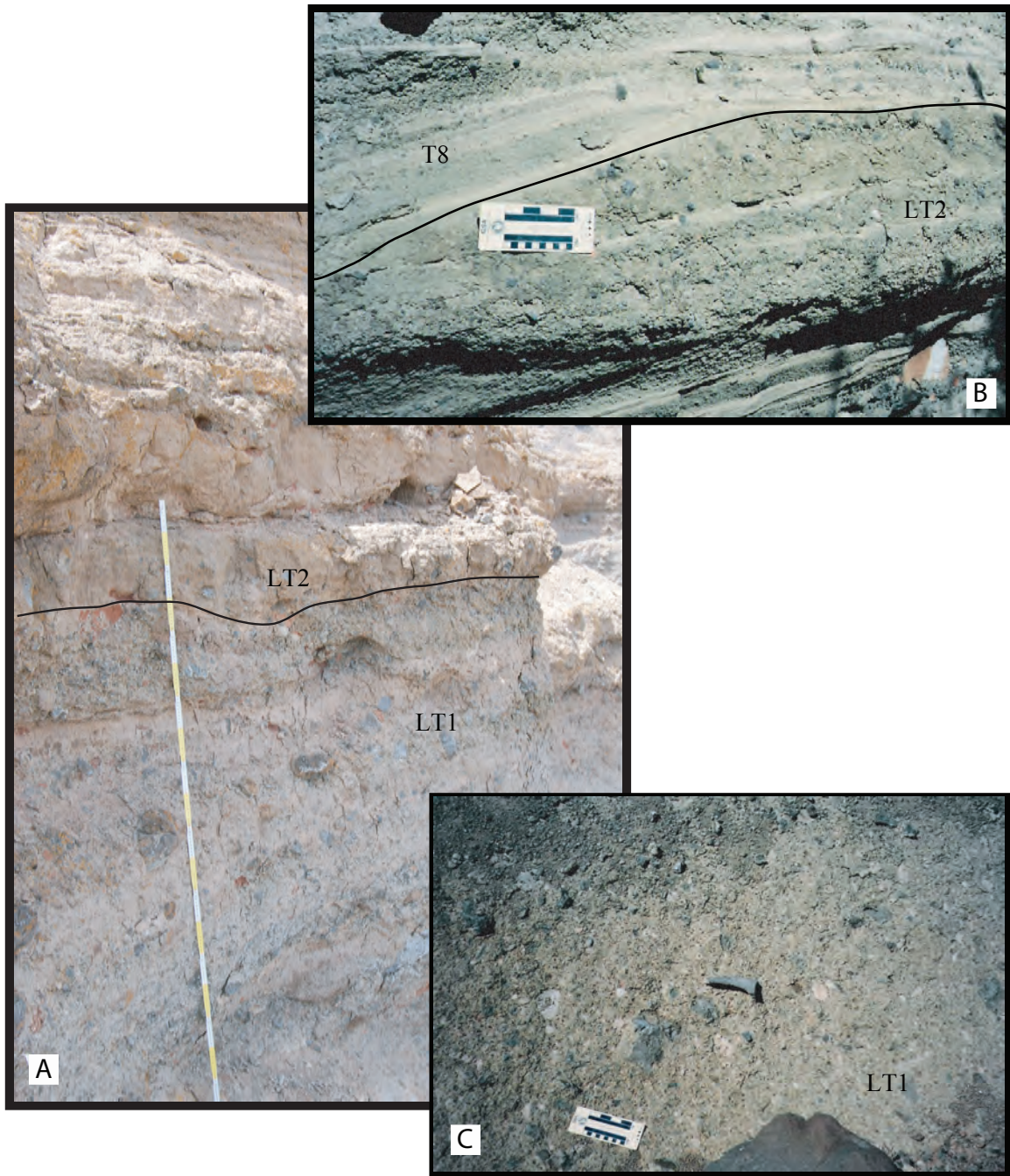


Figure 4: Photo (A) Facies LT1 overlain by facies LT2 located at the Triplets site TP0. Inset photo (B) Facies LT2 is a lapilli tuff, note the intercalated ash laminae. Facies T8 is overlain by Facies LT2 bed (basal part of bed 2E). Photo was taken near site HM1. Inset photo (C) Facies LT1 is from Haskie maar, note highly disorganized nature. Most of the proximal facies are composed of the LT1 facies. Note the poorly stratified ~25 cm LT1 beds and lapilli trains in LT2. Current direction is right to left. Inset photos are modified after Vazquez (1998).

*Facies LT2: Moderately stratified lapilli-tuff*

Facies LT2 comprises green, medium-grained, juvenile-rich, poorly-sorted lapilli tuff containing internal framework-supported lapilli trains and distinctive internal stratification (Fig. 4). Top contacts are generally flat, and bottom contacts are undulatory with local scouring of underlying beds. Bed thickness averages 20 cm, and is greatest where it swells downward to include infilling into underlying sag depressions. A 2-3 cm cone of reversely-graded lapilli is typically located at the base. The upper portion of beds typically exhibits normal grading. Pyroclast type is dominated by juvenile lapilli, with rarer accidental inclusions of Bidahochi mudrocks and Moenave sandstone. Elongate lapilli show crude upcurrent imbrication of long axes.

Lapilli trains are abundant and are planar to lensoidal with reverse grading. In addition to lapilli trains, stratification is defined by intercalated tan ash laminae. These ash laminae are typically laterally discontinuous, with an average thickness of 0.5 cm, and may exhibit bedforms. Diffuse, poorly-formed sandwaves may appear in the lapilli-sized portion of this facies, but are truncated by ash laminae. Ash laminae thickness increases over internal bed irregularities producing sandwave bedforms. These ash-rich bedforms are lee-erosive and stoss-depositional, and have amplitudes up to 14 cm with foreset dips that average 10 degrees. The ash-rich bedforms become best-developed approximately 1 km from the vent. Blocks and bombs are abundant in this facies. Blocks are associated with impact sags, especially those occurring at the base of beds. Larger lapilli are consistently concentrated in the lows of impact sags. Intact and broken fusiform bombs are typically scattered within beds, especially near the vent, but are not associated with impact sags.

*Facies LT3: Stratified undulatory lapilli-tuff*

Facies LT3 is characterized by green, medium-grained, poorly sorted lapilli-tuff with undulatory upper and lower contacts. Stratification is defined by internal bedforms and laminae. Average bed thickness is 6 cm, but bed thickness varies with bedform undulation in adjacent beds. Matrix ash content and degree of stratification increase upward. The basal few centimeters of this facies typically are reversely graded, whereas the upper portions of the beds are typically normally graded. Reverse grading is best

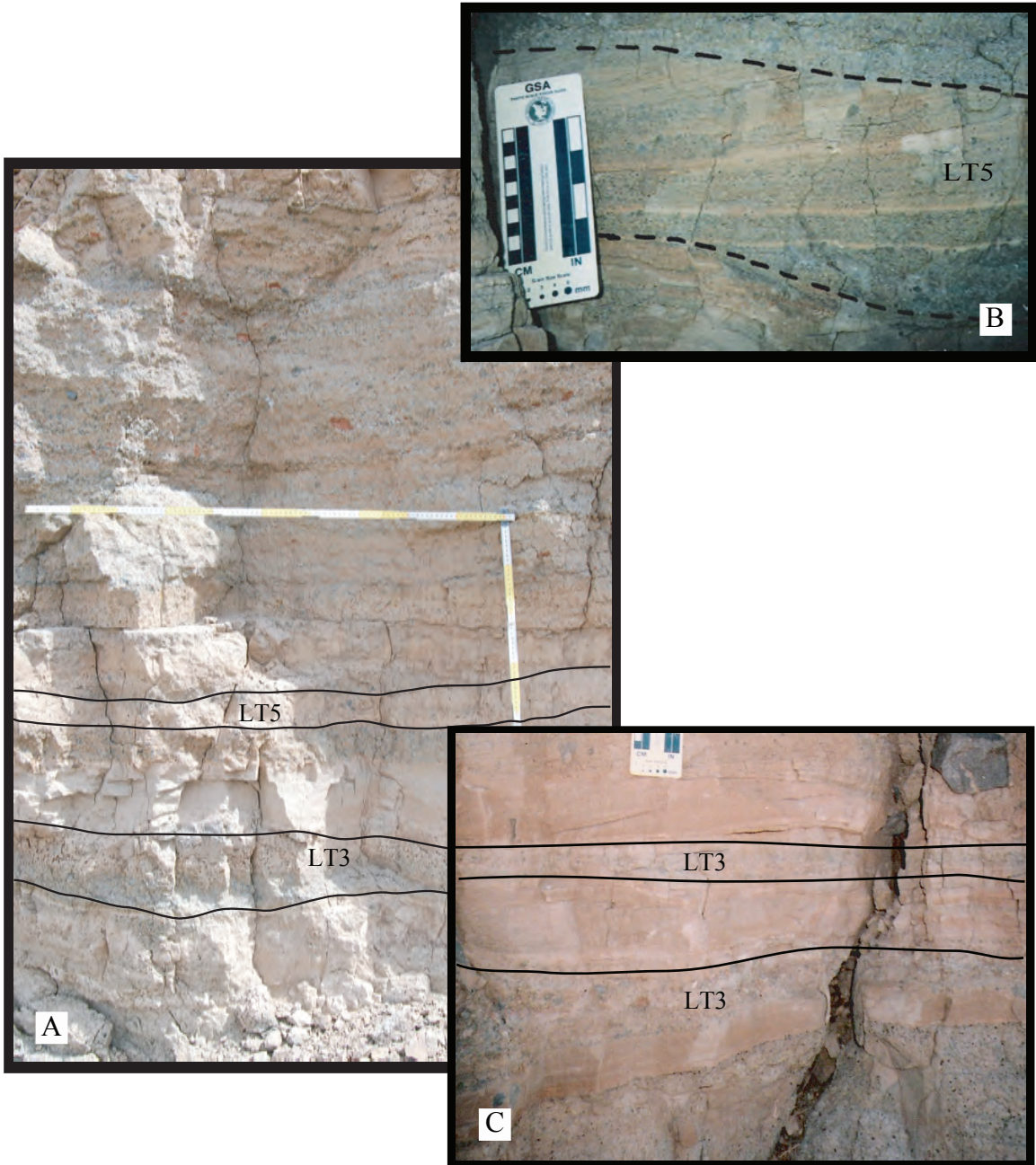


Figure 5: Photo (A) Facies LT3 overlain by facies LT5 is located at Triplets site TP6 . Inset photo (B) displays Facies LT5. The lower portions are richer in juvenile lapilli and upper portions contain well-developed bedforms. This facies is transitional from the juvenile-lapilli-dominated facies to the accidental-rich and bedform-bearing facies. Inset photo (C) is located at HM4 with facies labeled in the photo. Note the cyclicity of the juvenile (green) and accidental-rich (tan) beds. Inset photos are modified after Vazquez (1998).



developed in thick beds, localized in substrate lows. Intercalated ash laminae average less than 1 cm in thickness, and are typically discontinuous and bifurcated. Over lows, a single ash lamina may bifurcate into two laminae and then rejoin over highs, but without the development of sandwaves. Incipient sandwaves occur on the lee sides of the bedforms that formed the underlying beds (Fig. 5).

*Facies T4: Moderately stratified tuffs*

Facies T4 comprises thin beds of green, coarse-grained, moderately sorted, juvenile-rich ash tuffs with intercalated juvenile-poor, tan ash laminae and fine-grained lapilli trains. Average bed thickness is 7 cm. Ash laminae and short, localized lapilli trains define the stratification in this facies. On average, pyroclasts are coarse angular to sub-rounded ash. Basal contacts typically follow the undulations of underlying beds and are non-erosive. Upper contacts are flat.

Overall, this facies is normally graded, but crude reverse grading is characteristic of individual laminae and beds. Upper portions of this facies are poor in lapilli, and are dominated by ash. Ash laminae have a pinch-and-swell nature and bound small, low angle truncation surfaces; truncations locally cut underlying beds and laminae, but bounding ash laminae tend to be continuous.

*Facies LT5: Stratified undulatory tuff*

Facies LT5 comprises matrix- to framework-supported, moderately sorted, ash to medium-grained lapilli tuff. Average bed thickness is 4 cm. Upper contacts are flat and gradational with overlying ash tuffs of different facies. Basal contacts are locally erosive, and load underlying ash tuffs (Fig. 5, 6).

Overall, this facies is normally graded. The lower portions are typically framework-supported, medium-grained lapilli, dominated by juvenile pyroclasts with basal reverse grading. Upper portions are typically composed of matrix-supported, fine-grained lapilli to coarse-grained ash; much of the ash is accidental mud and silt. Abundant sandwaves characterize the upper ash portions with amplitudes up to 3 cm.

This facies differs from LT3 in that it does not contain well-developed stratification or intercalated ash laminae.

*Facies T6: Stratified undulatory juvenile-rich tuff*

Facies T6 comprises green, moderately well-sorted, coarse-grained tuff with internal stratification. Bed thickness averages 3 cm. Upper and lower contacts are typically undulatory, with characteristic bed thickening in lows and thinning over highs of underlying beds. Stratification is defined by continuous, intercalated, tan ash laminae. Bedforms are distinctly absent from this facies. Outsized lapilli, up to 2 cm, are abundant and produce small-scale asymmetric impact sags. Impact sags are filled by medium-grained lapilli. This facies occurs in distal sections, beginning approximately 1 km from the vent (Fig. 6).

*Facies T7: Erosional Sandwave-Bedded Tuff*

Facies T7 comprises tan, poorly to moderately sorted, fine to coarse grained ash tuff that is stratified and typically undulatory. This facies is dominated by accidental lithic fragments of mud and silt from the lower Bidahochi. Stratification is defined by discontinuous lapilli trains and abundant bedforms. Lapilli train beds are composed of fine- to medium-grained, framework-supported pyroclasts that may be reversely graded. Intercalated beds of very fine-grained ash, devoid of lapilli, also occur.

Bedforms in this facies are typically progressive, asymmetric to symmetric, stoss-erosional sandwaves. Beds show an overall upward trend of larger to smaller amplitude sandwaves. The lower sandwaves, the main body, have amplitudes up to 35 cm, whereas the upper sandwaves have amplitudes up to 9 cm. Large amplitudes are associated with beds in more proximal localities. Main body sandwaves are typically organized into cosets sharply truncated by overlying upper sandwaves. Upper sandwaves, initially stoss-erosive, invariably become stoss-depositional, as evidenced by continuous uppermost sandwaves. A thin, massive ash bed with soft sediment deformational structures typically caps the facies.

Accretionary lapilli, up to 8 mm, are concentrated in the sandwave foresets of several beds. These lapilli are composed of clay- to silt-sized cores with a thin mantle of

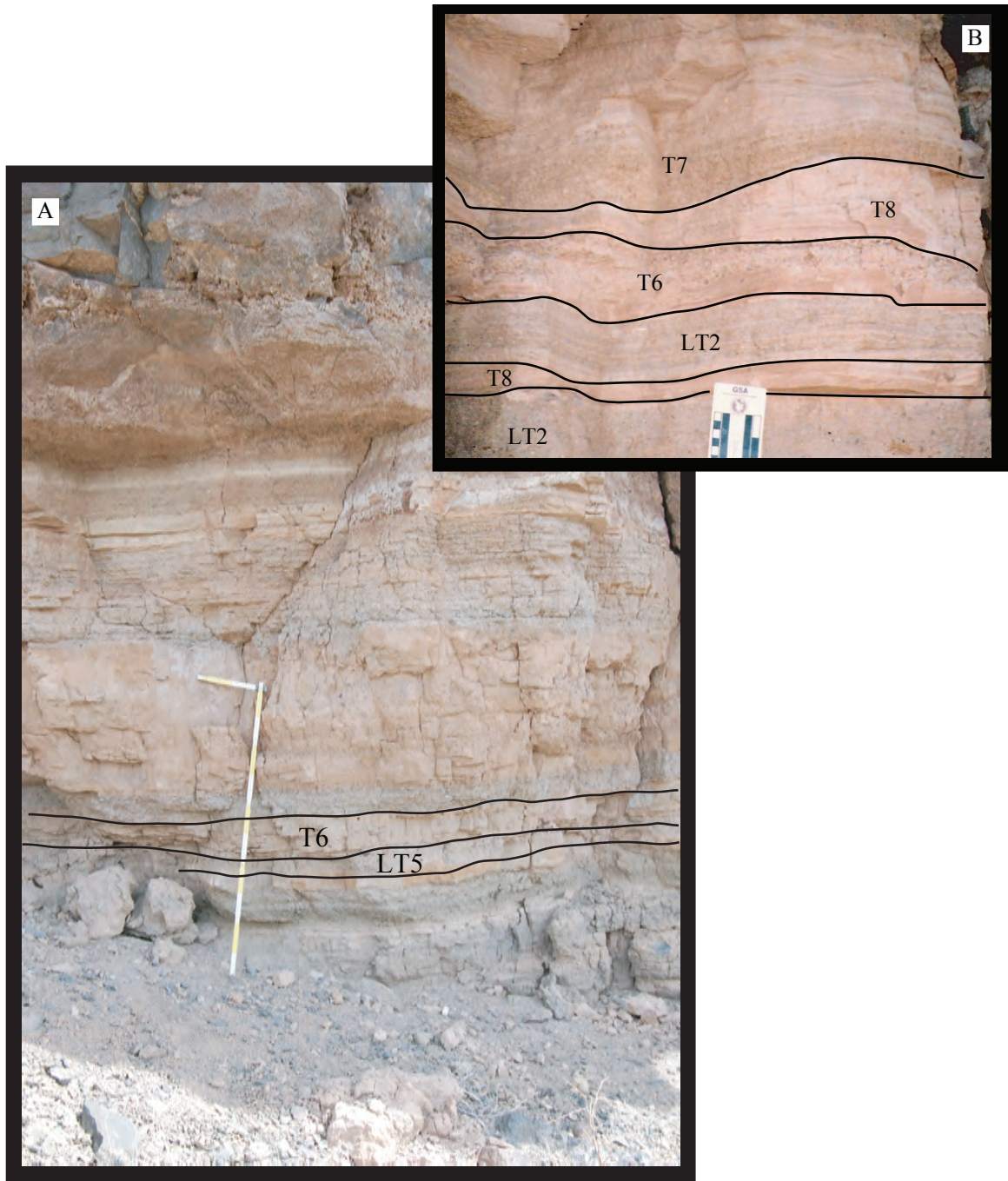


Figure 6: Photo (A) Facies LT5 overlain by facies T6 at the Triplets site T9. Facies T6 is a stratified undulatory tuff. Note the undulatory thin beds in T6, current direction is left to right. Inset photo (B) is taken near HM4 and displays distal tuff facies T6, T7, and T8. Note the cyclicity and fine laminations within the distal units. Current direction is left to right. Inset photo is modified after Vazquez (1998).

clay. Scarce accretionary lapilli are cored by juvenile ash. Deformation of accretionary lapilli by adjacent pyroclasts is common, although most are nondeformed.

*Facies T8: sandwave-bedded ash tuff*

Facies T8 is characterized by tan, poorly to moderately sorted, fine- to medium-grained tuff. This facies is very similar to facies T7, but lacks a progressive sequence of sharply truncated sandwaves. Beds contain abundant, well-developed sandwaves that typically form a solitary set with minimal bedform climbing. Stratification is defined by internal ash laminae and coarse-grained ash to fine-grained lapilli trains. Many trains are undulatory and show reverse grading. Overall, the facies show a normal grading of average pyroclast size, including trains. Lower bed contacts are flat and non-erosive, and upper contacts are very sharp.

Sandwaves in facies T8 are characteristically progressive, symmetric, and stoss-erosive, and contain concave-up foresets of coarse-grained ash to fine-grained lapilli. Amplitudes range from 5 to 25 cm, and are controlled by substrate irregularities; largest sandwaves occur on the lee sides of underlying bedforms. Amplitude tends to increase with proximity to source. A thin ash mantle caps this facies in places.

Loading and soft-sediment deformation structures are abundant along contacts and within facies T8. Small ballistic blocks and outsized lapilli create significant impact sags, and successive beds and laminae may “plaster” or mantle these obstructions. Overlying beds locally produce loading features such as flame structures. Large impact sags occur where blocks from overlying beds impact the tuff.

*Facies T9: planar-stratified tuff*

Facies T9 comprises tan, moderate to well-sorted, planar-stratified, fine- to coarse-grained tuff. Internal stratification is defined by alternating cm-scale, fine- to coarse-grained ash trains and discontinuous beds. Beds range from structureless to well stratified by interlaminated ash. Upper contacts are locally contorted, and are associated with small-scale flame structures; lower contacts mantle underlying beds. Stratification

is locally cross-cut by low-angle truncation surfaces, and well-developed bedforms such as sandwaves are absent. Ash trains locally pinch and swell, and comprise the coarsest grained component of this facies. Diffuse and distinct contacts between internal ash beds and laminae are also characteristic. Scattered, yet abundant, lapilli (up to 1 cm diameter) produce noticeable impact sags. Facies T9 is concentrated in distal localities at distances greater than approximately 1 km from the vent.

*Facies T10: planar-laminated tuff*

Facies T10 comprises tan, well-stratified, well-sorted ash tuff beds with alternating thin continuous interbeds and laminae of fine- to coarse-grained ash. Overall facies thickness averages approximately 15 cm, but is as thin as 2 cm in the most distal outcrops. Individual beds are distinctive due to color variations resulting from varying proportions of juvenile ash. Reverse grading occurs in some beds, but beds and laminations are generally structureless. Ash laminae show lateral pinching, and overlie local low-angle truncation surfaces. Ash trains occur in structureless beds devoid of ash laminae. Scattered lapilli and coarse-grained ash produce small-scale impact sags. This facies occurs in the most distal localities of the surge sequences, beginning approximately 1 km from the vent.

## ***VOLCANO DESCRIPTIONS***

### *Triplets*

“Triplets” volcano is located in the southeastern part of the field area (Plate 1) and is a hybrid tuff-ring/scoria-cone maar. “Triplets” is a ‘lily-pad’-shaped butte approximately 520 m by 670 m trending northwest-southeast, approximately 64 m above the surrounding plains, capped and protected from erosion by lava. One vent is identified at this location, having produced lava ponded within the central crater and two break-out flows on opposite sides of the crater that give the butte a unique morphology. The lapilli tuff produced from Triplets maar overlies the adjacent Red Clay Mesa lapilli-tuff unit, permitting a relative correlation for eruption timing within the field area (Plate 1; Fig. 7).

Triplets maar is the source of a laterally contiguous pyroclastic sequence. Outflow deposits are traceable to locations up to 1200 m from the vent. The tuff ring is



defined by inward-dipping tuffs that include a proximal facies identified by highly disorganized and bomb- and block-rich matrix-supported tuff breccia. A sequence of matrix-supported lapilli-tuff to tuffs grade into the tuff-ring deposits and are capped by subsequent lava flows, rootless flows, and spatter layers. These late breakout lava flows preserved the underlying pyroclastic units, making this site optimal for a study of the AMS characteristics of phreatomagmatic surge deposits.

The Triplets maar yielded two distinct eruption pulses: units 1A and 1B (Fig. 7). Unit 1B has a continuous lateral exposure and was the focus of detailed AMS. Unit 1B is composed of proximal, medial and distal pyroclastic rocks. Lateral exposures of facies LT1, a proximal, dark brown, poorly sorted, matrix-supported lithic tuff-breccia extend for ~300 m from the inferred vent margin (crater rim). This unit laterally grades into LT2 through LT5 facies, consisting of light to dark brown, moderately-sorted, stratified to cross-bedded, matrix-supported lapilli tuffs. These extend 300-750 m from the crater rim. At 750-1050 m from the crater rim, the 1B unit grades laterally into a stratified/plane parallel unit, facies T6 (Fig. 7).

The Triplets maar eruptive sequence is interpreted as a “wet,” low energy, monogenetic event. The accumulated stratigraphic thickness of units 1A and 1B, as well as its deposit morphology and change in lateral facies (Fig. 7), indicate a monogenetic eruptive history. The outflow deposits indicate that the eruptive units 1A and 1B have a progressively aggrading contact. The lack of sedimentary features – mud cracks, influx of epiclastic material, slumping, and development of paleosurfaces – would indicate that sedimentation of the primary volcanic deposits occurred in short-lived pulses, likely with a very high aggradation rate during active periods (Giordano, 2002).

### TRIPLETS STRATIGRAPHY

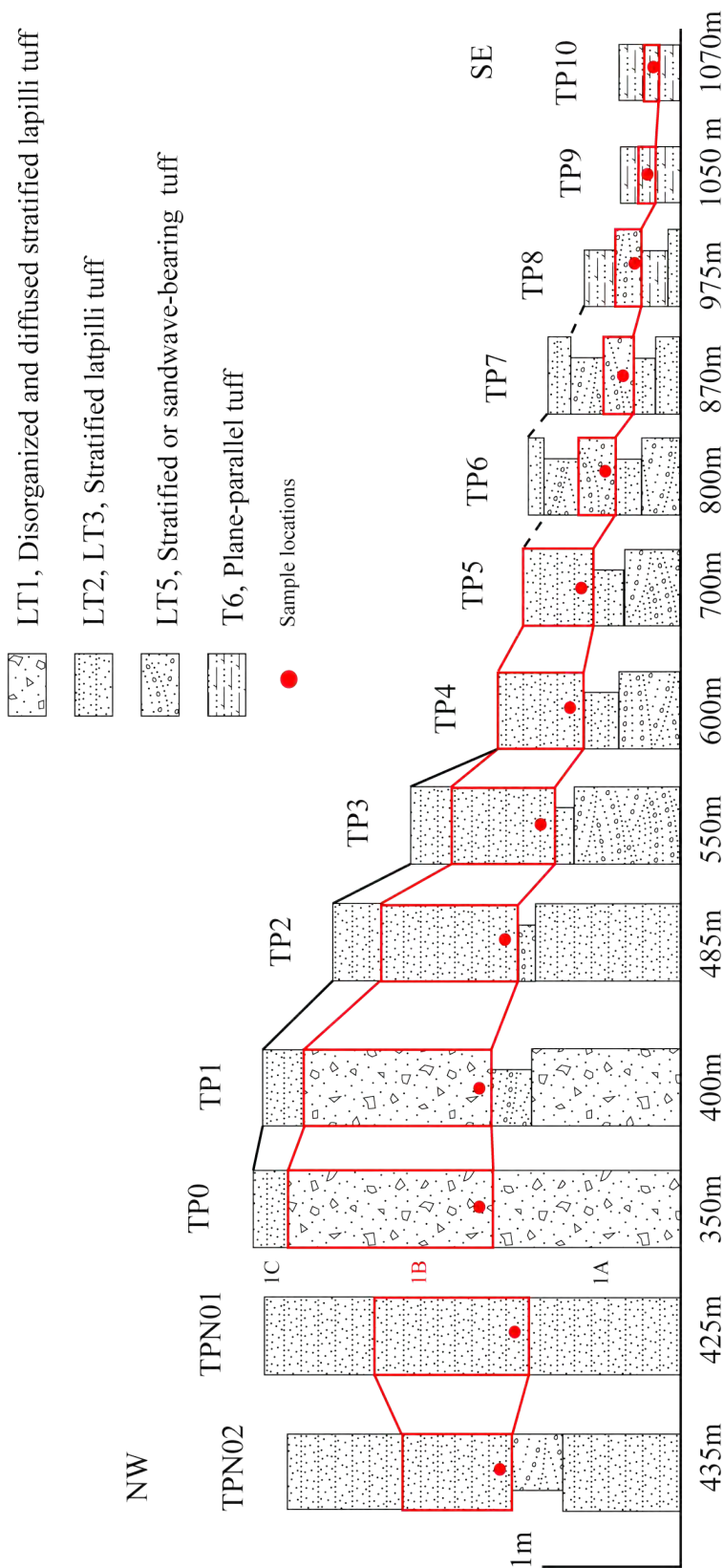


Figure 7: Stratigraphic sections of the Triplets phreatomagmatic deposits. Eruption units are correlated. AMS samples were taken from the basal section of the 1B unit.

### *Haskie Maar*

Haskie maar provides excellent exposure for the detailed study of depositional regimes of phreatomagmatic volcanism. Haskie maar is located on the north-central part of Wood Chop Mesa (Fig. 2, Plate 1). Vazquez (1998) mapped and described Haskie maar in detail. The volcano itself is a hybrid tuff-ring/scoria-cone volcano that is elongated southwest-northeast. The tuff ring is approximately 0.5 km by 0.6 km and is overlain by coalescing scoria cones (Vazquez, 1998). The products of the Haskie maar directly overlie Surprise and Phantom maar deposits, and are cross-cut by Gwen Claim and Churro maars (Vazquez, 1998, 1999).

Haskie maar is the source of the laterally continuous pyroclastic sequence of Wood Chop Mesa. Outflow deposits from this source are traceable to locations >1 km from the vent. The tuff ring is defined by inward- and outward-dipping tuffs that include a central vent zone defined by highly disorganized tuff breccias, facies LT1. The tuff-ring deposits grade laterally into a sequence of lapilli tuff to tuffs (facies LT2 and LT3 through T6); both are overlain by scoriaceous lapilli-fall deposits produced during the scoria-cone formation (Vazquez, 1998).

The scoria cones comprise alternating beds of red, scoriaceous lapilli tuff and ash tuff, agglutinate, and rootless flows. Beds have variable dips, but in general define two coalesced cones, one of which was host to a central lava lake, and another flanking lava flow breached the tuff ring and flowed laterally (Vazquez, 1998). Late-stage strombolian and effusive volcanism filled the depressed vent area of the tuff ring, as indicated by inward-dipping lower beds and outwardly dipping upper beds.

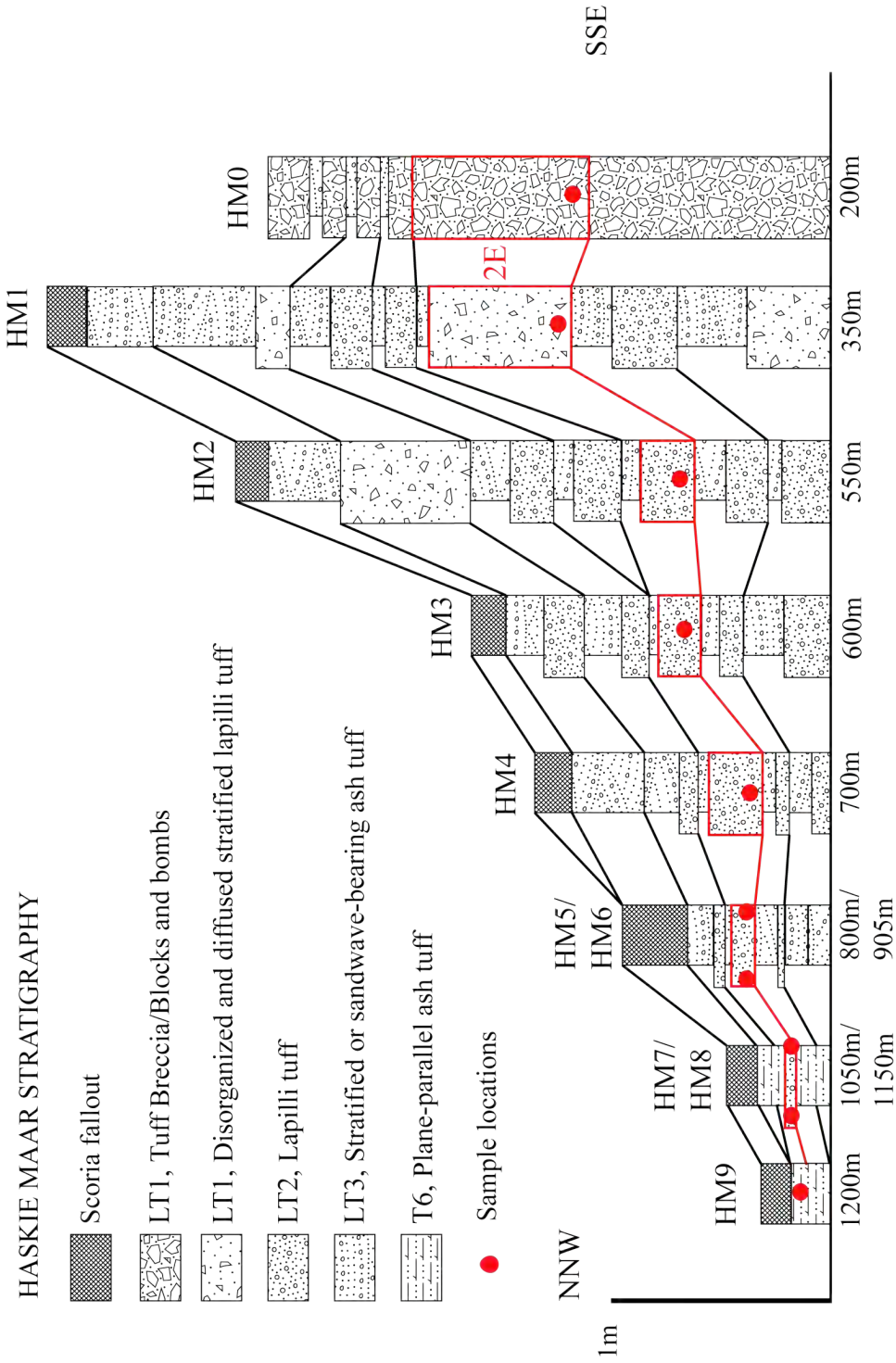


Figure 8: Stratigraphic section of Haskie phreatomagmatic deposits. Eruption units are correlated. AMS samples were taken from the basal section of the 2E unit. Modified from Vazquez and Ort, 2006.

### *Deshgish Butte*

Deshgish Butte is located in the northern part of the study area and is associated with multiple eruptive events (Fig. 2; Plate 1). Deshgish Butte is a roughly pear-shaped mesa, elongated in a north-south direction, with scalloped sides. The butte, approximately 90 m above the surrounding plains, is capped and protected from erosion by lava flows from 5 identified vents. Each eruptive event resulted in lava ponding within the crater and potentially included outflow and spattering.

Multiple events are characterized by an early maar-forming eruptive sequence called the Cottonwood maar and a later nested vent complex comprising the Point, Shazam, and Jack Rabbit maars (Plate 1). Cottonwood maar deposits form a broad, shallowly dipping, oval tuff ring approximately 700 m in diameter, with the Point, Shazam, and Jack Rabbit maar complex located along the southeastern margin of Deshgish Butte, corresponding in the field to a broad undifferentiated package of phreatomagmatic units (Unit 2). The majority of Deshgish deposits are thin- to medium-bedded coarse-ash to medium-ash and lapilli tuffs of facies LT2 and LT3, with grain size varying with distance from the estimated eruption center.

Cottonwood maar produced one major eruptive event identified as Unit 1A (Fig. 9). This unit appears between 300 to 2300 m laterally from the inferred vent site; the majority of the outcrops are located between 300 to 1200 m from the vent. Vent-proximal deposits for Cottonwood maar are not exposed. Medial through distal deposits lie conformably on top of the Tertiary lower Bidahochi Fm. and have been preserved in-situ by an erosion-resistant lava cap. Medial deposits (distances of 450-700 m from vent) range from 5 to 10 m thick, whereas the distal traceable extents of the Deshgish Butte maar deposits (distances of 1000-2300 m from vent) are typically only up to 1 to 2 m thick (Fig. 2, Fig 9). The proximal deposits dip toward the center of the crater between 5° and 20°. Dips decrease up-section, giving way to sub-horizontal, very thinly bedded, finely laminated, reworked tuffaceous siltstones and sandstones interpreted as lake sediments.

The Cottonwood maar is interpreted as a highly explosive 'dry' eruption spatially adjacent to the Point, Shazam, and Jack Rabbit maar complex; however, the deposits of the Cottonwood Maar show deposition and reworking prior to the deposition of the Point,

### DESHGISH STRATIGRAPHY

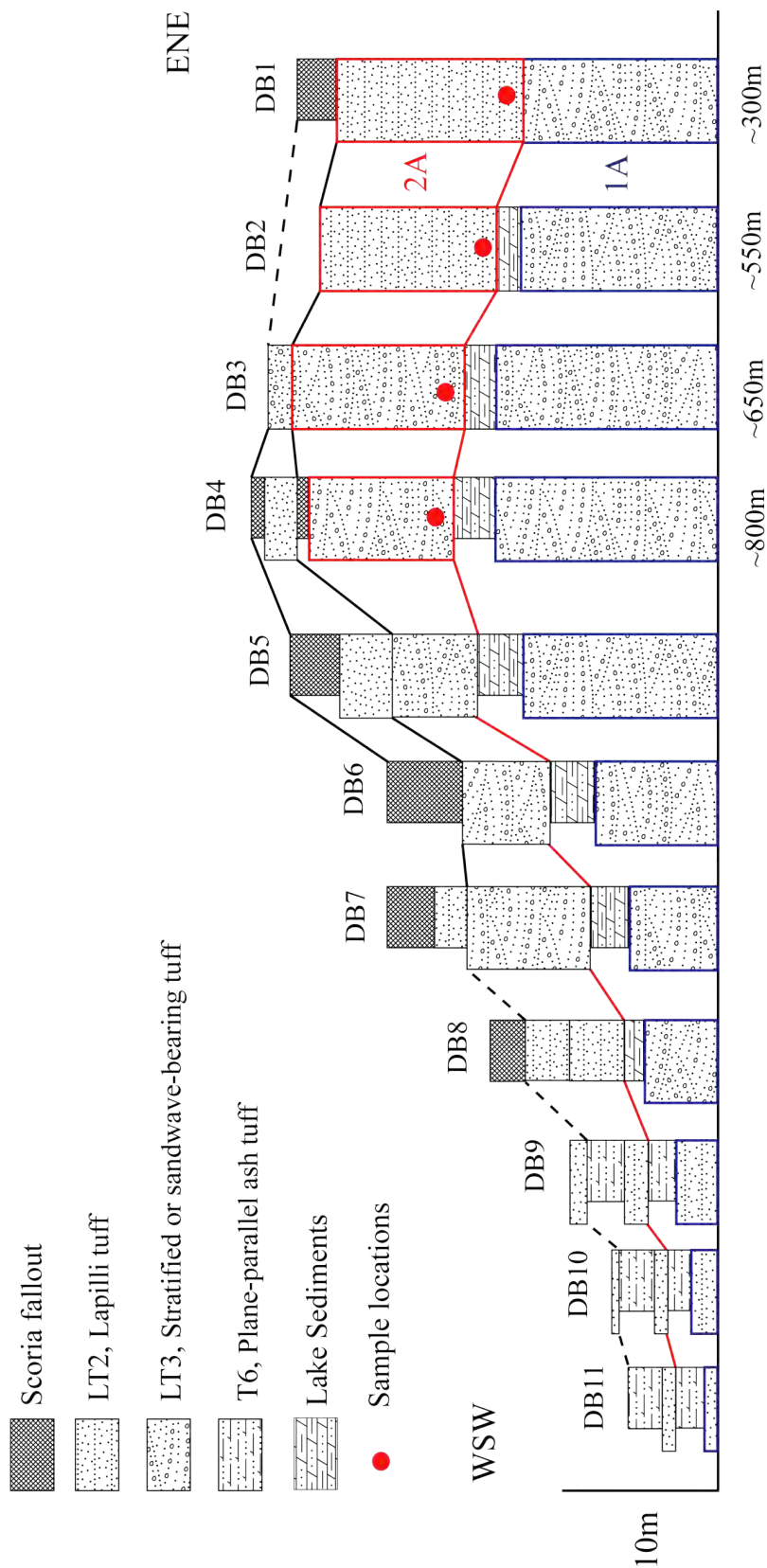


Figure 9: Stratigraphic sections of Deshigish Butte phreatomagmatic deposits. Eruption units are correlated. AMS samples were collected from the basal section of unit 2A.

Shazam, and Jack Rabbit deposits. The laterally extensive deposits of the Cottonwood Maar suggest a high level of fragmentation – clast-supported, thin to medium-bedded sets, with interbedded, cross-bedded sets, of coarse- to medium-ash, sub-rounded to sub-angular lapilli tuff. The lack of interstitial muds, bomb sags, and visible soft sediment deformation is characteristic of a fines depleted clast supported lapilli tuff (dry) eruptive sequence. Taken together, the lateral distribution, grain size, and angularity of the material indicate a highly fragmented dry eruption with deposits up to 2300 m from the eruptive source. The majority of deposits are interpreted as medial to distal outcrops at an estimated distance of 500-800 m from the inferred eruptive center (Plate 1).

The Point, Shazam, and Jack Rabbit maar complex (Unit 2A) lies stratigraphically above Cottonwood maar Unit 1A, and extends over an equal distance (Fig. 9). Proximal lithic tuff breccias in this complex occur within 200 m of the nested vent complex. At distances of 200 to 600 m from the vent, unit 2A grades laterally into a medial facies composed of light brown, clast-supported, moderately sorted, diffusely stratified to cross-bedded, fine- to medium-lapilli tuff. Individual eruptive units are not distinguished due to the complexities of contemporaneous, episodic eruptive sequences produced from the maar complex.

The Point, Shazam, and Jack Rabbit maar complex erupted from a sequence of three nested craters, corresponding in the field to the thick package of undifferentiated phreatomagmatic material mapped as unit 2A. The collective eruptive events are interpreted as a ‘moist’ sequence due to the facies characteristics of the matrix-supported lapilli tuff. The presence of matrix mud is an indicator of liquefied material incorporated at the time of the eruptive event. These muds are distinct clay- to fine-silt-sized particles incorporating the interstitial space between lapilli clasts. Proximal facies are observed to distances up to ~250 m from the eruptive vents and are primarily composed of light brown, matrix-supported, poorly-sorted, massively-bedded, lithic tuff breccia. Given the proximity and style of eruptive processes (i.e. the phreatomagmatic material produced by the Point, Shazam, and Jack Rabbit nested maar complex), the deposits produced by the nested complex at Deshgin Butte have a complexity and polygenetic nature, so that only the vent-proximal facies can be confidently attributed to a single eruptive source.

## CHAPTER 4: RESULTS OF MAGNETIC REMANENT ANALYSES

---

### *REMANENT MAGNETISM RESULTS*

Paleomagnetic analysis was conducted to determine the characteristic remnant magnetism (ChRM) of samples from twelve sites at Haskie maar (HM), East Haskie maar (HME), and Triplets (TP) study areas. The remanence sample sites coincide with AMS locations and are labeled with the same prefixes (Appendix 1). As an artifact of their polygenetic origin, the ChRM samples from Deshghish butte were presumed to be inconclusive; Deshghish was only sampled for AMS analysis.

ChRM results indicate that, most values cluster within  $\alpha 95$  intervals throughout the study area. Auto-reversals –  $180^\circ$  differences in clustering – were not observed within this sample set. However, these can be common features and should be recognized. This phenomenon might be attributed to lightning strikes, or other magnetic anomalies, such as baking, contact metamorphism or hydrothermal alteration, that can essentially ‘reset’ the local geo-magnetic field. The overall data trend suggests that the magnetic character of each study site has remained stable and samples have not been rotated, affected by lightning strikes, hydrothermally altered or affected by other diagenetic processes.

#### *Triplets ChRM Results*

Six sites were sampled for paleomagnetic analysis at the Triplets location: TP2, 3, 6, 7, 8, and 9 (Fig. 10). Samples TP2, TP6, and TP7 display strong clustering, indicative of a stable paleomagnetic history. TP3 does not cluster, suggesting it has not experienced a stable magnetic history. The ChRM values indicate that unit 1B at the TP test site has not been magnetically altered and/or rotated through time.



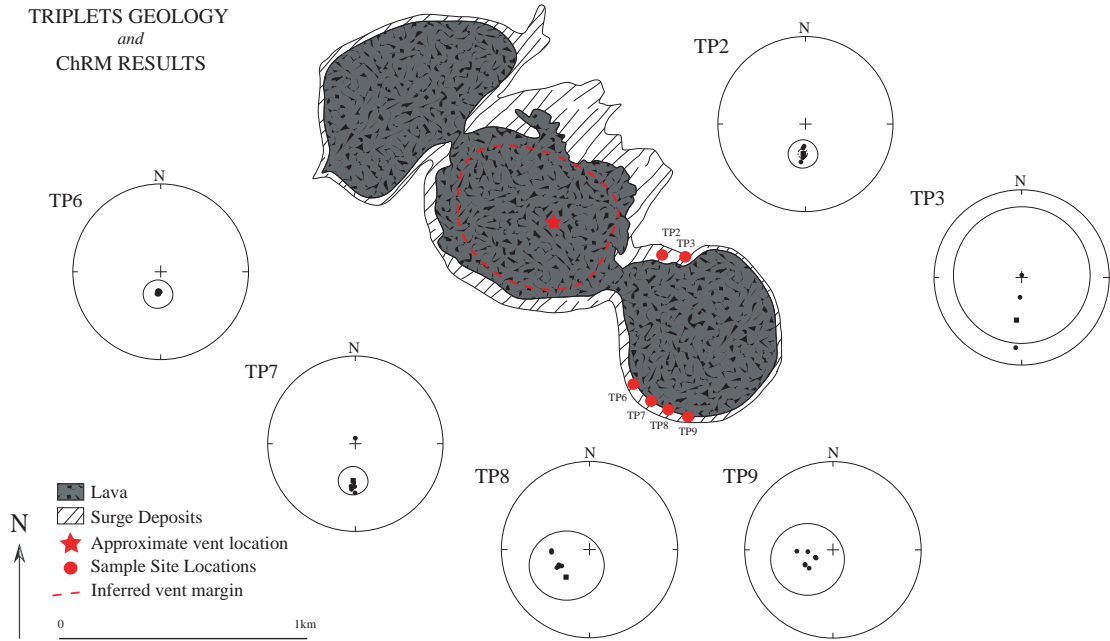


Figure 10: Triplets maar and associated volcanic deposits with ChRM results. Lava deposits include lava flows and pyroclastic material, comprising both a tuff ring and agglutinate margin. Surge deposits include phreatomagmatic products of surge and ash fall. Sample sites show distribution of the ChRM results with circles showing the  $\alpha 95$  ellipse.

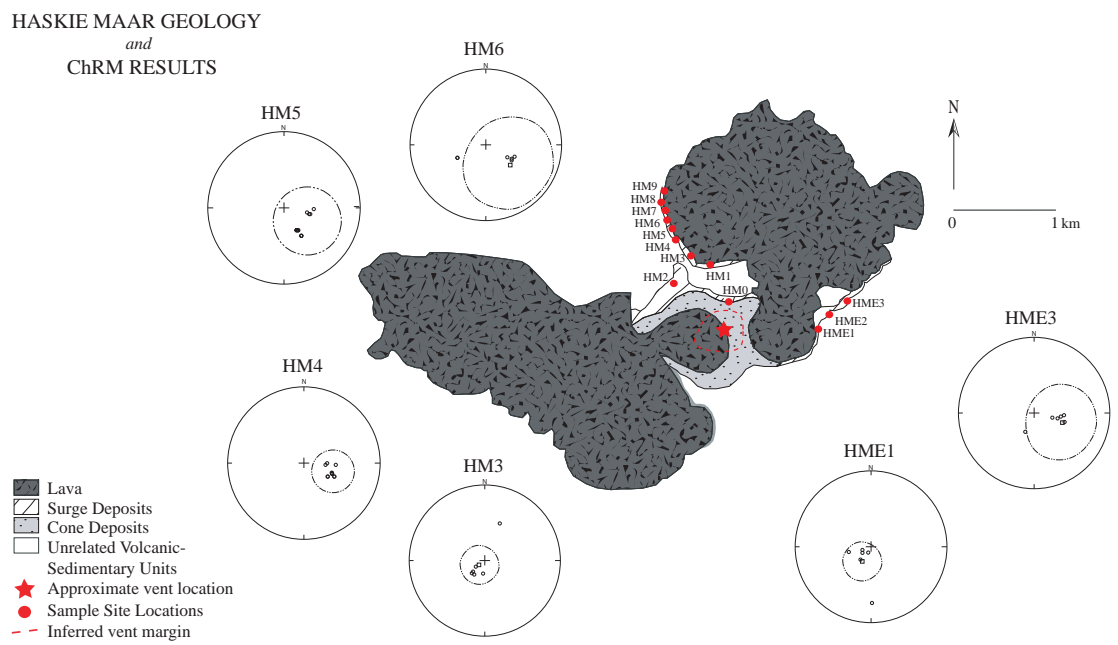


Figure 11: Haskie maar and associated volcanic deposits with ChRM results. Cone deposits comprise tuff ring and scoria cones. Surge deposits are phreatomagmatic surge and ash fall products. Sample sites show distribution of the ChRM results with circles showing the  $\alpha 95$  ellipse. Figure modified from Vazquez and Ort (2006).

### *Haskie Maar ChRM Results*

The six remanence sites at Haskie maar (Fig. 11) are located on both the western cliff exposures (samples HM3-HM6) and the eastern cliffs (samples HME1 and HME3). HM3-HM6 show strong clustering within the dataset. HME sites both have good clustering. The ChRM data indicate that unit 2E at the HM test site has not been magnetically altered and/or rotated through time.

### **AMS RESULTS**

Anisotropy of Magnetic Susceptibility (AMS) analysis was conducted on samples collected from 30 sites within the study area. AMS samples were analyzed from 10 sites at the Haskie maar (HM), 3 sites at Haskie maar east (HME), 11 sites at Triplets maar (TP), 2 sites at Triplets North (TPN), and 4 sites at Deshgish Butte (DB). In each of the main study areas, the general AMS results show a characteristic proximal, medial, and distal signature. AMS trends have an increasing organization with lateral distance from the eruptive vent through the medial sections of the dataset; this trend generally becomes less lineated, but still well foliated in the distal reaches.

### *Triplets AMS Results*

Sites TP0-TP10, TPN1 and TPN2 were all sampled within the 1B eruptive unit at the Triplets location. Unit 1B is ideal for this type of study because it can be traced up to 1070 m from the inferred vent at Triplets maar (Fig. 7). Unit 1B was sampled laterally to observe the evolution of an individual eruptive pulse as transport and deposition influence the magnetic characteristics of the phreatomagmatic surge. The variability within the AMS signatures of unit 1B should provide insight into surge emplacement processes and depositional dynamics.

TP0 and TP1 display disorganized AMS signatures that have been “texturally” quantified as oblate by T values of  $0 < T < 0.350$  and visually qualified as disorganized with D/I values of  $< 2$  (Table 1, 2). The  $K_1$  axis is parallel to flow. Sample TP0 was collected approximately 350 m from the eruptive vent (Fig. 12) and is located within the disorganized to poorly-stratified lapilli tuff facies LT1 (Fig. 7; Table 2). TP1 comes from a sample location approximately 350 m from the eruptive vent and is located within the

disorganized and defused stratified lapilli tuff and tuff breccia facies LT1 (Fig. 7; Table 2).

Although both classified with a disorganized D/I signature, TP0 and TP1 – when viewed together – show a progression toward increasing organization and dataset clustering with distance from vent. This trend suggests increased an organization within both the flow itself and depositional pattern, and may also infer a correlation to the depositional models proposed by Vazquez (2006). This apparent correlation will be further discussed in Chapter 5.

Samples TP2 through TP8 display the lineated D/I signature that qualifies the hemispheric data for these site locations, and have been texturally quantified as having an oblate fabric ( $0 > T > 1$ ) by T values of  $0.350 < T < 0.700$  (Table 1, 2). Sample TP2 comes from a relatively vent-proximal location, at approximately 400 m from the eruptive vent, and is situated within the stratified or sand-wave-bearing ash-tuff facies LT2. The  $K_1$  axis of sample TP2 begins to show flow-parallel alignment (Fig. 12). The D/I ratio

qualitatively places this sample at the threshold of the disorganized to lineated transition, visible in its hemispheric data plot (Fig 13). TP3 comes from a sample location approximately 450 m from the eruptive vent, and is also located within the LT2 facies.

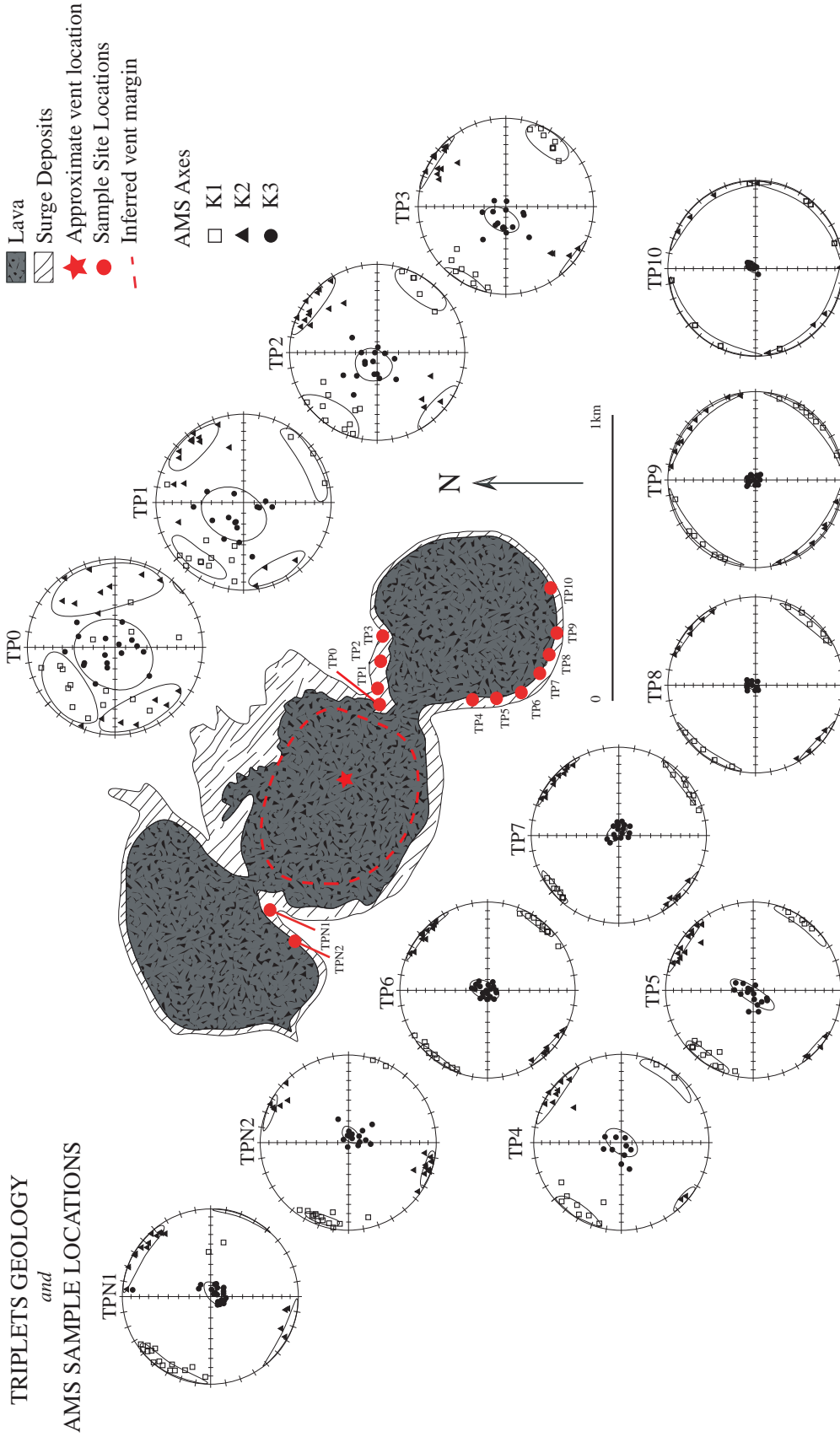


Figure 12: Triplets maar and associated volcanic deposits with AMS plots. Sample localities for facies analysis are shown and identified by stratigraphic section designation. The center of the inferred vent zone for the phreatomagmatic deposits is denoted with a star. AMS hemispherical plots are systematically placed to display the transition of AMS characteristics from chaotic to lineated to girdled.

Table 1: Anisotropy of magnetic susceptibility (AMS) data from Hopi Buttes phreatomagmatic deposits. All sample locations collected in mtrs, UTM zone 11N, 1927 North American datum. N, number of samples collected at each site, one to three specimens per sample; Km, bulk susceptibility (in 10<sup>-3</sup> SI); K1, K3; L, magnetic lineation (K1/K2); F, magnetic foliation ((K2/K3), P, anisotropy degree (K1/K3); T, shape parameter [-1 < T < 0 = prolate, 0 < T < 1 = oblate (Jelinek, 1981)]; DEC, average declination value at site; INC, average inclination value at site; DEC ca, average declination confidence angle ( $\alpha$  95); INC ca, average inclination confidence angle ( $\alpha$  95); D/I, DEC ca/ INC ca ratio.

Anisotropy of Magnetic Susceptibility Data																												
Site	Northing	Easting	Facies	Distance from vent	N	Km	K <sub>1</sub>	K <sub>2</sub>	K <sub>3</sub>	L	F	P	T	K <sub>1</sub>			K <sub>2</sub>			K <sub>3</sub>								
														DEC	INC	DEC ca	D/I	DEC	INC	DEC ca	D/I	DEC	INC	DEC ca	D/I			
DB1	3929578	585735	LT1	300	12	2.46E-02	1.002	1.000	0.998	1.002	1.002	1.004	-0.231	288.40	19.70	22.30	14.80	1.51	180.50	40.60	38.90	24.60	1.58	37.70	42.90	46.50	44.20	1.05
DB2	3929830	585440	LT2	550	16	1.98E-02	1.003	1.001	0.996	1.002	1.006	1.007	0.568	62.00	0.30	12.30	3.20	3.84	152.00	0.50	15.00	6.10	2.46	302.10	89.40	10.20	12.50	0.82
DB3	3929085	585200	LT1	650	12	3.13E-02	1.001	1.000	0.999	1.001	1.001	1.002	0.257	262.20	5.10	25.10	12.70	2.06	354.90	28.80	42.30	29.90	1.41	162.90	60.60	25.60	25.30	1.01
DB4	3929398	584980	LT1	800	13	2.17E-02	1.002	1.000	0.998	1.003	1.002	1.005	0.096	180.20	17.30	14.80	9.90	1.49	87.10	9.80	15.10	14.90	1.01	328.80	70.00	19.90	19.60	1.02
TP0	3926667	589344	LT2	300	18	2.31E-02	1.002	1.001	0.999	1.015	1.008	1.023	0.242	322.30	28.70	33.60	22.20	1.51	232.70	18.50	44.80	20.80	2.15	200.20	89.20	31.40	40.30	0.78
TP1	3926679	589431	LT2	350	13	1.98E-02	1.001	1.000	0.998	1.009	1.018	1.028	0.309	305.20	18.70	23.80	13.20	1.80	35.80	12.20	20.30	11.50	1.77	300.20	78.30	32.40	30.20	1.07
TP2	3926693	589487	LT2	400	12	2.47E-02	1.003	1.001	0.997	1.012	1.030	1.043	0.418	302.20	9.80	22.50	14.80	1.52	32.20	4.50	24.70	10.20	2.42	302.30	89.20	20.20	15.40	1.31
TP3	3926677	589551	LT2	450	12	2.75E-02	1.002	1.001	0.998	1.003	1.005	1.008	0.415	297.60	11.10	13.80	5.80	2.38	27.60	5.80	19.80	4.60	4.30	293.20	79.20	14.80	9.80	1.51
TP4	3926552	589352	LT2	550	10	2.64E-02	1.003	1.001	0.997	1.002	1.002	1.004	-0.214	300.20	3.20	17.50	5.70	3.07	30.30	9.10	18.90	4.30	4.40	120.20	89.70	13.80	10.10	1.37
TP5	3926248	589358	LT2	700	16	1.36E-02	1.002	1.000	0.998	1.003	1.013	1.016	0.590	306.30	7.90	14.30	6.20	2.31	37.40	4.40	20.00	4.60	4.35	126.20	89.90	19.70	10.20	1.93
TP6	3926130	589416	LT3	850	19	1.63E-02	1.004	1.001	0.996	1.001	1.002	1.003	0.510	309.90	2.10	15.00	3.70	4.05	41.10	3.20	20.30	2.80	7.25	130.30	90.00	15.70	10.30	1.52
TP7	3926041	589534	LT3	900	16	2.31E-02	1.004	1.002	0.992	1.002	1.011	1.013	0.472	320.10	4.20	15.70	6.20	2.53	50.20	1.20	21.10	3.10	6.81	140.10	89.40	10.30	15.30	0.67
TP8	3926032	589667	LT3	950	10	1.18E-02	1.002	1.001	0.996	1.004	1.013	1.017	0.584	308.90	6.80	22.30	3.40	6.56	38.20	2.30	19.90	2.30	8.65	320.30	87.60	3.10	2.10	1.48
TP9	3926072	589785	T6	1050	15	2.23E-02	1.004	1.002	0.997	1.002	1.014	1.016	0.771	132.30	4.50	34.90	4.10	8.51	220.80	3.90	35.10	4.00	8.78	350.30	88.20	2.70	2.50	1.08
TP10	3926172	589892	T6	1075	8	2.10E-02	1.004	1.003	0.994	1.001	1.012	1.013	0.788	128.40	2.40	39.40	4.80	8.21	218.20	3.90	49.20	4.90	8.61	5.20	85.80	3.20	3.40	0.94
TPN1	3927103	588845	LT2	470	12	2.52E-02	1.003	1.001	0.993	1.011	1.021	1.035	0.427	314.20	7.50	22.30	6.10	3.66	44.20	6.80	20.70	5.90	3.51	120.60	79.80	12.30	9.90	1.24
TPN2	3926975	588418	LT2	570	15	2.44E-02	1.002	1.001	0.993	1.009	1.018	1.028	0.409	290.10	10.20	12.20	5.30	2.30	200.20	6.90	10.20	5.60	1.82	110.10	80.20	13.20	10.10	1.31
HMD	3923890	589930	LT2	200	11	2.78E-02	1.001	1.000	0.998	1.001	1.000	1.001	0.207	162.30	13.20	32.40	15.50	2.09	252.30	15.20	35.40	21.10	1.68	330.30	65.80	18.90	10.20	1.85
HMI	3924184	589800	LT2	350	17	2.98E-02	1.004	1.000	0.997	1.002	1.001	1.003	-0.215	160.20	33.10	31.20	21.20	1.47	250.20	23.20	35.10	17.80	1.97	5.20	61.10	12.60	6.60	1.91
HM2	3924093	589510	LT2	550	9	2.29E-02	1.003	1.001	0.998	1.007	1.023	1.03	0.542	169.80	9.90	15.50	6.20	2.50	259.80	5.50	11.80	6.70	1.76	340.10	89.70	10.10	5.20	1.94
HMB	3924241	589653	LT2	600	7	2.70E-02	1.002	1.001	0.997	1.002	1.004	1.006	0.405	151.20	2.50	27.30	11.70	2.33	241.40	4.00	27.00	7.50	3.60	298.80	85.20	13.70	7.20	1.83
HMA	3924328	589577	LT2	700	18	2.66E-02	1.001	1.000	0.999	1.002	1.001	1.003	-0.066	158.80	2.20	12.90	6.30	2.05	248.80	4.40	12.80	9.20	1.39	350.30	82.30	9.70	5.90	1.64
HME	3924427	589494	LT2	800	15	1.36E-02	1.004	1.002	0.994	1.002	1.008	1.01	0.532	159.70	2.00	17.90	4.60	3.89	249.70	0.70	17.90	3.40	5.26	0.00	87.90	5.10	3.10	1.65
HM5	3924537	589465	LT2	905	7	1.71E-02	1.002	1.001	0.997	1.001	1.004	1.006	0.514	178.90	3.60	7.50	1.70	4.41	269.30	6.40	7.50	3.20	2.34	59.60	82.60	3.40	1.90	1.79
HM7	3924656	589398	LT2	1050	14	2.08E-02	1.002	1.001	0.997	1.001	1.004	1.005	0.376	161.80	17.00	13.10	5.30	2.47	254.30	8.00	13.30	5.10	2.61	8.40	71.10	6.10	4.70	1.30
HMB	3924808	589423	LT3	1150	15	1.17E-02	1.004	1.002	0.994	1.003	1.008	1.011	0.507	171.90	9.10	10.40	3.60	2.89	268.20	1.70	10.50	4.00	2.63	2.90	80.70	4.90	3.20	1.88
HMB	3924825	589424	T6	1200	18	1.40E-02	1.004	1.003	0.993	1.001	1.011	1.012	0.716	118.70	0.50	39.50	4.50	8.78	282.70	0.60	39.50	7.10	5.56	250.30	89.20	8.10	4.30	1.88
HME1	3923683	589071	LT2	800	12	2.67E-02	1.003	1.001	0.996	1.001	1.008	1.009	0.498	249.80	3.30	20.10	5.20	3.87	347.30	2.20	14.80	4.80	3.08	72.30	83.50	4.80	2.50	1.92
HME2	3923757	589100	LT2	900	8	2.14E-02	1.004	1.001	0.995	1.003	1.009	1.012	0.564	288.20	6.70	7.20	2.50	2.88	348.20	6.30	8.10	2.80	2.89	70.30	83.30	5.60	3.10	1.81
HME3	3923879	5891203	LT2	1100	12	1.11E-02	1.002	1.001	0.997	1.002	1.012	1.014	0.660	255.10	5.20	14.90	3.20	4.66	345.10	5.30	12.20	3.80	3.21	75.30	85.50	4.50	3.30	1.36

Table 2: Triplets AMS textural discrimination table. AMS quantitative and qualitative textural features: L, magnetic lineation (K1/K2); F, magnetic foliation (K2/K3), P, anisotropy degree (K1/K3); T, shape parameter:  $-1 < T < 0 =$  prolate,  $0 < T < 1 =$  oblate (Jelinek, 1981), shown with associated AMS hemispherical plots.

Site	TP0	TP1	TP2	TP3	TP4	TP5	TP6	TP7	TP8	TP9	TP10	
Distance from vent	350	400	485	550	600	700	800	870	975	1050	1070	
Lateral Facies	L1	L1	L2	L2	L2	L3	L3	L5	L5	T6	T6	
L	1.015	1.009	1.012	1.003	1.002	1.003	1.001	1.002	1.004	1.002	1.001	
F	1.008	1.018	1.03	1.005	1.002	1.013	1.002	1.011	1.013	1.014	1.012	
T	0.242	0.309	0.418	0.415	-0.214	0.590	0.510	0.472	0.584	0.771	0.788	
AMS Facies	<b>Disorganized</b>						<b>Lineated</b>					
AMS Diagrams												
<b>Triplets North Discrimination</b>												
Site	TPN1	TPN2										
Distance from vent	425	435										
Lateral Facies	L2	L2										
L	1.011	1.009										
F	1.021	1.018										
T	0.427	0.409										
AMS Facies	<b>Disorganized</b>		<b>Lineated</b>									
AMS Diagrams												

TP4 was collected approximately 600 m from the eruptive vent and is also located within the stratified or sand-wave-bearing ash-tuff facies LT2. Similar to TP2, samples TP3 and TP4 show an overall oblate fabric (Table 1, 2) with a lineated D/I signature (Fig. 13), and display a moderately-sorted  $K_1$  axial clustering, a  $K_1$  axis parallel to flow, and  $K_3$  foliation poles that begin to cluster more tightly around  $90^\circ$  (Fig. 12).

TP5 comes from a sample location approximately 700 m from the eruptive vent and is located within the stratified or sand-wave-bearing tuff facies LT3. TP5 shows an overall oblate textural fabric (Table 1, 2) with a lineated  $K_1$  D/I signature (Fig. 12, Table 2). The  $K_1$  axis is parallel to flow direction and the  $K_3$  axis is tapered down and clustered near  $90^\circ$  inclination. TPN1 and TPN2 were collected along the northern cliff exposures within the stratified or sand-wave-bearing tuff facies LT2 at Haskie maar (Fig. 8). Samples TPN1 and TPN2 were collected at approximately 425 m and 435 m, respectively, from the inferred eruptive vent (Table 2, Fig. 7). These samples exhibit lineated AMS signatures consistent with TP4 through TP6, collected at analogous locations on the southern extent of Triplets maar.

Samples TP6 through TP8 were all collected from stratified tuff facies LT5 (Fig. 5). Sample collection distances are approximately 800 m, 870 m, and 975 m from the eruptive vent, respectively. TP6 shows an overall oblate fabric (Table 1, 2) with a lineated AMS distribution (Fig. 12, Table 2). TP7 shows an overall oblate fabric (Table 1, 2) with a lineated AMS distribution (Fig. 12). The  $K_1$  axis is parallel to flow and the  $K_3$  axis pole to the foliation is centered at  $90^\circ$  (Fig. 12). TP8 also shows an overall oblate fabric (Table 1, 3) with a lineated AMS distribution (Fig. 12). The  $K_1$  axis has moved away from parallel to flow and the  $K_1$  and  $K_2$  axis data points are distributed relatively evenly around the circumference of the hemispherical plot in a phenomenon referred to in this manuscript as ‘girdling’, while the  $K_3$  axis is clustered tightly around  $90^\circ$ . D/I ratios categorize these data as girdled, but are at the transition between lineated and girdled axial signatures (Fig. 13).

Samples TP9 and TP10 display a girdled D/I signature that quantifies the visual hemispheric data pattern for these locations, and have been texturally quantified as having an oblate fabric ( $0 > T > 1$ ) by  $T > 0.700$  (Fig. 12; Table 1, 2). Girdled AMS fabrics are characterized by  $K_1$  and  $K_2$  axes that are diffused around the horizontal plane

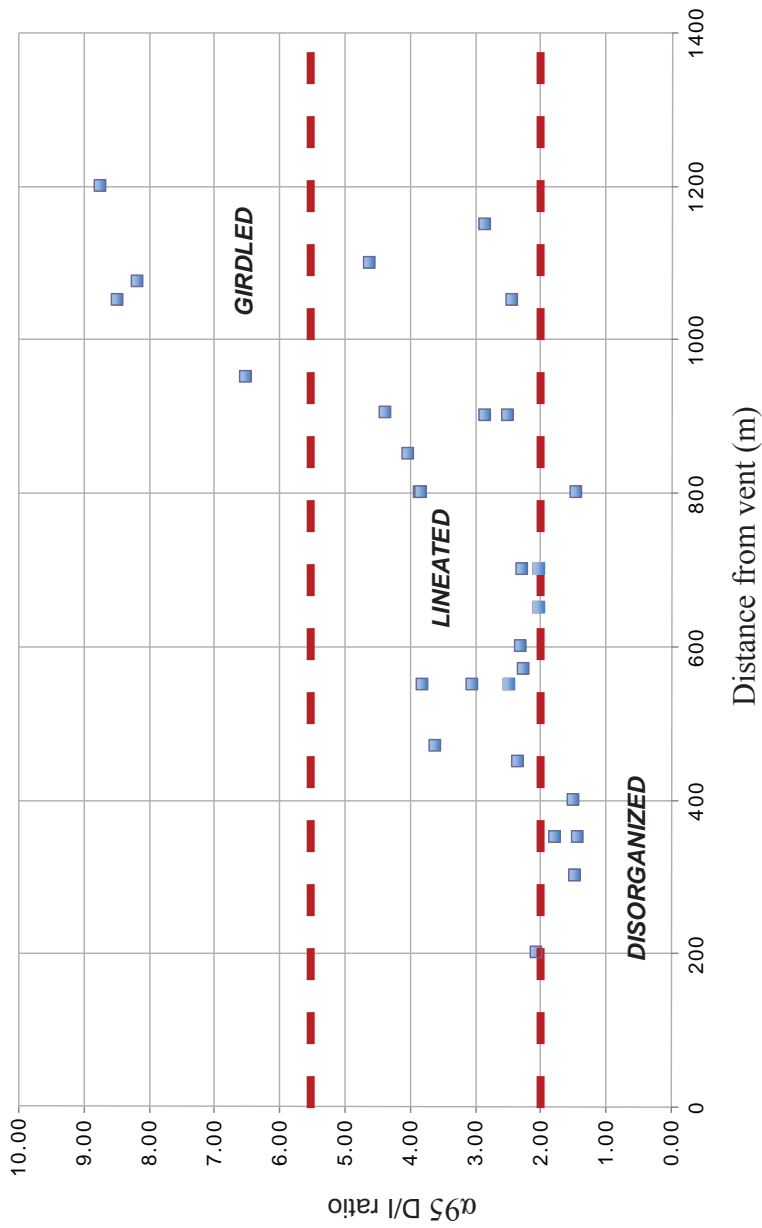


Figure 13: Ratio of  $\alpha95$  error of the declination/ $\alpha95$  error of the inclination for the  $K_1$  axis (D/I) versus distance from eruptive vent. Axis variability ratios are tentatively grouped into general categories reflecting  $K_1$  axis clustering, as reflected on the hemispherical plots of AMS results. D/I ratios:  $0 < D/I < 2.0$  = disorganized,  $2.0 < D/I < 5.50$  = lineated,  $D/I > 5.50$  = girdled.



of the hemispherical plot. TP9 comes from a sample location approximately 1050 m from the eruptive vent and is located within the stratified, undulatory, juvenile-rich tuff facies T6 (Fig. 7). TP10 comes from a sample location approximately 1070 m from the eruptive vent located within the stratified undulatory juvenile-rich tuff facies T6 (Fig. 7).

### *Haskie AMS Results*

Sites HM0-HM9 and HME1-HME3 were all sampled within the 2E eruptive unit correlated by Vazquez (1998) (Fig. 8) at the Haskie location. Unit 2E is ideal for this type of study because it can be traced up to ~1400 m from the inferred vent at Haskie maar (Fig. 8). As with the Triplets location, unit 2E was sampled laterally to observe the evolution of an individual eruptive pulse as transport and deposition influence the magnetic characteristics of the phreatomagmatic surge. The variability within the AMS signatures of unit 2E should provide further insight into surge emplacement process and depositional dynamics.

HM0 and HM1 display disorganized AMS signatures that have been texturally quantified as oblate by T values of  $0 < T < 0.350$  and visually qualified as possessing a disorganized signature – correlated with a quantifiable D/I value  $< 2$  (Fig. 13; Table 1, 3). The  $K_1$  axis is roughly parallel to flow. Sample HM0 was collected approximately 230 m from the eruptive vent (Fig. 14) and is located with the disorganized to poorly-stratified lapilli tuff facies LT1 (Fig. 8). The  $K_3$  poles to foliation display a rough imbrication (Fig. 12). Sample HM1 was collected approximately 525 m from the eruptive vent and is located within the disorganized and diffused stratified lapilli-tuff facies LT1 (Fig. 8). The average relation between the K axes for sample HM1 suggests an oblate fabric, but the  $0 > T > 1$  would assign a prolate texture for this site (Table 1, 3). This apparent disagreement between T and K axis relations is commonly a function of a distribution anisotropy (Muxworthy and Williams, 2004).

Samples HM2 through HM8, and HME1 through HME3 display lineated AMS signatures that have been quantified by T values of  $0.350 < T < 0.700$  (Table 3) and visually qualified with a lineated AMS signatures (quantifiable D/I value  $2 < D/I < 5.5$ ) (Fig. 13, Table 1, 3). The  $K_1$  axis – parallel to flow – and the  $K_3$  pole to foliation both

HASKIE MAAR GEOLOGY  
*and*  
 AMS SAMPLE LOCATIONS

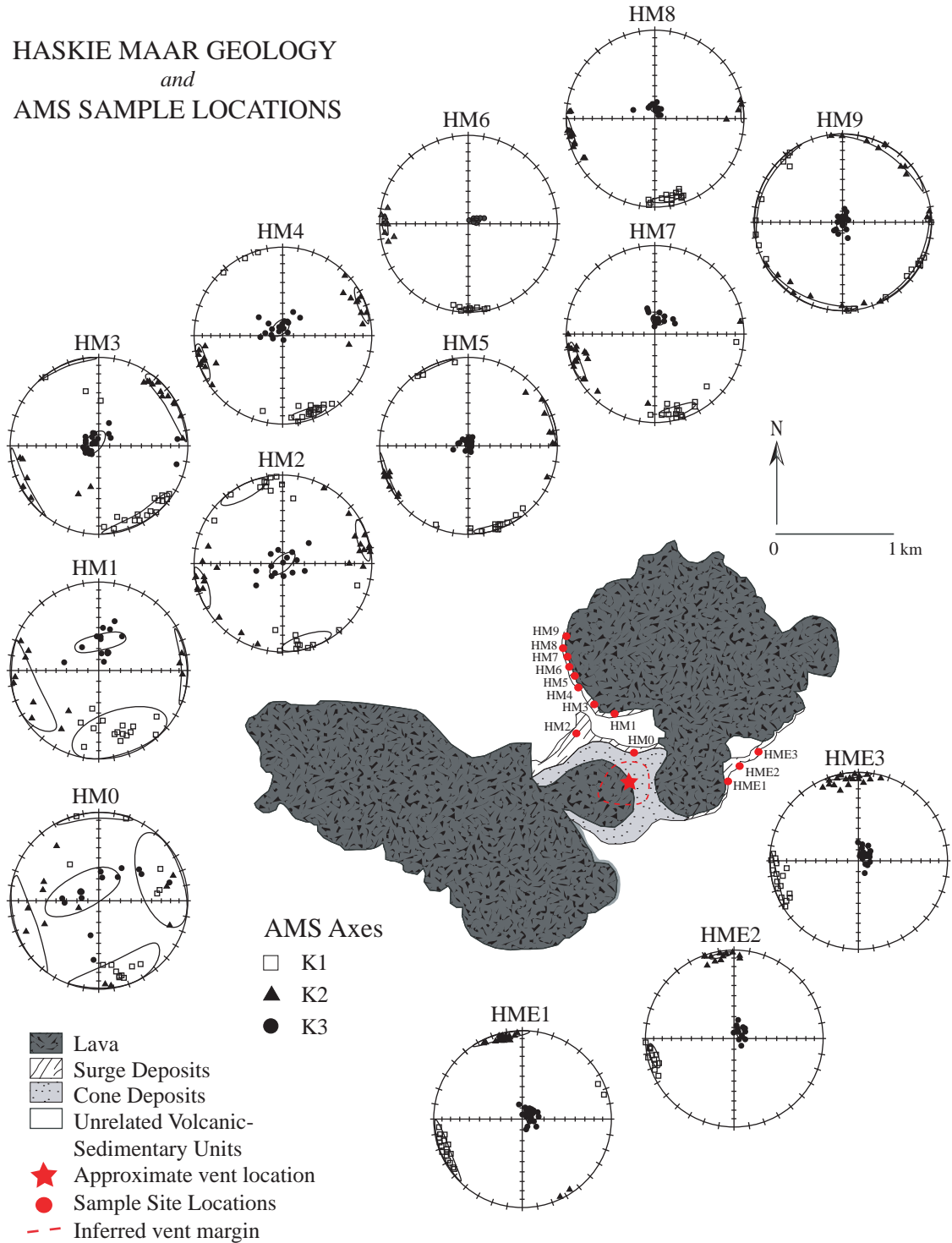


Figure 14: Haskie Maar and associated volcanic deposits. Sample locations for facies analysis are shown with red dots and labelled according to stratigraphic section designation. The center of the inferred vent zone for the phreatomagmatic deposits is denoted by a red star. AMS hemispherical plots are systematically placed to display the transition of K1 AMS axis ratio from chaotic to lineated to girdled at the HM sites.

exhibit strong clustering around  $90^\circ$  for this set of samples. Samples HM2 and HM3 were collected approximately 550 m and 600 m, respectively, from the eruptive vent and are located within stratified or sand-wave-bearing ash-tuff facies LT2 (Fig. 8). HM4 comes from a sample location approximately 890 m from the eruptive vent and was also extracted from the stratified or sand-wave-bearing tuff facies LT2 (Fig. 8). HM4 AMS axes lengths indicate an oblate fabric (Table 1), but the T values indicate a prolate fabric (Table 1, 3), likely a function of a distribution anisotropy overprint (Muxworthy et al, 2004). Samples HM5 and HM6 were extracted approximately 800 m and 905 m, respectively, from the eruptive vent and are located within the stratified or sand-wave-bearing tuff facies LT2 (Fig. 8). These samples display a  $K_1$  axis slightly oblique to flow (Fig. 14). Sample HM7 was collected approximately 1050 m from the eruptive vent, and is also located within stratified tuff facies LT2 (Fig. 8).  $K_1$  axis is oriented roughly parallel to flow (Table 3; Fig. 9); the  $K_3$  axis displays a slight imbrication (Fig. 14). Sample HM8 was collected at a distance of approximately 1150 m from the eruptive vent and is located within stratified tuff facies LT3 (Fig. 8). The HM8  $K_3$  axis displays a slight imbrication (Fig. 14). HME1 through HME3 were collected along the eastern cliff exposures within the stratified or sand-wave-bearing tuff facies LT2 at Haskie maar (Fig. 8). Samples HME1, HME2, and HME3 were collected at approximately 800 m, 900 m, and 1000 m from the inferred eruptive vent (Table 3, Fig. 14). These samples exhibit lineated AMS signatures consistent with HM5 through HM7, collected at analogous locations on the western flank of Haskie maar.

Sample HM9 was collected approximately 1200 m from the eruptive vent and is located within the T6 stratified tuff facies (Fig. 8). HM9 displays a girdled AMS signature that has been quantified by T values  $0.700 < T < 1$  (Table 3) and visually qualified by the broad  $K_1$  and  $K_2$  axial distribution at the equator of the hemispheric AMS plots (Fig. 14). This pattern best matches the qualitative and quantitative signature of distal sites TP9 and TP10 from the Triplets locality. The  $K_3$  axis is clustered around  $90^\circ$  (Fig. 14).

Table 3: Haskie Maar AMS textural discrimination table. AMS quantitative and qualitative textural features: L, magnetic lineation (K1/K2); F, magnetic foliation (K2/K3), P, anisotropy degree (K1/K3); T, shape parameter  $-1 < T < 0 =$  prolate,  $0 < T < 1 =$  oblate (Jelinek, 1981), shown with corresponding AMS hemispherical plots.

Site	HM0	HM1	HM2	HM3	HM4	HM5	HM6	HM7	HM8	HM9
Distance from vent	200	350	550	600	700	800	900	1050	1150	1200
Lateral Facies	LT1	LT1	LT1	LT2	LT2	LT2	LT2	LT2	LT3	T6
L	1.001	1.002	1.007	1.002	1.002	1.002	1.001	1.001	1.003	1.001
F	1.000	1.001	1.023	1.004	1.001	1.008	1.004	1.004	1.008	1.011
T	0.207	-0.215	0.542	0.405	-0.066	0.532	0.514	0.376	0.507	0.716
AMS Facies	<b>Disorganized</b>									
AMS Diagrams										
AMS Facies	<b>Lineated</b>									
AMS Diagrams										
AMS Facies	<b>Girdled</b>									
AMS Diagrams										
AMS Facies	<b>Disorganized</b>									
AMS Diagrams										
AMS Facies	<b>Girdled</b>									

Haskie Maar East Discrimination										
Site	HME1	HME2	HME3							
Distance from vent	800	900	1100							
Lateral Facies	LT2	LT2	LT2							
L	1.001	1.003	1.002							
F	1.008	1.009	1.012							
T	0.498	0.564	0.660							
AMS Facies	<b>Lineated</b>									
AMS Diagrams										
AMS Facies	<b>Girdled</b>									

### *Deshgish AMS Results*

Ten sites were originally sampled at Deshgish Butte, but the more distal sites could not be confidently sourced to any single eruptive vent. Only four could be definitively linked to an individual eruptive “unit”. These four sites, DB1-DB4 were all sampled within Unit 2A (Fig. 9). Deshgish Butte displays features of a nested vent complex (i.e. Point, Shazam, and Jack Rabbit vents or PSJ) associated with late maar development. This nested vent complex produced the unit 2A of the PSJ.

Site DB1 is located at an azimuth direction of  $085^{\circ}$ , approximately 290 to 320 m from the estimated complex center in unit 2A (Fig. 9). The DB1 site has an AMS oblate fabric (Table 1, 4) and the AMS axes display a disorganized distribution. The  $K_1$  axis has errors that give the sample a disorganized D/I ratio signature (Fig 13), which is characteristic of proximal facies.  $K_1$  axis is roughly perpendicular to flow and the  $K_3$  axis displays a moderate imbrication.

Site DB2 is located at an azimuth direction of  $185^{\circ}$  approximately 500 to 600 m from the estimated complex center in unit 2A. The AMS of the DB2 site reveals an overall oblate fabric (Table 1, 4). The clustering of the K axes is well defined and displays a moderately organized distribution of poles of the  $K_1$ ,  $K_2$ , and  $K_3$  axes (Fig. 15). The  $K_1$  axis has a D/I ratio that yields the lineated signature in the hemispheric data distribution (Fig. 15), which is characteristic of medial facies. The  $K_1$  axis is perpendicular to flow and the  $K_3$  axis does not display any degree of imbrication. The inconsistencies of the sorting and confidence angles observed in the AMS plots of the adjacent sample sites suggest that different units may have been sampled. Lateral variation of this unit seems unlikely due to the relative proximity of sites to the nested vent sequence and mapped eruptive vents.

Site DB3 is located at an azimuth direction of  $193^{\circ}$  approximately 600 to 700 m from the estimated complex center in unit 2A. The AMS signature of the DB3 site shows an overall oblate fabric (Table 1, 4) with a visually disorganized AMS distribution (Fig. 15). The  $K_1$  axis is roughly perpendicular/oblique to flow direction and the D/I ratio quantifies the disorganized pattern to the hemispheric data plot. The  $K_3$  axis has moderate imbrication.

Site DB4 is located at an azimuth direction of 200°, approximately 750 to 850 m from the estimated complex center in unit 2A. The AMS signature of the DB4 site shows an overall oblate fabric (Table 1, 4) with a disorganized AMS distribution. The  $K_1$  axis is oriented oblique to roughly parallel to flow, with a disorganized D/I signature. The disorganized D/I signature is unexpected for a medial location, but the axes show initial signs of clustering and particles are beginning to display oriented patterns (Fig. 15). The  $K_3$  axis does not indicate imbrication.

Overall, unit 2A exhibits highly variable AMS signatures and lacks the strong trend toward increasing AMS organization expected for an individual depositional unit produced by a single eruptive event;  $K_1$ ,  $K_2$ , and  $K_3$  axes are generally loosely grouped at Deshghish Butte. Due to the complex interaction of the nested vents, sampling an isolated single eruptive unit was difficult, if not impossible. However, even with the inability to characterize an individual unit, the AMS does show spatial complexities and a general trend with respect to distance from the eruptive vent or vent complex.

## DESHGISH GEOLOGY and AMS SAMPLE LOCATIONS

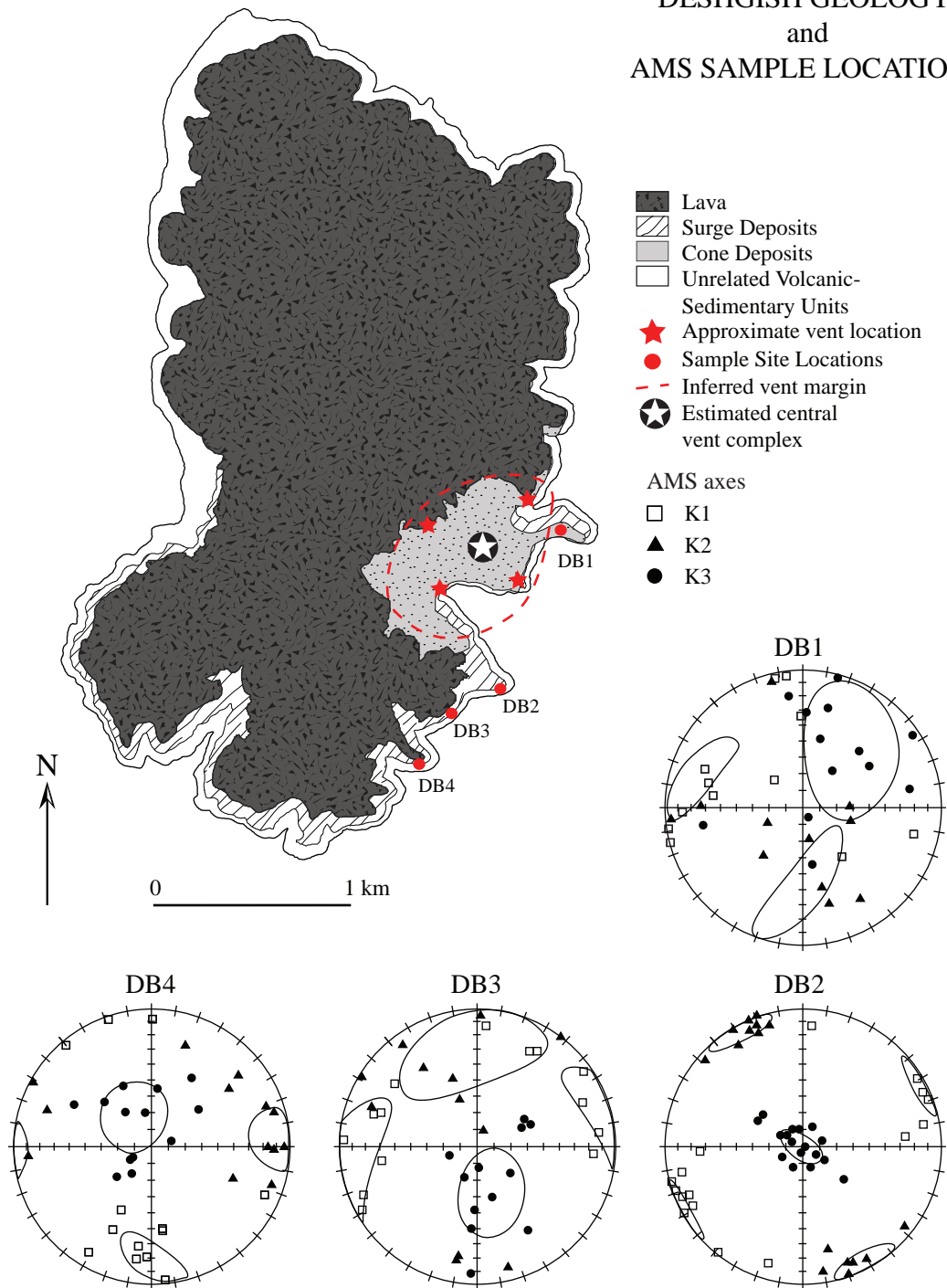
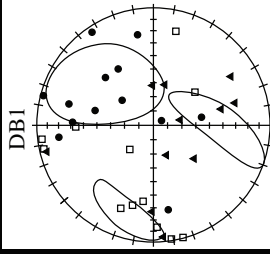
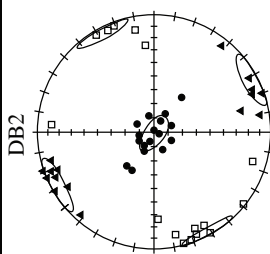
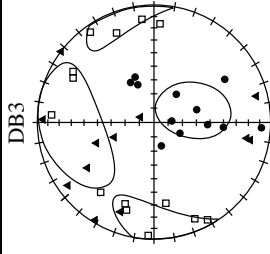
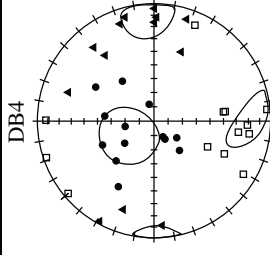


Figure 15: Deshghish Butte and associated volcanic deposits. Sample localities used in the facies analysis are shown, and denoted by their stratigraphic section designations. The center of the inferred vent zones for the phreatomagmatic deposits are denoted by the circled star.

Table 4: Deshghish AMS textural discrimination table. AMS quantitative and qualitative textural features: L, magnetic lineation (K1 axis/K2 axis); F, magnetic foliation (K2 axis/K3 axis), P, anisotropy degree (K1 axis/K3 axis); T, shape parameter  $-1 < T < 0 =$  prolate,  $0 < T < 1 =$  oblate (Jelinek, 1981), shown with associated hemispheric data plots.

Site	DB1	DB2	DB3	DB4
Distance from vent	300	550	650	800
Lateral Facies	LT2	LT2	LT3	LT3
L	1.002	1.002	1.001	1.003
F	1.002	1.006	1.001	1.002
T	0.231	0.568	0.257	0.096
AMS Facies	Disorganized	Lineated	Disorganized	Disorganized
AMS Diagrams				



## CHAPTER 5: AMS FABRIC INTERPRETATION

---

### *PROCESSES (AMS)*

The AMS results from this study can be categorized into three distinct hemispherical plot signatures that correlate with spatial regions in the field. These physical regions are defined by the lateral facies changes observed within the individual flow units, as discussed in Chapter 3. The qualitative categories observed in stereonet plots of the AMS data can also be quantified according to distinct numerical limits that are defined by the absolute T value and the  $\alpha_{95}$  K<sub>1</sub> axis D/I ratio, as presented in detail in Chapter 4.

These distinct AMS categories – essentially AMS ‘fabrics’ – can be discussed within the spatial context of 1) proximal or disorganized facies [disorganized D/I signature], 2) medial or lineated facies [lineated D/I signature], and 3) distal or girdled facies [girdled D/I facies]. The discussion that follows presents a framework for employment of these AMS characterizations as a proxy for spatial relations within pyroclastic deposits that fit into the Sohn and Chough (1989) and the Vazquez and Ort (2006) model for phreatomagmatic surge deposits.

#### *Disorganized AMS Facies Deposits*

Disorganized AMS facies typically extend laterally ~100 – 350 m from the eruptive vent, comprising very poorly sorted, matrix-supported tuff breccias, and are grouped into the LT1 and LT2 depositional facies (Table 1). The poorly organized AMS distribution of the K<sub>1</sub> axis on hemispherical plots, referred to as a disorganized D/I signature (Table 1), is characteristic of proximal phreatomagmatic surge deposits within the Hopi Buttes volcanic field (e.g. HM0, TP0, TP1, DB1, DB3, and DB4; Fig. 13A). The AMS results within this proximal disorganized zone have poorly defined poles to the plane of all measurable axes; AMS patterns exhibit T values of  $0 < T < 0.350$  (Table 1) and  $\alpha_{95}$  K<sub>1</sub> D/I ratios  $< 2$ , which correspond to the visually disorganized hemispheric plots. This pattern is best characterized in the results from the Haskie and Triplets sampling areas, particularly samples HM0, HM1 (Table 3) and TP0 (Table 2).

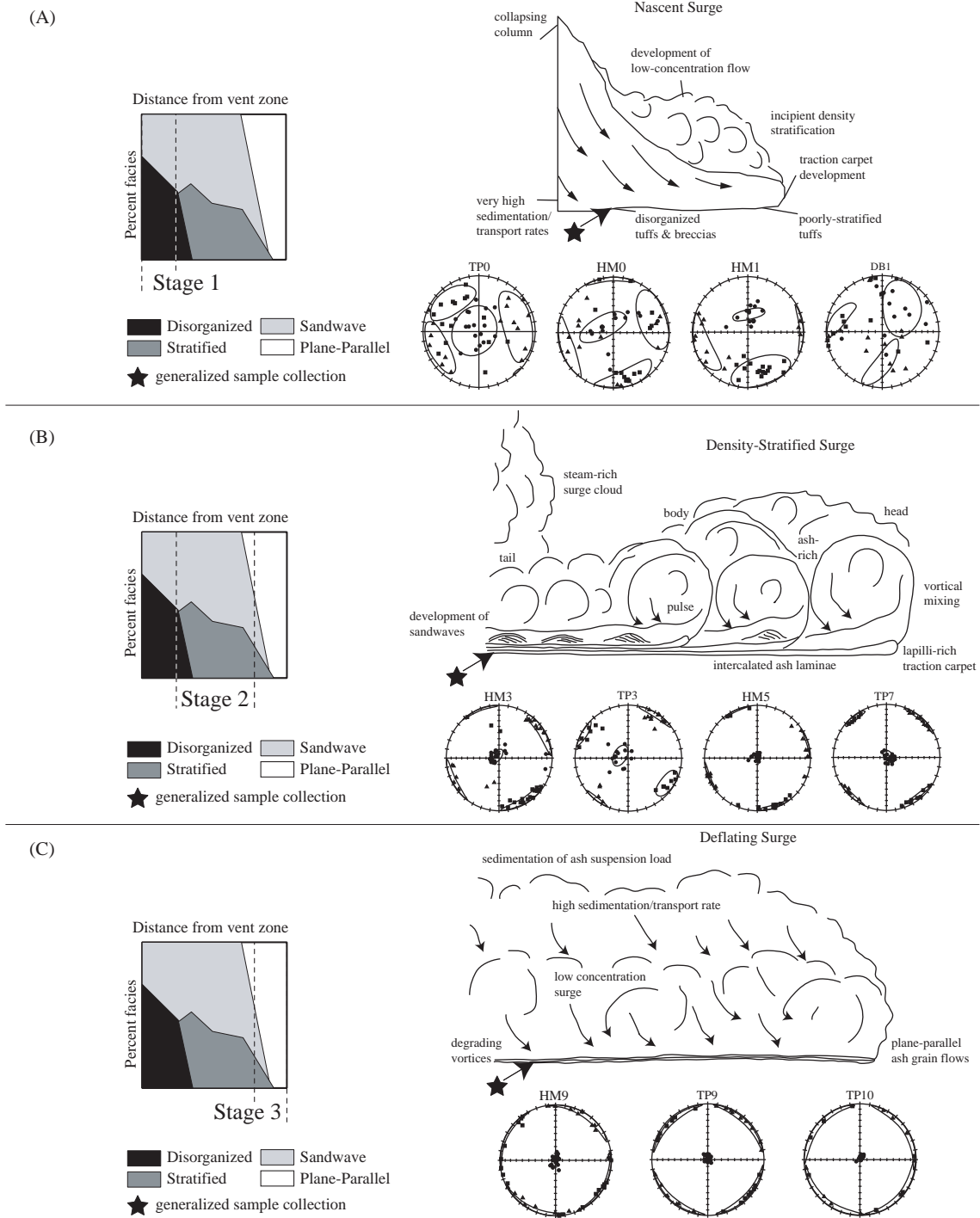


Figure 16: (A) Proximal sedimentation in Stage 1 occurs through a combination of fall back and poorly-developed lateral transport processes. Stage 1 represents the initial surge development that produced disorganized AMS signatures in the study area. (B) Stage 2-sedimentation in the study area is characterized by the lineated AMS signature, a product of the high-energy, pulsatory nature of flows and hypothesized laminar flow that occurs during medial deposition. (C) The girdled AMS signature of the distal facies developed as a result of slow aggradation and downgrading vortices during final particle settling.

Disorganized facies are derived from rapid emplacement of material deposited by the initial over-capacitated stage, and are produced at the inception of a phreatomagmatic explosion (Fig. 16A). In the field, the rapid emplacement is suggested by both the overall unsorted appearance of the deposit and the lack of sedimentary structures that would suggest a hiatus in deposition, such as erosional surfaces, paleosols, mud-cracks, tee-pee structures, and other interbedded depositional units. This rapid deposition does not afford the material within the eruptive cloud time to become moderately or well oriented during its brief transport period, evident in the scatter in both the declination and inclination of the K axes on the hemispheric plots. This disorganized deposition is supported within all scales of the exposure, from the microscopic random AMS orientations to the meso/macroscale massive tuff-breccias observed within the outcrops at Deshghish Butte, and Haskie and Triplets maars.

#### *Lineated AMS Facies Deposits*

Lineated AMS facies deposits extend laterally ~ 350 – 1050 m from individual eruptive vents and comprise moderately sorted, stratified to sand-wave-bearing, matrix- to clast-supported lapilli-tuffs. These rocks are represented by the LT2, LT3 and LT5 depositional facies (Fig. 16B). Patterns observed in the AMS data derived from these units include a lineated textural classification ( $0.350 < T < 0.700$ ) and stereonet plots that show strong clustering and organization within the  $K_1$  axis ( $2 < D/I < 5.5$ ).

Lineated AMS facies correlate with deposits produced when a surge advances downcurrent. Basal traction-carpet segregation occurs, and the surge becomes unsteady, density stratified, and highly turbulent (Fig 16B; Vazquez and Ort, 2006). Studies suggest that pulses are likely to develop in turbulent surges, as well as internal waves and vortices that permeate the surge current as local manifestations and continuous hydraulic structures (Valentine, 1987; Sohn and Chough, 1989). Individual pulses produce distinct basal beds, and/or laminae, depending on flow power, particle concentration and pyroclast size (Vazquez and Ort, 2006).

I combine macroscopic facies analysis with microscopic AMS textural analysis to suggest the following model: the depositional regime at the base of the turbulent flow becomes laminar as material aggrades, following the passage of the turbulent head. This

hypothesis is supported by the lineated character of the AMS data. The strongly grouped  $K_1$  axis is parallel to flow, suggesting localized, transient laminar flow, followed by rapid en masse deposition and compaction, as evident in the well-clustered  $K_3$  axis signature (Fig. 16B). Deposition occurs through energy loss within the flow and basal friction; post-deposition, the basal flow appears to experience continued shearing, again evident in the well-grouped character of the  $K_1$  axis. The oblate nature of the microscopic fabric at this stage – vs. the prolate character of proximal fabric – is not well explained by the AMS data, and may require additional analysis to fully conceptualize.

Although the lineated microscopic AMS signature maintains a general uniformity throughout the basal section of the deposits, the bipartite flow produces bedforms that display meso-/macroscopic textural variations that continue to evolve downcurrent. The underlying localized and transient forces of particle transport for microscopic and fine-grained material remain constant, while the coarse material is subject to a greater number of physical processes.

Whereas an interpretation based solely on meso- and macroscopic characteristics of a limited exposure could lead to several interpretations, AMS fabrics are consistent and independent of the readily visible textural characteristics of a given phreatomagmatic deposit. Without large laterally exposed outcrops where paleocurrent indicators lead to clear interpretations of emplacement and depositional processes, AMS analyses can serve as a proxy for particle-flow reconstruction.

#### *Girdled AMS Facies Deposits*

At lateral distances of ~1050-1400 m from the eruptive vent, the rocks comprise the well-sorted, plane-parallel, fine-lapilli to medium-ash tuffs represented by the LT5 and T6 depositional facies, all of which display similar girdling patterns in their AMS hemispheric plots (Fig. 16C). T values for the girdled hemispheric plots are  $0.700 < T < 1$  (Table 1) and the average  $K_1$  axis plots parallel to reconstructed flow, with D/I ratios  $> 5.5$  (Fig. 13). The transition from lineated AMS facies occurs rapidly at ~ 950 – 1050 m from the eruptive vent at the Haskie and Triplets sampling sites. Laterally contiguous deposits could not be correlated at the Deshghish location.

The girdled AMS facies form during the final phase of density current deposition, where the waning flow has lost the majority of its transport capacity for coarse material and the fine-grained material still held in suspension is beginning to settle out. On the meso- to macroscopic scale, continuous lateral motion and pulsating and periodic vortices cause the sediment grains to be deposited as distinctive grain layers in the development of low-angle bedforms (Cas and Wright, 1987). At this point, the T values indicate an oblate individual grain fabric. Although the data from this study cannot ascribe a complete explanation for this phenomenon, the grain shape is believed to be a compounding factor in the processes active during final particle transport and deposition; oblate grains are believed to be held in suspension longer, leading to deposition at the distal reaches of the flow. With nearly equal  $K_1$  and  $K_2$  axial lengths and a  $K_3$  axis hovering around  $90^\circ$ , the particles have lost any orientation relative to one another, and rest on their broad faces. Following deposition, shearing may be present as a result of downward pressure from overlying deposition, leading to lateral shear dispersion without prominent directional orientation.

There is also a possibility that there was no lateral shear and the particles are flat-lying but with any linear orientation, so the average is a girdled fabric. My model attributes the girdled AMS signature to uniform fine-grained material being deposited without a substantial unilateral, directional vector force. At this distance from the eruptive vent, there would be little to no lateral flow momentum; deposition likely occurs through flocculation and subsequent particle settling out of suspension. Minor shearing is evident in the bedforms at these distal locations (Ort and Vazquez, 2006), but compaction and pressure from downgrading vortical forces – rather than inertial flow momentum – may be more influential in producing the girdled AMS signature (Figure 16C).

## CHAPTER 6: CONCLUSIONS

---

Results from AMS analyses at Triplets maar, Haskie maar and Deshgish butte exhibit a general pattern towards increasing organization from proximal to medial locations with respect to distance from eruptive source, finally transitioning to an AMS signature that is well foliated, but less lineated at distal depositional reaches. Proximal signatures are highly disorganized at all three study locations – exemplified by samples HM0 and HM1.  $K_1$  axes plot without obvious clustering or directional trends on hemispherical graphs ( $D/I$  ratio  $< 2$ ). Medial signatures exhibit a lineated character, with the  $K_1$  axis well organized parallel to flow (e.g. samples TP3 and HM5), and a  $K_3$  axis generally clustered around  $90^\circ$ . In medial sections, a  $K_3$  axis migrating away from  $90^\circ$  may suggest a degree of particle imbrications ( $D/I$  ratio: 2-5.5). Distal deposit sections exhibit a girdled AMS signature (e.g. HM9 and TP10), with  $K_1$  axis values distributed around the horizontal plane of hemispheric plots, and a  $K_3$  axis again clustered around  $90^\circ$  ( $D/I$  ratio  $> 5.5$ ).

The physical regions of deposit characteristics are well matched to AMS signatures from proximal, medial and distal locations. Proximal to eruptive sources, disorganized AMS signatures correlate to disorganized deposits, seen as poorly sorted, matrix-supported, tuff breccias (e.g. LT1, LT2 facies). At medial distances of 350-1050m from eruptive vents, lineated AMS signatures occur within moderately sorted, variably stratified, matrix- to clast-supported lapilli tuffs (e.g. LT2, LT3, LT5 facies). Distal locations, generally greater than 1050m from eruptive sources, are exemplified by girdled AMS signatures. Deposit characteristics of these locations include well-sorted, plane-parallel, fine lapilli to medium ash tuffs (e.g. LT5 and T6 facies).

The AMS technique affords insight into the dynamic emplacement processes of phreatomagmatic pyroclastic surge deposits. The results and initial interpretations presented in this study offer a model for application of AMS signatures as a proxy for facies transitions in the field, according to the facies transition conclusions of Ort and Vazquez (2006) and Sohn and Chough (1989). It would be worthwhile, nonetheless, to evaluate the numerical results of this study against other phreatomagmatic surge

emplacement models, e.g. Wohletz and Sheridan (1986), as an initial interpretation of the present results appears to contrast with their depositional model.

The AMS results from this study have many implications, including 1) results from the present AMS fabric analysis may be extended to construct quantitative constraints for other types of dilute gravity-driven density currents, 2) this proxy could be implemented in any mass flow with analogous facies assemblages, and 3) this model can be implemented in situations for which there is little to no observable spatial relation between facies. An example of application of this latter point might be in the mining or geothermal industries: AMS signatures from exploratory drilling and sampling can help direct localized and/or regional targeting of resources commonly associated with volcanic centers.

Another example of the use of the AMS facies model might be at Deshgish Butte, where a vent location could not be identified and individual eruptive units could not be confidently sourced. If the AMS facies model was applied here, it would suggest that sampling was conducted from two separate eruptive units. Sample DB2, which exhibits the lineated facies signature, is located within close proximity to the other sampling locations, which exhibit a disorganized signature. A centrally located single vent could not be responsible for this pattern, thereby suggesting that sampled DB2 was erupted from a different, and more distant, volcanic source.

Additional questions have been raised by this research, leaving ample room for future research related to AMS fabrics and phreatomagmatic surge emplacement process. For example, only the basal sections of bipartite flows were sampled for this project. The full vertical depositional model for phreatomagmatic surges describes an upper, turbulent flow that could be further characterized with AMS analyses. Lastly, the numerical constraints for depositional facies should be verified in additional phreatomagmatic surge emplacement settings. Similar locations exist in former maar environments of southern Korea (e.g. Sohn and Chough, 1989), the Payunia basaltic field in western Argentina, the Balaton Highland Volcanic Field in Hungary, or at other maar diatremes in the Hopi Buttes area, Arizona.

## REFERENCES CITED

- Akers, J.P., Shorty, J.C., Stevens, P.R., 1971, Hydrogeology of the Cenozoic igneous rocks, Navajo and Hopi Indian reservations, Arizona, New Mexico and Utah; United States Geological Survey Professional Paper 521-D.
- Alibert, C., Michard, A., and Albarede, F., 1986, Isotope and trace element geochemistry of Colorado Plateau volcanics: *Geochemica et Cosmochimica Acta*, v. 50, p.2735-2750.
- Alibert, C., 1994, Peridotite xenoliths from western Grand Canyon and The Thumb: A probe into the subcontinental mantle of the Colorado Plateau: *Journal of Geophysical Research.*, v.99, p.21605-21620.
- Baer, E.M., Fisher, R.V., Fuller, M., Valentine, G., 1997, Turbulent transport and deposition of the Ito pyroclastic flow; determinations using anisotropy of magnetic susceptibility; *Journal of Geophysical Research*, v. 102, p. 22565-22586.
- Barker, D.S., 1996, Nephelinite-phonolite volcanism: *In* Mitchell, R.H., editor, *Undersaturated Alkaline Rocks; Mineralogy, Petrogenesis, and Economic Potential-* Mineralogical Association of Canada Short Course Series, v. 24, p.23-45.
- Bennett, V.C., and DePaolo, 1987, Proterozoic crustal history of the western United States as determined by neodymium isotopic mapping: *Geological Society of America Bulletin*, v.99, p.674-685.
- Buchanan, D.J., 1974, A model for fuel-coolant interactions: *Journal of Applied Physics*, v.7, p.1441-1457.
- Bird, P., 1984, Laramide crustal thickening event in the Rocky Mountain foreland and Great Plains: *Tectonics*, v.3, p. 741-785.
- Busby-Spera, C.J., and White, J.D.L., 1987, Variation in peperite textures associated with differing host-sediment properties: *Bulletin of Volcanology*, v.49, p.765-775.
- Burgisser, A., Gardner, J.E., 2006, Using hydraulic equivalences to discriminate transport processes of volcanic flows: *Geology*, v. 34, no. 3, p.157-160.



- Burgisser, A., Bergantz, G., 2002, Reconciling pyroclastic flow and surge: the multiphase physics of pyroclastic density currents: *Earth and Planetary Science Letters*, v. 202, p. 405-418.
- Büttner, R., Dellino P., Zimanowski B., 1999, Identifying magma–water interaction from the surface features of ash particle: *Nature*, v. 401, p. 688-690
- Büttner, R., Zimanowski B., 1998, Physics of thermohydraulic explosions: *Physical Review E*, v. 57, p. 5726-5729.
- Cagnoli, B., Tarling, D.H., 1997, The reliability of anisotropy of magnetic susceptibility (AMS) data as flow direction indicators in friable base surge and ignimbrite deposits: Italian examples: *Journal of Volcanology and Geothermal Research*, v. 75, p. 309-320.
- Cañón-Tapia, E., 2001, Factors affecting the relative importance of shape and distribution anisotropy in rocks: theory and experiments; *Tectonophysics*, v. 340, p. 117-131.
- Cas, R.F., Wright, J.V., 1985, *Volcanic Successions*, Chapman and Hall Press, London, U.K., 528 p.
- Chough, S.K., and Sohn, Y.K., 1990, Depositional mechanics and sequences of base surges, Songaksan tuff ring, Cheju Island, Korea; *Sedimentology*, v. 37, p. 1115-1135.
- Colella, A., and Hiscott, R.N., 1997, Pyroclastic surges of the Pleistocene Monte Guardia sequence (Lipari Island, Italy): depositional processes: *Sedimentology*, v. 44, p. 47-66.
- Condie, K.C., 1986, Geochemistry and tectonic setting of Early Proterozoic supercrustal rocks in the southwestern United States: *Journal of Geology*, v.94, p. 845-864.
- Condie, K.C., 1992, Proterozoic terrain and continental accretion in southwestern North America: *In* Condie, K.C., ed., *Developments in Precambrian geology*, v.10 Elsevier Press, Amsterdam, Netherlands, p. 447-480.
- Crandell, D.R., 1975, Assessment of volcanic risk on the island of Oahu, Hawaii: U.S. Geological Survey Open-File Report 75-287, 18 p.
- Condit, C.D., and Conner, C.B., 1996, Recurrence rates for volcanism in basaltic volcanic fields: an example from the Springerville volcanic field, Arizona: *Geological Society of America Bulletin*, v. 108, p. 1225-1241.

- Conway, F.M., Conner, C.B., Hill, B.E., Condit, C.D., Mullaney, K., and Hall, C.M., 1998, Recurrence rates of basaltic volcanism in SP cluster, San Francisco volcanic field, Arizona: *Geology*, v. 26, p. 655-658.
- Dallegge, T., 1999, Correlation and chronology of the Miocene-Pliocene Bidahochi Formation, Navajo and Hopi Nations, Northeastern Arizona, [Masters Thesis]: Northern Arizona University, 304 p.
- Dallegge, T.A., Ort, M.H., McIntosh, W.C., and Perkins, M.E., 2003, Age and depositional basin morphology of the Bidahochi Formation and implications for the ancestral upper Colorado River; Young, R., [ed.], Grand Canyon National Park Association, Grand Canyon Symposium Monograph, p. 47-51.
- Damon, P.E., Shafiquallah, M., Harris, R., 1991, Compilation of unpublished Arizona K-Ar dates from the University of Arizona laboratory of Isotope Geochemistry 1971-1991: Arizona Geological Survey Open-File Report 96-18, 56 p.
- Damon, P.E., Spencer, 2000, K-Ar geochronologic survey of the Hopi Buttes volcanic field; Young, R., [ed.], Grand Canyon National Park Association, Grand Canyon Symposium Monograph, p 53-56.
- Delaney, P.T., Pollard, D.D., Ziony, J.I., and Mckee, E.H., 1986, Field relations between dikes and joints: emplacement processes and paleo-stress analysis: *Journal of Geophysical Research*, v.91, p.4920-4938.
- Ealy, P.D., 1994, Gravity and magnetic analysis of the Hopi Buttes volcanic field, Navajo Nation, Northeastern Arizona [Masters Thesis]: Northern Arizona University, 80 p.
- Ellwood, B.B., 1982, Estimates of flow direction for calc-alkaline welded tuffs and paleomagnetic data reliability from anisotropy of magnetic susceptibility measurements: Central San Juan Mountains, southwest Colorado; *Earth and Planetary Science Letters*, v. 59, p. 303-314.
- Fiedler, A., Fröhlich, G., Müller, G., Benz, R., Bürger, M., Schwalbe, W., Unger, H., 1980, Theoretische und eexperimentelle Untersuchungen zur Dampfexplosion: IKE 2 BMFT RS 206, p. 72.
- Fisher, R.V., 1983, Flow transformations in sediment gravity flows: *Geology*, v. 11, p. 273-274.

- Fisher, R.V., and Schmincke, H.-U., 1984, Pyroclastic rocks, Springer-Verlag, Berlin, 472 p.
- Fisher, R.V., Orsi, G., Ort, M.H., Heiken, G., 1993, Mobility of a large-volume pyroclastic flow -- Emplacement of the Campanian Ignimbrite, Italy: *Journal of Volcanology and Geothermal Research*, v. 56, p.205-220.
- Frazzetta, G., La Volpe, L., and Sheridan, M.F., 1983, Evolution of the Fossa cone, Vulcano: *Journal of Volcanology and Geothermal Research*, v. 17, p. 329-360.
- Grunewald, U., Zimanowski, B., Büttner, R., Phillips, L.F., Heide, K., Büchel, G., 2007, MFCI experiments on the influence of NaCl-saturated water on phreatomagmatic explosions: *Journal of Volcanology and Geothermal Research*, v. 159, p. 126-137.
- Hack, J.T., 1942, Sedimentation and volcanism in the Hopi Buttes, Arizona; *Bulletin of the Geological Society of America*, v.53, p. 335-372.
- Hackman, R.J., and Olson, A.B., 1977, Map showing geology, structure, and uranium deposits of the Gallup 1° x 2° quadrangle, New Mexico and Arizona; USGS I-981.
- Harms, J.C., Southard, J.B., Walker, R.G., 1982, Structures and sequences in clastic rocks: *Society for Sedimentary Geology Short Course No. 9*, p. 8-51.
- Hargraves, R.B., Johnson, D., Chan, C.Y., 1991, Distribution anisotropy: the cause of AMS in igneous rocks?; *Geophysical Research Letters*, v. 18, p. 2193-2196
- Hillhouse, J.W., Wells, R.E., 1991, Magnetic fabric, flow directions, and source area of the lower Miocene Peach Springs Tuff in Arizona, California, and Nevada; *Journal of Geophysical Research*, v. 96, p. 12443-12460.
- Hooten, J.A., 1999a, Phreatomagmatic diatremes of the western Hopi Buttes volcanic field, Navajo Nation, Arizona [Masters thesis], Northern Arizona University, 140 p.
- Hooten, J.A., 1999b, Map of the volcanic geology of the Castle Butte Trading Post vicinity, Hopi Buttes, Navajo Nation, Arizona: Arizona Geologic Survey. Map CM-00-A.
- Hooten, J.A., Ort, M.H., 2002, Peperite as a record of early stage phreatomagmatic fragmentation processes: An example from the Hopi Buttes volcanic field, Navajo

- Nation, Arizona, USA: *Journal of Volcanology and Geothermal Research*, v.114, p. 95-106.
- Hrouda, F., 1982, Magnetic anisotropy of rocks and its application in geology and geophysics: *Geophysical Survey*, v. 5, p. 37-82.
- Incoronato, A., Addison, F.T., Tarling, D.H., Nardi, G., Pescatore, T., 1983, Magnetic fabric investigations of pyroclastic deposits from Phlegrean Fields, southern Italy: *Nature*, v.306, p. 461-463.
- Jelinek, V., 1977, The statistical theory of measuring anisotropy of magnetic susceptibility of rocks and its application, *Geofyzika Brno*, Institute of Geophysics, Charles, University, 88p.
- Jelinek, V., 1981, Characterization of the magnetic fabric of rocks: *Tectonophysics*, v.79, p. 63-67.
- Knight, M.D., Walker, G.P.L., Ellwood, B.B., Diehl, J.F., 1986, Stratigraphy, paleomagnetism, and magnetic fabric of the Toba Tuffs: Constraints on the sources and eruptive styles: *Journal of Geophysical Research*, v. 91, p. 10355-10382.
- Lajoie, J., Lanzafame, G., Rossi, P.L., Tranne, C.A., 1992, Lateral facies variations in hydromagmatic pyroclastic deposits at Linosa, Italy: *Journal of Volcanology and Geothermal Research*, v. 54, p. 135-143.
- Le Penneç, J.L., Chenn, Y., Diot, G., Froger, J.L., Gourhaud, A., 1998, Interpretation of anisotropy of magnetic susceptibility fabric of ignimbrites in terms of kinematic and sedimentological mechanisms. An Anatolian case-study. *Earth Planet: Science Letters*, v. 157, p. 105-127.
- MacDonald, W.D., Palmer, H.C., 1990, Flow directions in ash-flow tuffs: a comparison of geological and magnetic susceptibility measurements, Tshirege member (upper Bandelier Tuff), Valles caldera, New Mexico, USA: *Bulletin of Volcanology*, v. 53, p. 45-59.
- Maldonado, F., and Nealey, D.L., 1995, Introduction: *In Geological studies in the Basin and Range-Colorado Plateau Transition Zone in southeastern Nevada, southwestern Utah, and northwestern Arizona*, 1995: United States Geological Survey Bulletin 2153, p.1-4.

- Moore, J.G., 1967, Base surge in recent volcanic eruptions: *Bulletin of Volcanology*, v. 30, p. 337-363.
- Muxworthy, A.R., Williams, W., 2004, Distribution anisotropy: the influence of magnetic interactions on the anisotropy of magnetic remanence: Martin-Hernandez, et al. [eds], *Magnetic Fabric: Methods and Applications*, Geological Society, London, Special Publications, v. 238, p. 37-47.
- Nealey, L.D., and Sheridan, M.F., 1989, Post-Laramide volcanic rocks of Arizona and northern Sonora, Mexico, and their inclusions; in Jenney, J.P., and Reynolds, S.J., *Geologic evolution of Arizona: Arizona Geological Society. Digest 17*, p. 609-647.
- Nye, J.F., 1985, *Physical properties of crystals: 2<sup>nd</sup> ed*, Clarendon Press, Oxford, 329p.
- Ort, M.H., 1993, Eruptive processes and caldera formation in a nested down-sag collapse caldera: Cerro Panizos, central Andes Mountains: *Journal of Volcanology and Geothermal Research*, v. 56, p. 221-252.
- Ort, M.H., Dallegge, T.A., Vazquez, J.A., White, J.D.L., 1998, Volcanism and sedimentation in the Mio-Pliocene Bidahochi Formation, Navajo Nation, northeastern Arizona. *Geologic Excursions in northern and Central Arizona: Field trip Guidebook for Geological Society of America Rocky Mountain Section Meeting, Arizona*. (Ed) Ernest M. Duebendorfer. p.35-57.
- Ort, M.H., Rosi, M., Anderson, C.A., 1999, Correlation of deposits and vent locations of the proximal Campanian Ignimbrite deposits, Campi Flegrei, Italy, based on natural remanent magnetization and anisotropy of magnetic susceptibility characteristics: *Journal of Volcanology and Geothermal Research*, v. 91, p. 167-178.
- Ort, M.H., Orsi, G., Pappalardo, L., and Fisher, R.V., 2003, Anisotropy of magnetic susceptibility studies of depositional processes in the Campanian Ignimbrite, Italy: *Bulletin of Volcanology*, v. 65, p. 55-72.
- Palmer, H.C., McDonald, W.D., Hayatsu, A., 1991, Magnetic, structural and geochronologic evidence bearing on volcanic sources and Oligocene deformation of ash flow tuffs, northeast Nevada; *Journal of Geophysical Research*, v. 96, p. 2185-2202.
- Parsons, T., and McCarthy, J., 1995, The active southwest margin of the Colorado Plateau: Uplift of the mantle origin: *Geological Society of America Bulletin*, v.107, p.139-147.

- Porreca, M., M. Mattei, G. Giordano, D. De Rita, and R. Funicello, 2003, Magnetic fabric and implications for pyroclastic flow and lahar emplacement, Albano maar, Italy: *Journal of Geophysical Research*, v.108. p. 2264
- Regan, A.B., 1924, Stratigraphy of the Hopi Buttes volcanic field; *Pan-American Geologist*, v. 41, p. 355-366.
- Repenning, C.A., and Irwin, J.H., 1954, Bidahochi Formation of Arizona and New Mexico: *American Association of Petroleum Geologists Bulletin*; v. 38, p. 1821-1826.
- Roden, M.F., Smith, D., and Murthy, V.R., 1990, Chemical Constraints on lithosphere composition and evolution beneath the Colorado Plateau: *Journal of Geophysical Research*, v.95, p.2811-2831.
- Roma geomagnetism, 2003, <http://www.ingv.it/~roma/SITOINGLESE/activities/geomagnetismo/paleomagnetism/anisotropy.html>, date visited 2004.
- Seaman, S.J., McIntosh, W.C., Geissman, J.W., Williams, M.L., Elston, W.E., 1991, Magnetic fabrics of the Bloodgood Canyon and Shelley Peak Tuffs, southwestern New Mexico: implications for emplacement and alteration processes; *Bulletin of Volcanology*, v. 53, p. 460-476.
- Shafiquallah, M., and Damon, P.E. 1985, Geochronology of the Hopi Buttes volcanic field, northeastern Arizona [abstract], in *Abstracts of the symposium on Southwest geology and paleontology: Flagstaff, Arizona, Museum of Northern Arizona*, p. 9.
- Sheridan, M.F., Barberi, F., Rosi, M., and Santacroce, R., 1981, A model for Plinian eruptions of Vesuvius: *Nature*, v. 289, p. 282-285.
- Sheridan, M.F., and Wohletz, K.H., 1983, Hydrovolcanism: Basic considerations and review: *Journal of Volcanology and Geothermal Research*, v. 17, p. 1-29.
- Shoemaker, E.M., Roach, C.H., and Byers, F.M., Jr., 1962, Diatremes and uranium deposits in the Hopi Buttes, Arizona; in Engel, A.E.J., James, H.L., and Leonard, B.F., editors, *Petrologic studies - A volume in honor of A.F. Buddington*, Geol. Soc. Am., New York, pp. 327-355.
- Smith, R.B., 1978, Seismicity, crustal structure, and intraplate tectonics of the interior of the western Cordillera: *In* Simith, R.G., Eaton, G.P., eds, 1989, *Cenozoic*

- Tectonic and Regional Geophysics of the Western Cordillera: GSA Memoir 152, p.111-145.
- Sutton, R.L., 1974, The geology of Hopi Buttes, Arizona; in Geology of northern Arizona with notes on archeology and paleoclimate, Part II; Geological Society of America, Rocky Mtn. Section, Guidebook 27, p. 647-671.
- Tarling, D.G., Hrouda, F., 1993, The magnetic anisotropy of rocks: Chapman and Hall Press, London , U.K., 217 p.
- Thompson, G.A., and Zoback, M.L., 1979, Regional geophysics of the Colorado Plateau: Tectonophysics, v.61, p.149-181.
- Tingey, D.G., Christiansen, E.H., Best, M.G., Joaquin, R., and Daniel, R.L., 1991, Tertiary minette and melanephelinite dikes, Watsatch Plateau, Utah: records of mantle heterogeneities and changing tectonics: Journal of Geophysical Research, v.96, p.13529-13544.
- Ulrich, G.E., Billingsley, G.H., Hereford, R., Wolfe, E.W., Nealey, L.D., and Sutton, R.L., 1984, Map showing geology, structure, and uranium deposits of the Flagstaff 1° x 2° quadrangle, Arizona: United States Geologic Survey. Misc. Inv. Map I-1446.
- Ulrich, G.E., Condit, C.D., Wenrich, K.J., Wolfe, E.W., Holm, R.F., Nealey, L.D., Conway, F.M., Aubele, J.C., and Crumpler, L.S., 1989, Excursion 5A: Miocene to Holocene volcanism and tectonism of the southern Colorado Plateau, Arizona; in Chapin, C.E., and Zidek, J., editors, Field excursions to volcanic terrains in the western United States, volume I: Southern Rocky Mountain region, New Mexico Bur. Mines Min. Res. Mem. 46, p. 1-41.
- Valentine, G.A, 1987, Stratified flow in pyroclastic surges: Bulletin of Volcanology, v. 49, p. 616-630.
- Vazquez, J.A., 1998, Maar volcanism in the Wood Chop Mesa area, Hopi Buttes volcanic field, Navajo Nation, Arizona; Masters thesis, Northern Arizona University, 210 p.
- Vazquez, J.A., 1999, Map of the volcanic geology of the Wood Chop Mesa area, Hopi Buttes (Tsezhin Bii), Navajo Nation, Arizona: Arizona Geological Survey

Contributed Map CM-99-A, scale 1:12,000.

- Vazquez, J.A., Ort, M.H., 2006, Facies variation of eruption units produced by the passage of single pyroclastic surge currents, Hopi Buttes volcanic field, USA: *Journal of Volcanology and Geothermal Research*, v.154 p.222–236.
- Wendlandt, E., DePaolo, D.J., and Baldrige, W.S., 1993, Nd and Sr isotope chronostratigraphy of Colorado Plateau lithosphere: Implication for magmatic and tectonic underplating of the continental crust: *Earth and Planetary Science Letters*, v.116, p.23-43.
- Wenrich, K.J., 1989, Hopi Buttes volcanic field, in Chapin, C.E., and Zidek, J., (eds), *Field excursions to volcanic terrains in the western United States, volume 1; Southern Rocky Mountain Region: New Mexico Bureau of Mines and Mineral Resources Memoir 46*, p. 21-33.
- Wenrich, K.J., and Mascarenas, J.F., 1982a, Diatremes of the Hopi Buttes, Arizona: Chemical and statistical analyses: U.S. Geological Survey Open-File Report. 82-0740, 131 pp.
- Wenrich, K.J., and Mascarenas, J.F., 1982b, Maps showing uranium-bearing diatremes of the Hopi Buttes, Arizona: United States Geologic Survey MF-1310.
- White, J.D.L., 1990a, Depositional architecture of a maar-pitted playa: sedimentation in the Hopi Buttes volcanic field, northeastern Arizona, USA: *Sedimentary Geology*, v.67, p.55-84.
- White, J.D.L., 1990b, Hydrovolcanism and associated sedimentation in the Mio-Pliocene Hopi Buttes volcanic field, northeastern Arizona, USA [Ph.D. Dissertation]: Santa Barbara, University of California, 160 pp.
- White, J.D.L., 1991, Maar-diatreme phreatomagmatism at Hopi Buttes, Navajo Nation (Arizona), USA: *Bulletin of Volcanology*, v.53, p.239-258.
- White, J.D.L., 1992, Pliocene subaqueous fans and Gilbert-type deltas in maar crater lakes, Hopi Buttes, Navajo Nation (Arizona), USA: *Sedimentology*, v.39, p.931-946.
- White, J.D.L., 1996, Impure coolants and interaction dynamics of phreatomagmatic eruptions: *Journal of Volcanology and Geothermal Research*, v.74, p.155-170.



- Williams, H., 1936, Pliocene volcanoes of the Navajo-Hopi country; Bulletin of the Geological Society of America, v. 47, p.111-172.
- Wohletz, K.H., 2002, Water/magma interaction: some theory and experiments on peperite formation: Journal of Volcanology and Geothermal Research, v. 114, p. 19-35.
- Wohletz, K.H., 1986, Explosive magma-water interactions: thermodynamics, explosion mechanisms, and field studies: Bulletin of Volcanology, v. 48, p. 245-264.
- Wohletz, K.H., and Sheridan, M.F., 1983, Hydrovolcanic explosions II: Evolution of basaltic tuff rings and tuff cones: American Journal of Science, v. 283, p. 385-413.
- Wohletz, K.H., and McQueen, R.G., 1984a, Experimental studies of hydromagmatic volcanism, in Explosive volcanism: Inception, evolution and hazards; Washington, D.C., National Academy Press: Studies in Geophysics, p. 158-169.
- Wohletz, K.H., and McQueen, R.G., 1984b, Volcanic and stratospheric dust-like particles produced by experimental water-melt interactions; Geology, v. 12, p. 591-594.
- Wohletz, K.H., and Heiken, G., 1992, Volcanology and geothermal energy: Univ. Calif. Press, Berkeley, 432 p.
- Wolff, J.A., Ellwood, B.B., Sachs, S.D., 1989, Anisotropy of magnetic susceptibility in welded tuffs: application to a welded-tuff dyke in the Tertiary Trans-Pecos Texas volcanic province, USA: Bulletin of Volcanology, v. 51, p. 299-310.
- Zanella et al., 1999, Magnetic fabric and remanent magnetization of pyroclastic surge deposits from Vulcano (Aeolian Islands, Italy): Journal of Volcanology and Geothermal Research, v.93, p. 217-236.
- Zimanowski, B., Fröhlich, G., and Lorenz, V., 1991, Quantitative experiments on phreatomagmatic explosions: Journal of Volcanology and Geothermal Research, v. 48, p. 341-358.
- Zimanowski, B., Büttner, R., Lorenz, V., and Häfele, H.G., 1997, Fragmentation of basaltic melt in the course of explosive volcanism: Journal of Geophysical Research, v. 102, no. B1, p. 803-814.



## APPENDICES

---

### **Appendix 1:** ChRM Data for Study Sites.

Points on plots indicate the declination and inclination of magnetic north for each specimen, as recorded during rock formation.

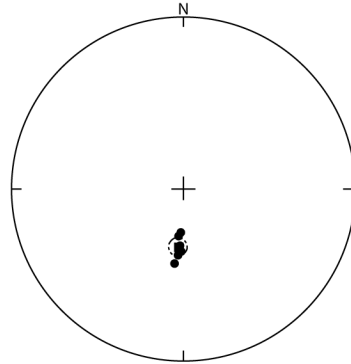
Plot Legend:

- southern hemisphere declination and inclination
- average of southern hemisphere declination and inclination
- $\alpha_{95}$  confidence interval for all southern hemisphere samples at each site
- northern hemisphere declination and inclination
- average of northern hemisphere declination and inclination
- $\alpha_{95}$  confidence interval for all northern hemisphere samples at each site

## Appendix 1.1: Triplets ChRM Data

### TRP2 MAG COMPASS CORRECTED

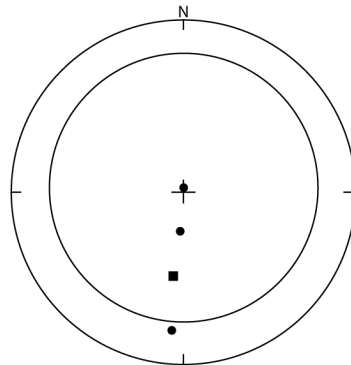
Sample	Dec	Inc	alpha
TRP21	1.0	119.9	
TRP22	2.0	110.3	
TRP23	3.0	117.0	
TRP24	4.0	121.5	
TRP25	5.0	112.6	
TRP26	6.0	126.0	



MeanD	MeanT	k	alpha	R	RC	MDS	Dist
-176.4	-62.1	189.7	4.9	5.9736428	18.5	TRP23	8.2
-177.0	-63.7	285.3	4.5	4.9859786	16.0	TRP26	6.0
-176.8	-62.3	413.7	4.5	3.9927483	14.7	TRP21	5.2
-177.3	-60.5	1135.1	3.7	2.9982381	11.0	TRP24	2.5
-177.5	-59.3	2677.5	4.8	1.9996265	14.6	TRP25	1.1
						TRP22	

### TRP3 MAG COMPASS CORRECTED

Sample	Dec	Inc	alpha
TRP31	1.0	235.8	
TRP32	2.0	87.1	
TRP33	3.0	316.5	
TRP34	4.0	326.7	
TRP35	5.0	259.5	
TRP36	6.0	208.3	

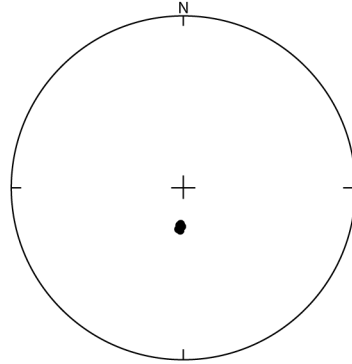


MeanD	MeanT	k	alpha	R	RC	MDS	Dist
-172.5	49.4	0.9	180.0	0.3079972	180.0	TRP32	8.2
-176.0	44.9	1.1	180.0	1.3063978	180.0	TRP31	6.0
-176.0	39.9	1.8	105.9	2.2947872	180.0	TRP36	5.2
-174.5	62.4	4.9	63.0	2.5928195	180.0	TRP35	2.5
-173.2	82.3	29.3	47.9	1.9658904	180.0	TRP33	1.1
						TRP34	

**Appendix 1.1: Triplets ChRM Data (continued)**

TRP6 MAG COMPASS CORRECTED

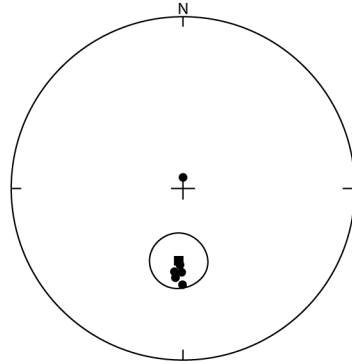
Sample	Dec	Inc	alpha
TRP61	1.0	108.2	
TRP62	2.0	107.6	
TRP63	3.0	110.6	
TRP64	4.0	109.2	
TRP65	5.0	109.6	
TRP66	6.0	107.9	
TRP67	7.0	110.1	



MeanD	MeanT	k	alpha	R	RC	MDS	Dist
-176.0	71.0	3608.5	1.0	6.9983373	4.1	TRP62	8.2
-175.8	71.2	4180.9	1.0	5.9988041	3.9	TRP61	6.0
-176.4	71.5	5633.7	1.0	4.9992900	3.6	TRP66	5.2
-176.7	71.8	6849.7	1.1	3.9995620	3.6	TRP65	2.5
-177.0	72.1	8710.9	1.3	2.9997704	4.0	TRP63	1.1
178	72.1	28926.2	1.5	1.9999654	4.4	TRP64	0.9

TRP7 MAG COMPASS CORRECTED

Sample	Dec	Inc	alpha
TRP71	1.0	137.3	60.4
TRP72	2.0	130.4	63.6
TRP73	3.0	126.7	63.9
TRP74	4.0	130.4	63.6
TRP75	5.0	84.6	
TRP76	6.0	133.8	60.1
TRP77	7.0	130.6	

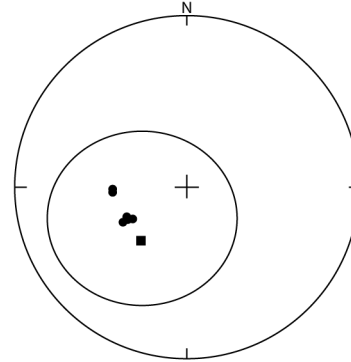


MeanD	MeanT	k	alpha	R	RC	MDS	Dist
-176.2	54.7	20.8	13.6	6.7112107	55.8	TRP7	40.7
-176.2	48.5	424.9	3.3	5.9882312	12.3	TRP7	6.1
-175.6	49.6	807.7	2.7	4.9950476	9.5	TRP7	3.8
-175.2	48.7	1338.0	2.5	3.9977579	8.2	TRP7	2.6
-175.7	49.6	2447.8	2.5	2.9991829	7.5	TRP7	1.7
-177.0	49.6	7817.9	2.8	1.9998721	8.6	TRP7	0.6
						TRP7	

**Appendix 1.1: Triplets ChRM Data (continued)**

TRP8 MAG COMPASS CORRECTED

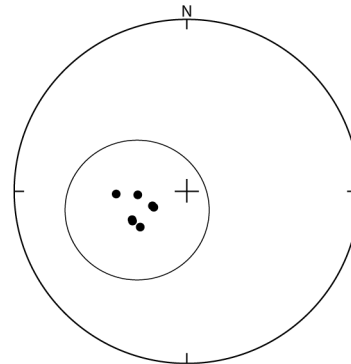
Sample	Dec	Inc	alpha
TRP81	238.9	59.8	
TRP82	241.7	57.2	
TRP83	267.8	53.9	
TRP84	241.9	54.7	
TRP85	265.3	53.7	
TRP86	243.6	58.1	
TRP87	240.6	59.9	



MeanD	MeanT	k	alpha	R	RC	MDS	Dist
-139.4	56.0	1.6	77.7	3.1605566	180.0	TRP83	151.0
-127.2	57.5	2.6	52.5	4.0641212	180.0	TRP85	156.4
-118.6	57.9	1212.1	2.2	4.9966998	7.7	TRP84	3.3
-118.8	58.8	2352.8	1.9	3.9987249	6.1	TRP81	1.6
-118.0	58.4	2610.8	2.4	2.9992340	7.3	TRP87	1.7
-117.4	57.7	1721.1	3.0	1.9998596	9.0	TRP82	0.7
						TRP86	

TRP9 MAG COMPASS CORRECTED

Sample	Dec	Inc	alpha
TRP91	242.8	59.7	
TRP92	275.5	66.3	
TRP93	274.1	55.2	
TRP94	241.3	59.9	
TRP95	232.7	61.3	
TRP96	241.6	71.3	
TRP97	244.8	71.4	

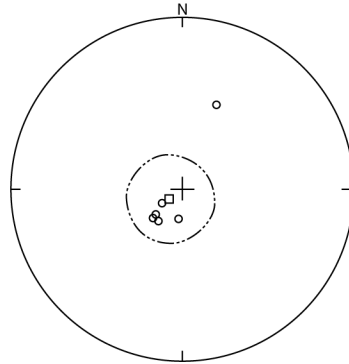


MeanD	MeanT	k	alpha	R	RC	MDS	Dist
-120.6	-24.8	1.3	101.4	2.4474723	180.0	TRP91	127.3
-110.8	-36.8	1.8	74.9	3.1555872	180.0	TRP95	99.0
-107.1	-53.2	2.6	59.9	3.4560728	180	TRP94	113.5
-103.4	-66.4	78.7	10.4	3.9618924	34.1	TRP93	12.1
-108.6	-70.0	234.2	8.1	2.9914591	24.4	TRP92	6.1
-116.8	-71.4	12427.6	2.2	1.9999195	6.8	TRP96	0.5
						TRP97	

## Appendix 1.2: Haskie Maar ChRM Data

### HM3 MAG COMPASS CORRECTED

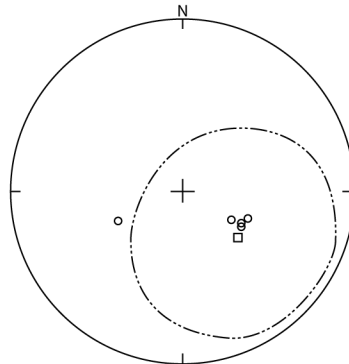
Sample	Dec	Inc	alpha
HM31	23.0	-46.3	
HM32	185.3	-75.6	
HM33	234.5	-78.3	
HM34	216.8	-71.0	
HM35	225.3	-72.4	
HM36	223.3	-70.3	



MeanD	MeanT	k	alpha	R	RC	MDS	Dist
-128.7	-82.6	11.3	20.8	5.5573540	82.8	HM31	50.3
-142.6	-74.1	188.0	5.6	4.9787178	19.7	HM32	8.4
-136.1	-73.1	383.7	4.7	3.9921813	15.3	HM33	5.8
-138.3	-71.3	2073.3	2.7	2.9990354	8.2	HM34	1.6
-135.8	-71.4	2725.3	4.8	1.9996331	14.5	HM35	1.1
						HM36	

### HM4 MAG COMPASS CORRECTED

Sample	Dec	Inc	alpha
HM41	244.8	56.0	
HM42	119.3	-57.6	
HM43	119.1	-57.6	
HM44	113.4	-55.8	
HM45	120.3	-57.3	
HM46	120.8	-62.3	

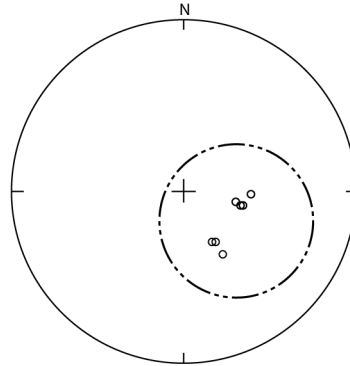


MeanD	MeanT	k	alpha	R	RC	MDS	Dist
129.5	-55.5	2.7	50.8	4.1432920	180.0	HM41	144.9
118.5	-58.1	766.2	2.8	4.9947791	9.7	HM42	4.3
118.0	-57.1	1777.2	2.2	3.9983120	7.1	HM43	2.8
119.6	-57.5	43919.4	0.6	2.9999545	1.8	HM44	0.4
119.2	-57.6	99999.9	0.2	1.9999990	0.7	HM45	0.1
						HM46	

## Appendix 1.2: Haskie Maar ChRM Data (continued)

### HM5 MAG COMPASS CORRECTED

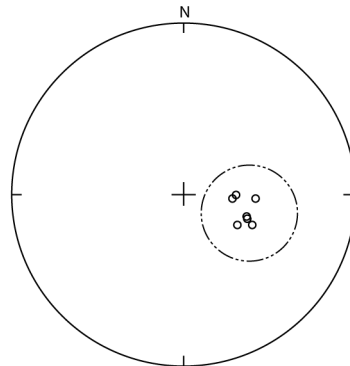
Sample	Dec	Inc	alpha
HM51	101.1	-65.1	
HM52	100.2	-60.0	
HM53	145.6	-61.8	
HM54	147.8	-54.6	
HM55	90.1	-57.3	
HM56	150.4	-62.4	
HM56	100.4	-61.1	



MeanD	MeanT	k	alpha	R	RC	MDS	Dist
144.1	-25.5	1.2	120.2	2.1079354	180.0	HM53	103.6
129.8	-44.8	1.4	96.9	2.5372026	180.0	HM56	124.5
114.9	-56.4	2.2	67.7	3.2114918	180.0	HM54	136.0
97.6	-61.0	377.5	4.7	3.9920530	15.4	HM55	5.3
100.5	-62.1	905.8	4.1	2.9977920	12.4	HM51	3.0
100.3	-60.6	10768.4	2.4	1.9999071	7.3	HM57	0.6
						HM52	

### HM6 MAG COMPASS CORRECTED

Sample	Dec	Inc	alpha
HM61	92.6	-64.8	
HM62	95.6	-66.5	
HM63	109.0	-58.0	
HM64	94.1	-54.8	
HM65	113.7	-54.2	
HM66	119.9	-59.9	
HM67	111.4	-57.2	



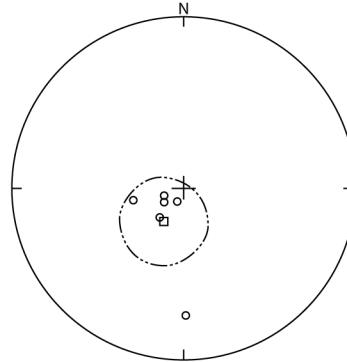
MeanD	MeanT	k	alpha	R	RC	MDS	Dist
-148.8	33.0	1.1	180.0	1.3315942	180.0	HM64	131.7
-128.4	46.4	1.3	119.2	2.1321361	180.0	HM61	151.2
-119.5	53.4	2.0	73.4	3.0470083	180.0	HM62	158.6
-113.4	57.4	562.6	3.9	3.9946678	12.6	HM66	4.2
-111.4	56.5	1150.1	3.6	2.9982610	11.0	HM65	2.6
-110.2	57.6	5722.1	3.3	1.9998252	10.0	HM63	0.8
						HM67	



### Appendix 1.3: Haskie Maar East ChRM Data

#### HME1 MAG COMPASS CORRECTED

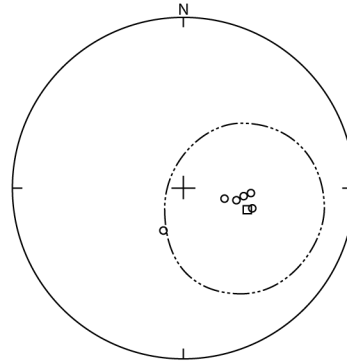
Sample	Dec	Inc	alpha
ES11	256.8	-65.3	
ES12	249.2	-80.0	
ES13	178.4	-26.2	
ES14	204.7	-83.1	
ES15	213.2	-71.3	
ES16	213.2	-78.6	



MeanD	MeanT	k	alpha	R	RC	MDS	Dist
-149.0	-71.0	11.3	20.8	5.5565882	82.9	ES13	48.5
-124.3	-76.5	80.5	8.6	4.9502892	30.3	ES11	13.0
-135.4	-78.7	168.8	7.1	3.9822226	23.1	ES15	7.9
-127.7	-81.0	398.1	6.2	2.9949756	18.7	ES14	4.3
-118.9	-79.4	1319.8	6.9	1.9992423	20.9	ES12	1.6

#### HME3 MAG COMPASS CORRECTED

Sample	Dec	Inc	alpha
ES31	94.8	-57.5	
ES32	205.0	67.2	
ES33	102.2	-63.5	
ES34	98.1	-60.3	
ES35	102.6	-62.5	
ES36	106.3	-55.0	
ES37	104.4	-68.7	



MeanD	MeanT	k	alpha	R	RC	MDS	Dist
109	-57.0	3.2	39.8	5.1526151	180	ES32	142.7
101.3	61.3	237.1	4.4	5.9789085	16.5	ES37	7.5
100.8	-59.8	370.0	4	4.9891882	14	ES36	5.7
99.2	-61.0	633.4	3.7	3.9952633	11.9	ES31	4.1
100.9	-62.1	1610.4	3.1	2.9987581	9.3	ES34	2.3
102.4	-63.0	12710.0	2.2	1.9999213	6.7	ES33	0.5
						ES35	

**Appendix 2:** AMS Data for Study Sites.

Points on southern hemisphere plots indicate the declination and inclination of poles to the plane of foliation (magnetic axes).

Plot Legend:

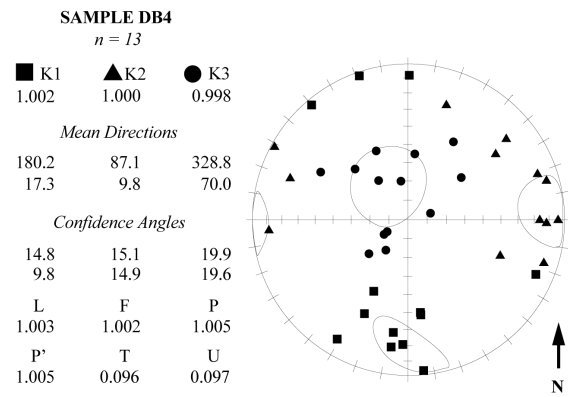
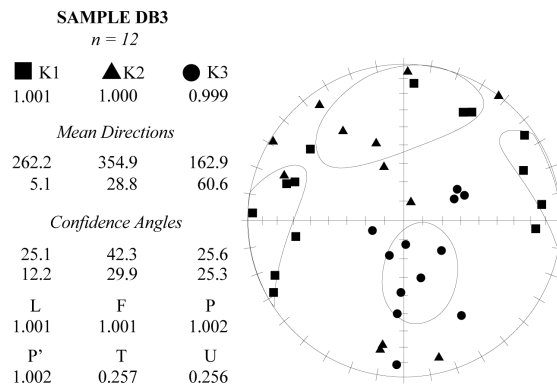
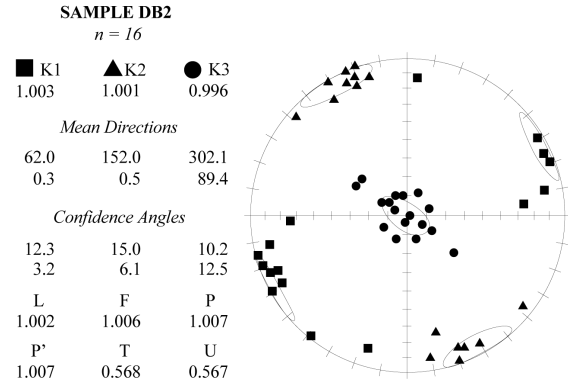
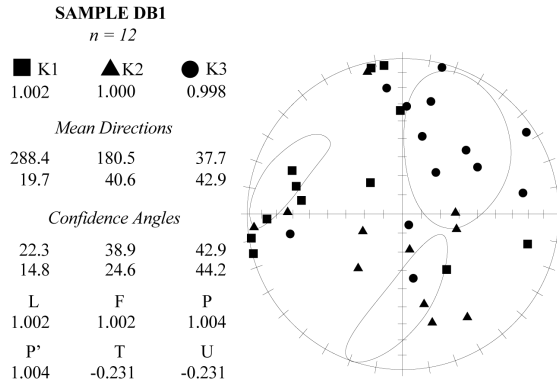
■  $K_1$  axis

▲  $K_2$  axis

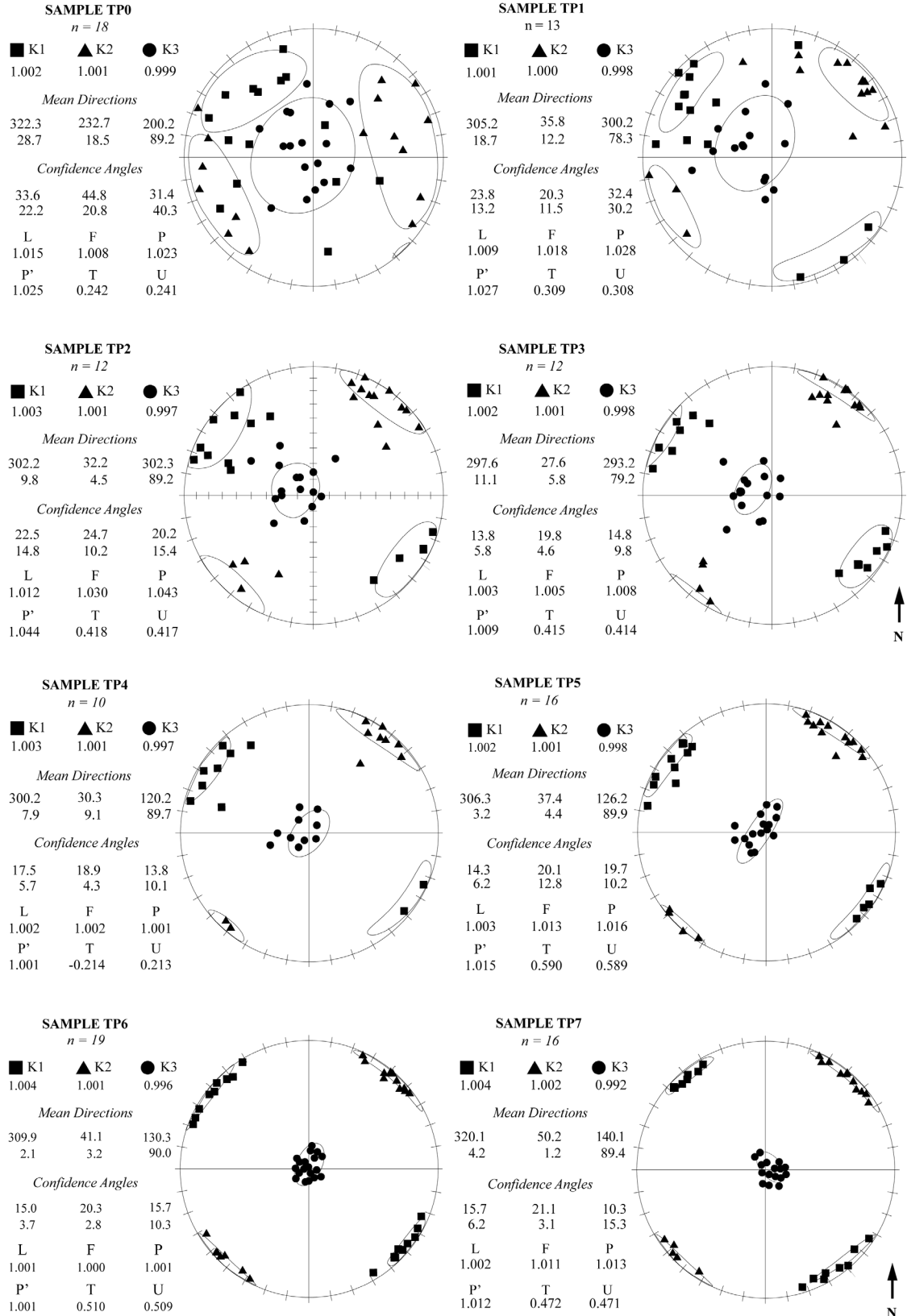
●  $K_3$  axis

◡  $\alpha 95$  confidence interval for contained set of axis measurements

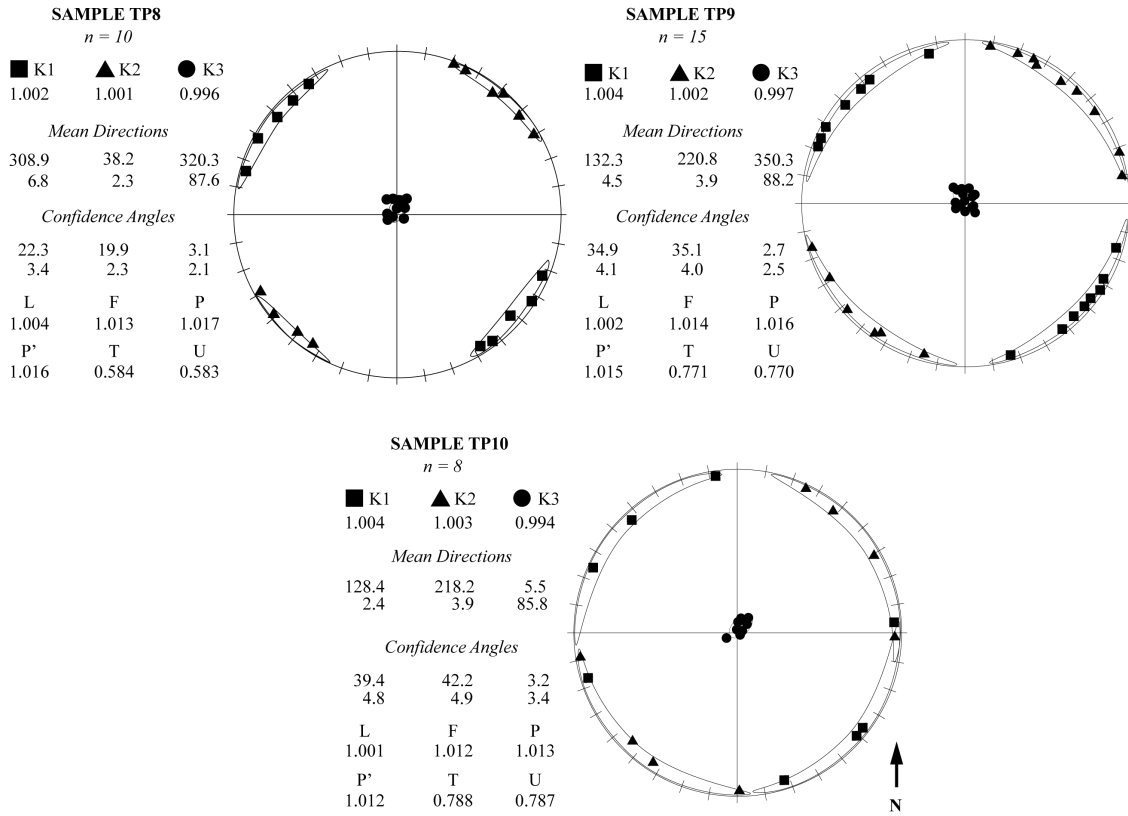
## Appendix 2.1: Deshghish AMS Data



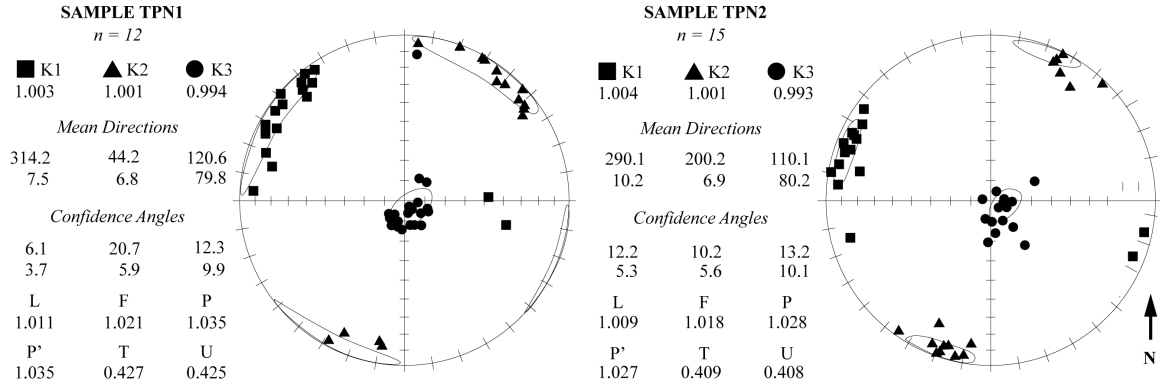
## Appendix 2.2 Triplets AMS Data



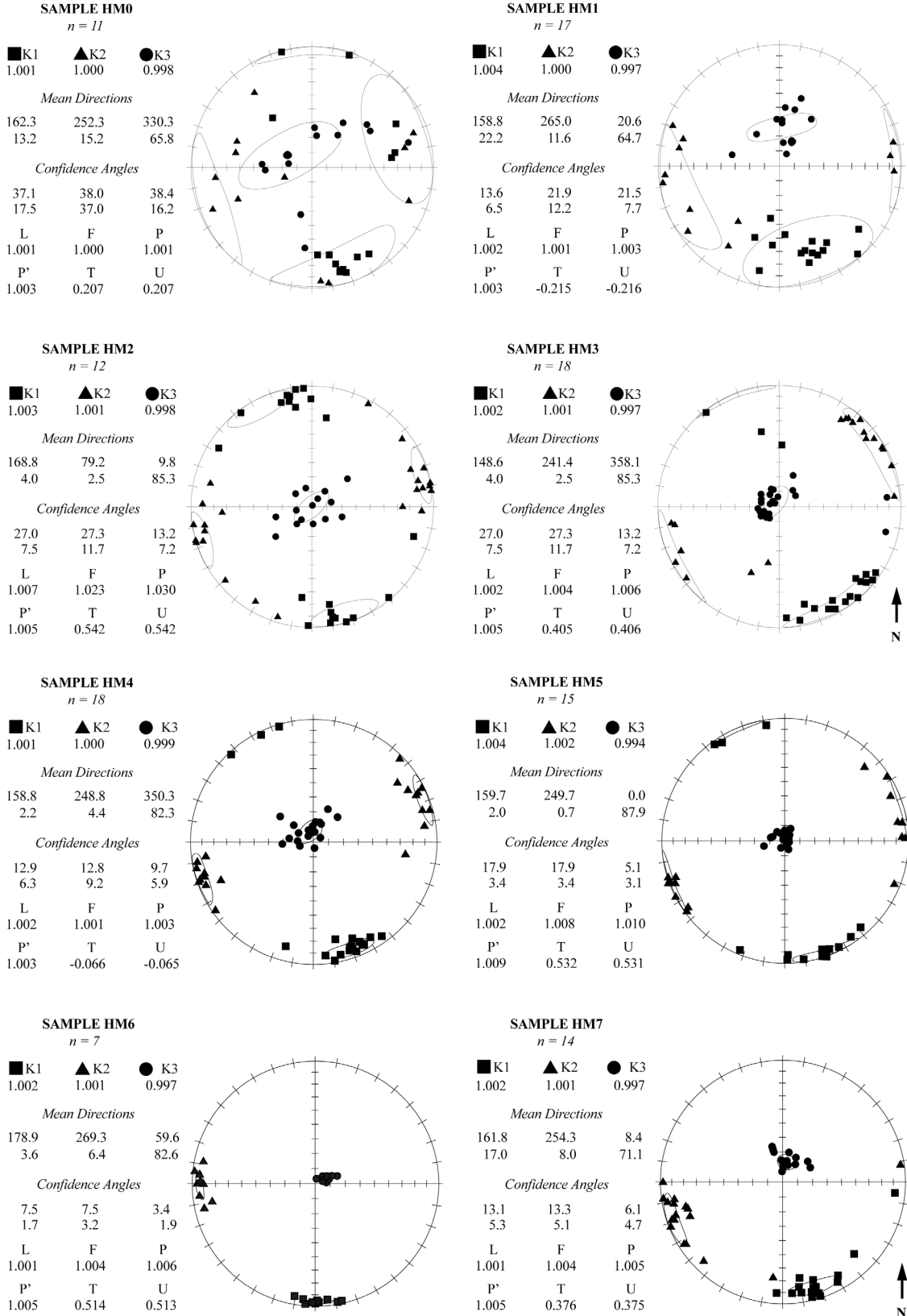
## Appendix 2.2 Triplets AMS Data (continued)



## Appendix 2.3 Triplets North AMS Data



## Appendix 2.4 Haskie Maar AMS Data



## Appendix 2.4 Haskie Maar AMS Data (continued)

**SAMPLE HM8**  
n = 15

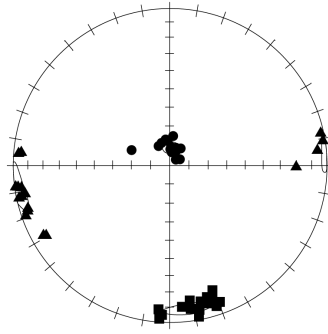
■ K1	▲ K2	● K3
1.004	1.002	0.994

*Mean Directions*

171.9	262.2	2.9
9.1	1.7	80.7

*Confidence Angles*

10.4	10.5	4.9
3.6	4.0	3.2
L	F	P
1.003	1.008	1.011
P'	T	U
1.011	0.507	0.508



**SAMPLE HM9**  
n = 18

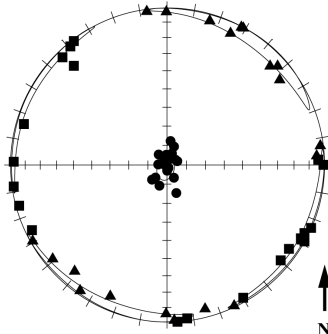
■ K1	▲ K2	● K3
1.004	1.003	0.993

*Mean Directions*

118.7	28.7	250.3
0.5	0.6	89.2

*Confidence Angles*

39.5	39.5	8.1
4.5	7.1	4.3
L	F	P
1.001	1.011	1.012
P'	T	U
1.011	0.716	0.714





## Appendix 2.5 Haskie Maar East AMS Data

